

METAL OXIDE MATERIALS FOR SOLID-STATE FLUORIDE ION BATTERIES

MSC. THESIS



METAL OXIDE MATERIALS FOR SOLID-STATE FLUORIDE ION BATTERIES

MSC. THESIS

by

Linhan PENG

to obtain the degree of Master of Science

at the Delft University of Technology,

to be defended publicly on 26th February 2024 at 11:00

Student Number: 5577136

Thesis committee:

Dr. Pedro B. Groszewicz,

Dr. S.T. (Shoshan) Abrahami

Dr. Amarante J. Böttger

Faculty:

Faculty of Mechanical Engineering (ME)

TU Delft, Daily Supervisor

TU Delft, Faculty Supervisor

TU Delft, Committee member

Keywords: Solid-state fluoride ion batteries, metal oxide materials, solid electrolyte

Front cover: First battery by Alessandro Volta. [1]

Copyright © 2024 by Linhan Peng

An electronic version of this dissertation is available at
<http://repository.tudelft.nl/>.

I think dialogue is very important for thinking.

John B. Goodenough

CONTENTS

Summary	ix
1 Introduction	1
2 State of Art	3
2.1 Fluoride ion batteries	3
2.1.1 From lithium-ion batteries to fluoride-ion batteries	3
2.1.2 Working principle of fluoride-ion batteries.	5
2.2 Materials of electrodes used in fluoride-ion batteries	7
2.2.1 Early work	7
2.2.2 Conversion-type electrodes	9
2.2.3 Intercalation-type electrodes	17
2.2.4 Metal oxyfluoride and metal oxide electrode materials.	21
2.3 Solid electrolytes used in fluoride-ion batteries	28
2.4 Objective	33
3 Material Preparation and Testing	35
3.1 Substances and equipment	35
3.2 Experimental synthesis	36
3.2.1 Ball Milling.	36
3.2.2 Synthesis of precursors	37
3.2.3 Electrode composites	38
3.3 Battery assembly	38
3.3.1 EIS Device	39
3.3.2 LSV device	40
3.3.3 Full cell device	40
3.4 X-Ray Diffraction (XRD).	42
3.4.1 X-Rays source and Blagg's law	42
3.4.2 Refinement	43
3.4.3 Experimental parameters	44
3.5 Electrochemical impedance spectroscopy (EIS).	45
3.5.1 Experimental parameters	47
3.6 Linear sweep voltammetry (LSV)	47
3.6.1 Experimental parameters	47
3.7 Cyclic voltammetry(CV)	48
3.7.1 Experimental parameters	49
3.8 Galvanostatic charge and discharge (GCD)	49
3.8.1 Experimental parameters	52

4	Results and Discussions	53
4.1	Solid Electrolyte Synthesis - $CsPb_{0.9}K_{0.1}F_{2.9}$ (PK10)	53
4.2	Ag full cell testing.	57
4.3	Room temperature testing of Cu_2O , FeO , Mn_2O_3 full cells	62
4.3.1	Room temperature testing of Cu_2O full cell	62
4.3.2	Room temperature testing of FeO full cell	66
4.3.3	Room temperature testing of Mn_2O_3 full cell	68
4.4	Symmetric cell testing.	72
4.4.1	Electrochemical performance	73
4.4.2	XRD characterization	80
4.5	Cu_2O full cell testing at 60 °C	85
4.5.1	Electrochemical performance	86
4.5.2	XRD characterization	88
5	Conclusions and outlook	93
6	Appendix	95
	Acknowledgements	103

SUMMARY

This study explores the potential of metal oxide fluorides as cathode materials for solid-state fluoride-ion batteries (FIBs), aiming to combine the stability of intercalation-based electrode materials with the high energy density of conversion-based materials. Through comprehensive experimental investigations using techniques such as electrochemical impedance spectroscopy (EIS), cyclic voltammetry (CV), galvanostatic charge-discharge (GCD), linear sweep voltammetry (LSV), and X-ray diffraction (XRD), the compatibility and electrochemical performance of transition metal oxides (Cu_2O , FeO , and Mn_2O_3) with $\text{CsPb}_{0.9}\text{K}_{0.1}\text{F}_{2.9}$ (PK10) solid electrolyte and Pb/PbF_2 composite anode are evaluated. Results indicate negligible room temperature capacity for Cu_2O , FeO , and Mn_2O_3 , suggesting potential limitations related to the cathode fluorination reaction. Additionally, PK10 electrolyte displays slight instability at room temperature, indicating potential electrochemical activity. Symmetric cell testing using Pb/PbF_2 composite electrodes confirms the suitability of the Pb/PbF_2 composite as both counter and reference electrodes. Notably, Cu_2O full cells show enhanced specific capacity at elevated temperatures (60°C), reaching 310.24 mAh/g during the first cycle, equivalent to 82.96% of the theoretical specific capacity. This considerable increase in capacity due to only a slightly higher temperature is attributed to reduced overpotential and enhanced fluoride ions diffusion rates. However, observation of capacity fade between cycles for the Cu_2O cell at 60°C suggests irreversible reactions, necessitating further investigation. In conclusion, this study highlights the potential of metal oxide cathode materials in solid-state FIBs, emphasizing the importance of understanding electrolyte stability and cathode compatibility for battery performance enhancement.

1

INTRODUCTION

With the rapid development of electrochemical energy storage technologies, the energy density of lithium-ion batteries is gradually approaching its theoretical "ceiling". Additionally, due to the limited lithium resources on Earth, scientists have been actively exploring new and improved battery technologies, with sodium-ion batteries, magnesium-ion batteries, and others emerging as research hotspots in the energy field. In comparison, fluoride ion batteries, which also belong to the "next generation" of electrochemical energy storage technologies, seem somewhat less prominent.

The concept of fluoride ion batteries was first proposed in the 1970s. Due to the low atomic weight of fluorine, rechargeable fluoride ion batteries offer high energy density. However, current fluoride ion batteries primarily rely on molten salt electrolytes for conducting fluoride ions at high temperatures (150°C). This limitation significantly impedes the commercialization and widespread adoption of this technology. Overcoming the challenge of achieving efficient fluoride ion conduction at room temperature has become the primary focus of fluoride ion battery development. Furthermore, in contrast to liquid electrolytes, solid electrolytes offer improved safety and substantial advantages in achieving a broad electrochemical stability window. Its potential has attracted considerable attention.

Regarding the electrode materials used in fluoride-ion batteries, they are typically classified into two types: conversion-type electrode materials and intercalation-type electrode materials. Each type has its own advantages and disadvantages. Conversion-type electrode materials offer higher capacity owing to the lower molecular mass of materials, whereas intercalation-type electrode materials exhibit better cyclability and rate capability due to lower volume changes during electrochemical reactions. However, there is a third type of material that is garnering attention: metal oxyfluoride. Metal oxyfluoride has the potential to combine the characteristics of conversion-type and intercalation-type electrode materials. Currently, only a few metal oxyfluoride materials have been explored.

In this project, metal oxyfluoride materials are not directly utilized as the cathode material. Instead, metal oxide materials are used as a preliminary step towards study-

ing metal oxyfluoride electrodes. The solid electrolyte $\text{CsPb}_{0.9}\text{K}_{0.1}\text{F}_{2.9}$, abbreviated as PK10, and Pb/PbF_2 are selected to complement three transition metal oxide materials: Cu_2O , FeO , and Mn_2O_3 . The electrochemical performance and underlying mechanisms of these solid-state fluoride ion battery systems will be investigated.

2

STATE OF ART

The development of energy storage systems is crucial to meeting our sustainability goals. Renewable energy sources, such as solar, wind, and tidal power, require efficient storage methods because they are intermittent. There are many ways to store energy in various forms, such as chemical, electrical, mechanical, magnetic, potential, and kinetic. Electrochemical energy storage and conversion is a particularly promising approach due to its high efficiency, versatility in form and volume, as well as the ability to perform well in various applications. Rechargeable batteries, or secondary batteries, are an especially appealing form of electrochemical energy storage. They can be designed as large, high-energy stacks for grid storage, or as micro-batteries for use in portable electronic devices. Moreover, they have the potential to replace combustion engines in vehicles and are already being used as complementary energy sources in hybrid electric vehicles. While fuel cells may seem like attractive alternatives for electric propulsion, they face criticism for their efficiency, price, and sustainability. Due to these aspects, more and more people focus on rechargeable battery research. Due to fluoride-ion batteries (FIBs) having attractive strengths including high energy density, stability, abundance, safety, and so on, more and more people have started to pay attention to their research. [2]

2.1. FLUORIDE ION BATTERIES

2.1.1. FROM LITHIUM-ION BATTERIES TO FLUORIDE-ION BATTERIES

Lithium-ion batteries (LIBs) have been the dominant rechargeable battery technology in recent years due to their high energy density, long cycle life, and low self-discharge rate. However, their reliance on expensive and limited lithium resources has led to the search for alternative battery chemistries. [3]

Also, the safety issues related to lithium-ion batteries are always a problem. Lithium-ion batteries have several safety issues that have been documented. One of the most common problems is the potential for thermal runaway, which can cause the battery to overheat, ignite, and possibly explode. This can occur due to a variety of factors, including overcharging, physical damage to the battery, exposure to high temperatures, or

manufacturing defects. Another issue with lithium-ion batteries is the potential for short circuits. This can happen if the positive and negative electrodes come into contact with each other, either due to physical damage or an internal defect. Short circuits can cause the battery to overheat, and may also lead to thermal runaway. There have also been cases of lithium-ion batteries catching fire during transportation, storage, or use. This can occur if the battery is damaged or subjected to extreme conditions, such as exposure to high temperatures or pressure. [4]

Also, the energy density of lithium-ion batteries is not sufficient for use in electric aircraft as the aviation industry is facing increasing pressure to reduce its environmental impact since the world confronts a climate crisis caused by greenhouse gas emissions. The theoretical maximum energy density of commercial lithium-ion batteries has been nearly reached, which is usually less than 350 Wh kg^{-1} [5]. One potential solution is the transition to electric aircraft, which could significantly reduce emissions. However, for electric aviation to become a viable alternative to fossil fuel-powered aviation, batteries with significantly higher energy densities are required. To achieve the necessary range and payload capacity, a battery with an energy density of around 800 Wh kg^{-1} would be required. This is almost three times the energy density of current lithium-ion batteries. [3]

Li ions can be considered as mobile and stable energy carriers in LIBs and they can be extended to appropriate cations and anions for other battery technologies. Although many cation-based shuttle batteries have been developed, such as magnesium-ion batteries, sodium-ion batteries, potassium-ion batteries, and aluminum-ion batteries, etc, there are fewer anion-based shuttle batteries. The most widely researched anion-based shuttle batteries are hydroxide-ion batteries, chloride-ion batteries, and fluoride-ion batteries (FIBs) as the corresponding ions are more mobile and stable [6]. However, compared with cation-based batteries, anion-based batteries have lower charge densities which have less possibility to introduce challenges for ion transport and reversible cycling. And within these anion-based batteries, fluoride-ion batteries (FIBs) are potential as it has the smallest radius and fluorine is the lightest element in its group, which is responsible for faster ionic transport and higher energy densities. FIBs have significantly large energy density which can reach 5000 Wh L^{-1} and 2200 Wh kg^{-1} theoretically resulting from multiple-electron redox reaction [7, 5]. The energy density of FIBs is incredible which is 8 times higher than the LIBs [6]. The comparison of gravimetric energy density and volumetric energy density between FIBs and other secondary ion batteries can be found in Fig.2.1.

Furthermore, fluorine is the most electronegative element and the strongest oxidizing agent in the periodic table, allowing for a wide electrochemical window (from 3.03 V vs NHE to $+2.87 \text{ V}$ vs NHE) [8, 6]. This excellent oxidative stability of fluoride ions enables the utilization of redox pairs with higher voltages [3]. In terms of economics and elemental abundance, Fluorine is the 13th most abundant element in the earth's crust and exists primarily as fluorspar (CaF_2) [3]. The comparison of global production of fluorine and lithium can be found in Fig.2.2.

In terms of safety, FIBs are safer than LIBs in the following respects. Since FIBs can use non-flammable electrolytes, which reduces the risk of thermal runaway and fire compared to some LIBs that use flammable electrolytes. Also, FIBs are less prone to

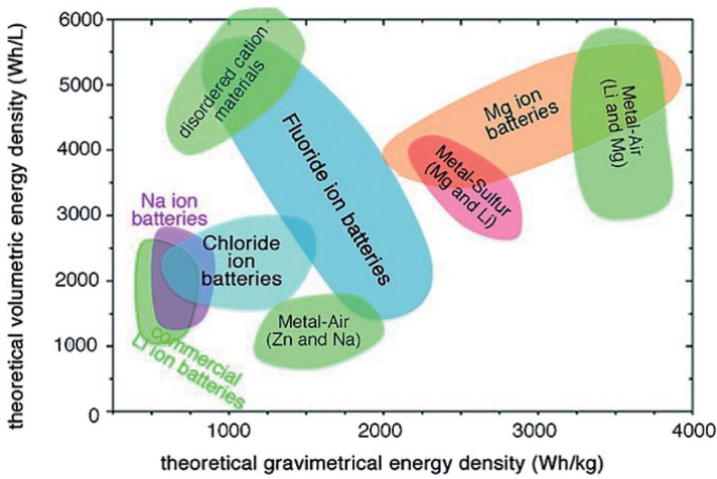


Figure 2.1: Overview of secondary ion batteries for future battery technologies. [8]

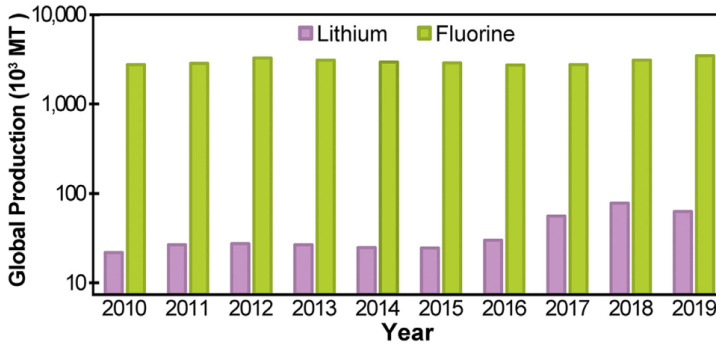


Figure 2.2: Global production of fluorine and lithium. [3]

the formation of dendrites, tiny needle-like structures that can grow inside a battery and cause short circuits compared to some types of LIBs, and thus, dendrites will not puncture the separator and cause a short circuit [5]. Recently, solid-state fluorine-ion batteries (SSFIBs) have received widespread attention due to fluoride-ion conductors while using solid electrolytes have excellent chemical stability, which reduces the risk of electrolyte decomposition and other chemical reactions that can lead to safety hazards. Also, solid-state FIBs typically operate at high temperatures, which can improve battery performance and safety by reducing the risk of thermal runaway.

2.1.1.2. WORKING PRINCIPLE OF FLUORIDE-ION BATTERIES

The FIBs studied in this thesis are classified as all-solid-state batteries which means FIB electrodes with a solid electrolyte. The most common and basic cathode in FIBs is the metal fluoride MF_x and the anode can be a metal M' . The battery is usually operated at

high temperatures around 150-200 °C while using solid electrolytes, however, there are always exceptions that can operate at room temperature, such as using BaSnF₄. Upon discharge, the metal fluoride cathode MF_x (positive charge) undergoes reduction while the metal anode M' (negative charge) undergoes oxidation. The charge process is vice versa. Reactions are presented below.

2

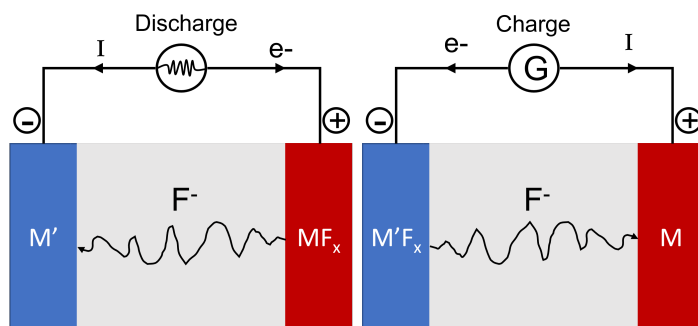
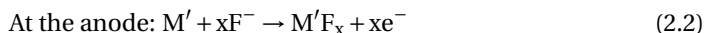
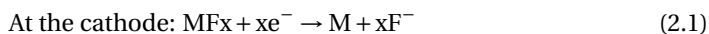
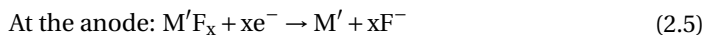
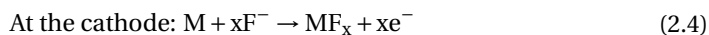


Figure 2.3: Illustration of a fluoride-ion battery at discharge (left) and charge (right) state.

Discharge:



Charge:



The variable x in the equations represents the number of fluoride ions that are exchanged per mole of the metal ion. This value is closely related to the oxidation state of the metal, as it reflects the number of electrons that are gained or lost by the metal during the reaction. Therefore, the value of x provides important information about the chemical properties and reactivity of the metal.

Take BiF₃|electrolyte|Zn as an example. In the very beginning state, BiF₃ and Zn exist to be the electrodes.

Table 2.1: Electrochemical series.

Reaction	E° /V
$\text{Bi}^{3+} + 3 \text{e}^- \rightleftharpoons \text{Bi}$	0.308
$\text{Zn}^{2+} + 2 \text{e}^- \rightleftharpoons \text{Zn}$	-0.7618

According to the Eq.2.7 and the Table.2.1,

$$E^{\circ} = E_{red}^{\circ}(\text{reduction process}) - E_{red}^{\circ}(\text{oxidation process}) \quad (2.7)$$

$E^{\circ} = 0.308 - (-0.7618) = 1.0698$ V. At the standard state, according to the Nernst equation

$$\Delta G^{\circ} = -nFE^{\circ} \quad (2.8)$$

As the value of E° is positive, the ΔG° is negative. So the reaction happens spontaneously which means it is discharging progress. Upon discharging, BiF_3 is reduced to Bi while Zn is oxidized as ZnF_2 . After complete discharging, the cell starts to charge with the beginning state of Bi|electrolyte| ZnF_2 . For charging progress, $E^{\circ} = -0.7618 - 0.308 = -1.0698$ V, so ΔG° is positive which means the process is unspontaneous and this is consistent with the charging progress.

In many cases, conditions deviate from the standard state, leading to changes in Gibbs energy. However, even in these non-standard conditions, the Gibbs energy remains connected to the standard condition, as illustrated by the equation below:

$$\Delta G = \Delta G^{\circ} + RT \ln Q \quad (2.9)$$

Under non-standard conditions:

$$\Delta G = -nFE \quad (2.10)$$

After combining Eq.2.9 and Eq.2.10, the Eq.2.11 is derived:

$$E = E^{\circ} - \frac{RT}{nF} \ln Q \quad (2.11)$$

The assessment of whether a reaction can occur spontaneously remains the same under both standard and non-standard conditions.

2.2. MATERIALS OF ELECTRODES USED IN FLUORIDE-ION BATTERIES

2.2.1. EARLY WORK

In 1974, the concept of fluoride ion batteries (FIBs) was introduced and they were initially known as fluoride galvanic cells. Baukal et al. [9] proposed that calcium fluoride (CaF_2) could function as a solid electrolyte in an all-solid-state FIB, even at high temperatures ranging from 400-500 °C. Despite this proposal, there are no records of any experiments conducted on the operation of a complete FIB cell. Therefore, while the idea of using CaF_2 as a solid electrolyte in FIBs is intriguing, further research is required to determine its feasibility.

In 1976, Kennedy and Miles [10] conducted an experiment demonstrating an electrochemical cell that utilized fluoride ions shuttling. They used KF-doped $\beta\text{-PbF}_2$ as a solid electrolyte in $\text{CuF}_2|\beta\text{-PbF}_2|\text{Pb}$ and $\text{AgF}|\beta\text{-PbF}_2|\text{Pb}$ electrochemical cells. Although the starting potentials were close to the open cell voltage, poor capacities were observed,

which were attributed to the formation of the α -PbO₂ phase in the anode material, leading to poor ionic conductivity. Kennedy and Miles also discharged a thin-film cell composed of CuF₂, Pb, and PbF₂ as cathode, anode, and electrolyte materials, respectively, and found that discharge capacities of up to 40% of the theoretical capacity (528 mAh g⁻¹) of CuF₂ could be obtained [11]. However, further charging of the cell could not be achieved. These results suggest that while fluoride ion shuttling has the potential for use in electrochemical cells, there are still challenges to be addressed in improving their capacity and performance.

Schoonman [12] experimented in the same year where he built a Pb| β -PbF₂:AgF|BiO_{0.09}F_{2.82}|Bi cell by spring-loading disks of Pb and Bi painted with powders of β -PbF₂, AgF or BiO_{0.09}F_{2.82}, respectively, from dispersions in ethyl acetate. The discharge potential observed was close to the open cell voltage, indicating that oxyfluorides could be potential electrolyte materials for FIBs. However, there was no further information provided regarding the reversibility of the cell, and therefore, it is unclear whether this approach is a viable option for the development of FIBs. Further research is needed to determine the efficacy and feasibility of using oxyfluorides as electrolyte materials in FIBs.

Meantime, Borger et al. [13] filed a patent proposing the use of carbon fluoride (CF)_x as an active material in FIBs. The patent described the use of K_{0.25}Pb_{0.75}F_{1.75} as a solid electrolyte to discharge (CF)_x against a lead electrode at 280 °C with a current of 0.1 mA. This is the only experimental result reported in the patent, but it is significant as it suggests the potential for carbon to be utilized as an active material in FIBs.

In 1978, Danto and colleagues [14] reported on the reversible cycling of thin-film solid-state galvanic cells with a mean thickness of 0.55 μ m. These cells were composed of Pb as the anode, Bi/BiF₃ as the cathode, and cubic β -PbF₂ as the electrolyte. The experiments were conducted at room temperature, and the results showed a starting discharge potential as high as 353 mV, followed by a discharge plateau at around 280 mV for a current density of 40 μ A cm⁻². This work demonstrated the potential for using thin-film solid-state galvanic cells in FIBs, although further research is needed to optimize their performance and explore their potential applications.

In 1979, Schoonman [15] conducted further investigations on the electrolytes for fluoride-ion galvanic cells and reported on a solid solution-based electrolyte M_{1-x-y}U_xCe_yF_{2+2x+y} (M = Ca, Sr, Ba) with BiF₃ as cathode and Ca as anode materials.

In 1981, Schoonman and Wolfert [16, 17] used the term "solid-state fluoride-ion battery" for the first time in their publications, where they reported on the improved ionic conductivity of CaF₂ anodes by doping with La or Yb. This was achieved by forming the corresponding fluoride Ca_{1-x}La_xF_{2+x}. This work highlights the importance of doping in improving the performance of electrolyte materials in FIBs, and the continued efforts to optimize the materials used in FIBs for better performance.

However, between 1981 and 2011, research about FIBs stagnated. Until 2011, Reddy and Fichtner [18] researched reversible all-solid-state conversion-based FIBs using metal/metal fluoride electrode materials and Ba-doped LaF₃ (La_{0.9}Ba_{0.1}F_{2.9}) as a solid-state electrolyte. These systems were operated at elevated temperatures of around 150-200 °C, and they also observed relatively short-life cycling performances. This research shows that La_{0.9}Ba_{0.1}F_{2.9} has the highest ionic conductivity among all other La_{1-x}Ba_xF_{3-x}

($0 \leq x \leq 0.15$) compounds (about $2.8 \times 10^{-4} \text{ S cm}^{-1}$ at 160°C) and good electrochemical stability resulted from the low electrochemical potentials of Ba^{2+} and La^{3+} . Several metal fluorides, such as CuF_2 , BiF_3 , SnF_2 , and KBiF_4 were investigated as cathode materials against Ce metal in their research. From then on, there is a renewed focus on FIBs research including solid and liquid electrolytes, conversion and intercalation type electrodes as well as the battery system design improvement.

2.2.2. CONVERSION-TYPE ELECTRODES

Because the electrode active materials in FIBs are mainly composed of metal and F ions, FIBs typically utilize lightweight electrode materials. There are basically two types of electrodes in FIBs. One is the conversion type and the other is based on the intercalation mechanism (also known as the insertion mechanism or solid solution reactions). In this thesis, research will focus on a new potential type which is oxyfluorides and it will be discussed in section 3.4.

For the first type, conversion-based electrodes generally have high capacities as they are capable of accommodating more electrons per redox-active materials (AM) and they have a lower mass of active materials than intercalation-based electrodes. However, there's always a change in the crystal structure while the conversion electrode undergoes a redox reaction. This results in the breaking and combining of the chemical bonds as well as a large volume change. The large volume change in the electrodes during charging and discharging should be attenuated since it leads to internal stresses which cause pulverization and also results in less physical contact between active materials. Furthermore, it leads to the degradation of the electrode/electrolyte interphase. These all deteriorate the electrochemical performance of the electrodes such as cyclability. Also, close-packed metal atoms (eg. Cu, Co, Ni, Bi) cannot provide fluoride-ions with diffusion paths in conversion-type M/MF_x systems. [3, 8, 6, 19]

The fluoride conversion reaction is related to the diffusion rates of F^- through the fluoride layer which has a connection with the crystal structure. Faster diffusion of F^- is beneficial to the conversion reaction. The alkaline earth fluorides like CaF_2 , BaF_2 , and SrF_2 have a common cubic fluorite structure (Fm $\bar{3}$ m), while rare earth fluorides such as LaF_3 , CeF_3 , and NdF_3 have a trigonal tysonite structure (P $\bar{3}$ c1). These two types of crystal structures can be superionic conductors at high temperatures, and they are usually studied within the aspect of electrolytes. Also, due to the low work function of metals, they are usually used as anode materials. These materials can be doped with other elements becoming mixed cation species to increase the ionic conductivities. For example, introduce Ba^{2+} to LaF_3 to get $\text{La}_{1-x}\text{Ba}_x\text{F}_{3-x}$ which contains additional fluoride anion vacancies; introduce La^{3+} to BaF_2 to get $\text{Ba}_{1-x}\text{La}_x\text{F}_{2+x}$ which contains additional fluoride anions at the interstitial sites. However, this doping method is less used in cathode materials as most crystal structures of cathode materials show unconscious fluoride ion conduction than these anion crystal structures. The later 3d transition-metal fluorides can generally be considered as rutile (P4 $_2$ /mm) (PbF_2 , MgF_2 , NiF_2), orthorhombic (R $\bar{3}$ c) (FeF_3 , CoF_3 , AlF_3 , YF_3 and BiF_3) and the tetragonal I $_4$ /mmm (SnF_4 , NbF_4) crystal structure. The rutile difluorides have the lowest F^- conductivities and the later two structures' nature of F^- conduction is less known. In addition, CuF_2 is a rutile-like crystal structure. The "Ball and stick" models for the most common crystal structures of binary metal flu-

oxides are shown in Fig.2.4. [3]

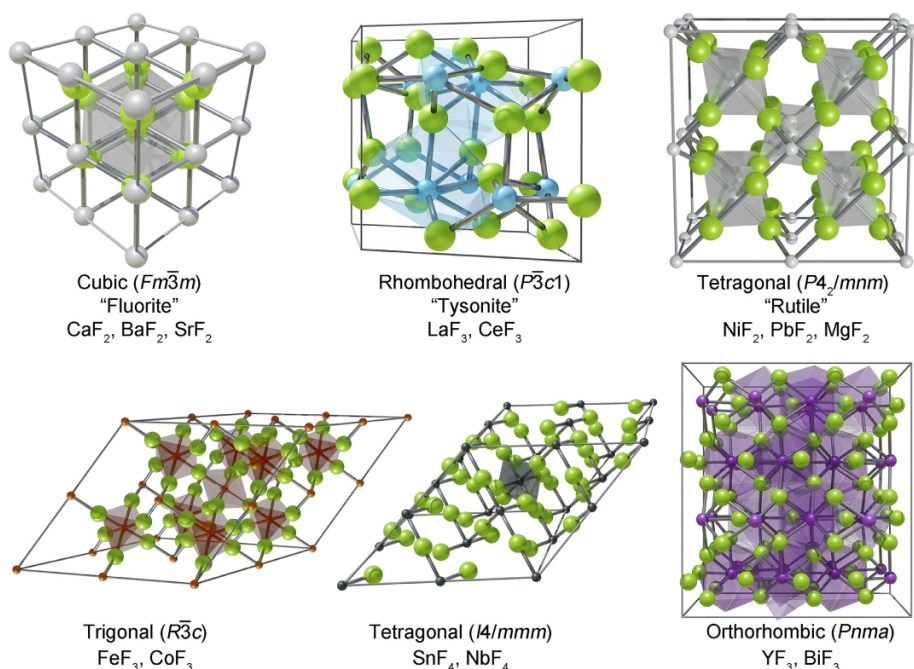


Figure 2.4: "Ball and stick" models for the most common crystal structures of binary metal fluorides. [3]

Conversion-based cathode materials

The most used cathode materials by far are BiF_3 and CuF_2 in conversion-based FIBs [8]. Theoretical capacities of Cu/CuF_2 and Bi/BiF_3 are calculated to be 843 and 384 mAh g^{-1} , respectively [8]. With its advantageous properties of low cost, high redox potential, and low molecular weight, CuF_2 is a highly desirable cathode material that has impressive theoretical properties, including a high gravimetric capacity and a high theoretical conversion potential of 3.55 V [6].

In a study published in 2011, M. Anji Reddy and M. Fichtner [18] investigated the use of CuF_2 cathodes in FIBs. Their experiments utilized a CuF_2 cathode, $\text{La}_{0.9}\text{Ba}_{0.1}\text{F}_{2.9}$ electrolyte, and a Ce anode, and demonstrated a high first cycle discharge capacity of 322 mAh g^{-1} . However, the study was limited in that it only demonstrated the discharge of CuF_2 for one cycle, without results of the reversibility of the reaction. Additionally, while the high first-cycle discharge capacity is promising, further investigation is needed to evaluate the long-term performance of CuF_2 cathodes in FIBs.

In 2017, Thieu [20] demonstrated the reversibility of CuF_2 as a cathode material in the fluoride ion battery system with tysonite-type $\text{La}_{0.9}\text{Ba}_{0.1}\text{F}_{2.9}$ as an electrolyte and a metallic La as an anode. Fig.2.5 shows that the electrode could achieve an initial discharge capacity of 360 mAh g^{-1} , which is equivalent to approximately 68% of its theoretical specific capacity of 527 mAh g^{-1} . Two plateau regions indicate a two-step reaction

during charging. Analysis of the discharge pattern of CuF_2 cathodes has revealed that the pseudo-plateau at the lower voltage range corresponds to the oxidation of $\text{Cu}(0)$ metal to $\text{Cu}(I)$, while the pseudo-plateau at the higher voltage range may be related to the further oxidation of $\text{Cu}(0)$ or $\text{Cu}(I)$ to $\text{Cu}(II)$ species. Interestingly, the first discharge pattern differs from the subsequent discharges, which showed two pseudo-plateaus. The first pseudo-plateau region at higher voltage can be related to the reduction of $\text{Cu}(II)$ to $\text{Cu}(I)$, and the second one is related to the conversion of $\text{Cu}(II)$ and/or $\text{Cu}(I)$ to $\text{Cu}(0)$ metal. However, the capacity of CuF_2 cathodes fades drastically on subsequent cycling, indicating poor cycling stability. To overcome the limitations of poor electrochemical reversibility and cyclability of CuF_2 cathodes, researchers have recommended the technique of surface covering of the electrode material. This involves modifying the electrolyte/electrode interface to prevent Cu metal diffusion and control the volumetric changes during cycling. In addition to surface covering, the type of grinding material and ball-to-powder ratio during the ball mill are critical factors in achieving high mobility of F ions within the composite cathode material.

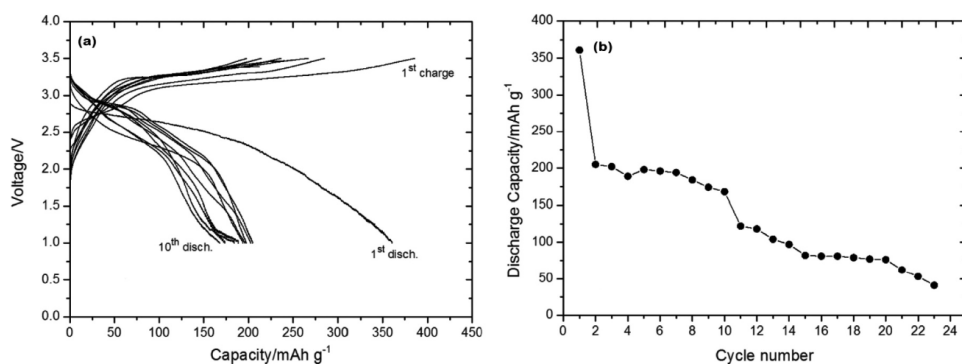


Figure 2.5: (a) Charge-discharge curve (first 10 cycles) and (b) cycling behavior (first 24 cycles) of $\text{CuF}_2/\text{La}_{0.9}\text{Ba}_{0.1}\text{F}_{2.9}/\text{La}$ cell at $150\text{ }^\circ\text{C}$ (current density: 4 mA g^{-1}) [20]

In 2020, Nakano et al.[21] demonstrated the feasibility of FiBs as extremely high-energy batteries while using a 2.3 nm thick film of Cu as cathode and LaF_3 as the anode. They found that the discharge capacity of the cell at a temperature of $150\text{ }^\circ\text{C}$ was very close to its theoretical capacity, reaching $820\text{ mAh g}^{-1}\text{ Cu}$ out of a theoretical maximum of $844\text{ mAh g}^{-1}\text{ Cu}$. Even at a lower temperature of $80\text{ }^\circ\text{C}$, the cell still exhibited a relatively high discharge capacity of $671\text{ mAh g}^{-1}\text{ Cu}$, which is equivalent to 80% of its theoretical capacity. The cell was also able to operate at room temperature ($25\text{ }^\circ\text{C}$) with promising results. After 30 cycles, the capacity retention was recorded at 76%.

In 2021, research on all-solid-state FiBs has shown promising results by optimizing the chemistry and composition of CuF_2 electrodes. By using a copper-gold alloy known as Cu_3Au , the performance of the cathode was improved due to Cu_3Au 's ability to buffer volumetric differences and reduce lattice strain at the phase boundary [22]. This led to high rate performance and a longer cycle life compared to the use of pure Cu . Additionally, a highly reversible two-phase reaction between Cu_3Au and CuF_2 was observed.

Zhang et al. [23] reported that the formation of a composite material consisting of

copper and lead fluoride (Cu/PbF_2) further enhanced the electrode composition and contributed to better overall performance.

Recently, Tojigamori et al.[24] reported a composite cathode, Pb_2CuF_6 which is synthesized by doping of CuF_2 with PbF_2 showed an higher ionic conductivity of $3.6 \times 10^{-8} \text{ S cm}^{-1}$ at RT and $3.0 \times 10^{-5} \text{ S cm}^{-1}$ at 140°C . The study showed that during the first discharge, Pb_2CuF_6 demonstrated a high capacity of 319 mAh cm^{-3} per electrode volume, which was higher than that of the conventional CuF_2 electrode. The material exhibited a plateau at $\sim 0.5 \text{ V}$, indicating the presence of a redox reaction. After the first discharge, Pb_2CuF_6 reacted at a potential of $\sim 0.7 \text{ V}$ versus Pb/PbF_2 , indicating the redox potential of copper. It showed a reversible capacity of 46% of the theoretical capacity, with a discharge capacity of 24% of the theoretical capacity, even at a high rate of 1 mA cm^{-2} . The Cu utilization ratio was about four times higher than that of the CuF_2 cathode. The study confirmed the reversible formation of $\beta\text{-PbF}_2$ and Pb_2CuF_6 as fluoride-ion conductors during the discharge and charge processes, respectively.

BiF_3 is a cathode material that has a low energy density due to the massive atomic weight of bismuth. It has a relatively high redox potential and low volume changes during (de)fluoridation as seen in Fig.2.6. The low cost of bismuth makes BiF_3 an attractive option as a cathode material, potentially more cost-effective than other materials like NiF_2 or SnF_4 . Although the reversible (de)fluoridation of BiF_3 has been demonstrated, it suffers from limited capacity retention. Given the large ionic radius of bismuth and its tendency to alloy with other metals, it may be more useful as a substitutional component for modifying the structure and fluoride-ion conductivity of ternary metal fluorides. Due to the relative scarcity of bismuth, this approach could be more sustainable and efficient in developing high-performance cathode materials. [3]

	Active material	Redox pot. (V versus Li^+/Li)	Specific capacity ^a (mAhg^{-1})	Fluoride crystal structure	Density (g cm^{-3})	Volume change $\text{M} \rightarrow \text{MF}_x$	Metal price ($\text{US\$ kg}^{-1}$)
Cathode	$\text{Cu} \leftrightarrow \text{CuF}_2$	3.54	843.5	rutile-like ($P2_1/c$)	8.96	237%	7–9
	$\text{Fe} \leftrightarrow \text{FeF}_3$	2.74	1,439.8	rhombohedral ($R\bar{3}c$)	7.87	311%	~ 1
	$\text{Ni} \leftrightarrow \text{NiF}_2$	2.96	913.32	rutile ($P4_2/mnm$)	8.91	211%	18–20
	$\text{Sn} \leftrightarrow \text{SnF}_4$	2.86	903.08	tetragonal ($I4/mnm$)	7.27	150%	22–24
	$\text{Bi} \leftrightarrow \text{BiF}_3$	3.18	384.7	orthorhombic ($Pnma$)	9.78	50%	5–6
Anode	$\text{CaF}_2 \leftrightarrow \text{Ca}$	0.00	686.5	fluorite ($Fm\bar{3}m$)	3.18	-6%	$\sim 0.4^b$
	$\text{MgF}_2 \leftrightarrow \text{Mg}$	0.54	860.3	rutile ($P4_2/mnm$)	3.15	42%	2–3
	$\text{YF}_3 \leftrightarrow \text{Y}$	0.41	551.1	orthorhombic ($Pnma$)	4.01	168%	3–5 ^c
	$\text{SrF}_2 \leftrightarrow \text{Sr}$	0.05	426.7	fluorite ($Fm\bar{3}m$)	4.24	-11%	5–5.5
	$\text{LaF}_3 \leftrightarrow \text{La}$	0.66	410.4	tysonite ($P\bar{3}c1$)	5.94	47%	1.5–3.5 ^c

Salient properties of the five most attractive and practically viable conversion-type fluoride-ion battery cathodes and anodes, listed in order of theoretical energy density.

^aTheoretical capacities calculated for the discharged state with a metal cathode and a metal fluoride anode.

^bPrice is shown for the metal fluoride.

^cPrice is shown for the metal oxide.

Figure 2.6: Several common fluoride conversion electrodes. [3]

In 2017, Grenier et al.[25] conducted a detailed study on the reaction between bismuth and bismuth fluoride ($\text{Bi} + \text{BiF}_3$), using synchrotron data analysis called pair distribution function analysis. They found that the reaction between Bi and BiF_3 is complex and involves the formation of oxyfluoride compounds during the intermediate stages of the reaction. The study also showed that these impurities cannot move through the electrolyte and are restricted to the side of the electrode where they were formed.

In 2019, Yamanaka [26] has extensively studied the structural transformation, reactivities, and mechanisms of BiF_3 microparticles of different structures (orthorhombic BiF_3 (o- BiF_3) and cubic BiF_3 (c- BiF_3)). For o- BiF_3 , the direct defluorination process happened at a voltage range of 0.45-0.2 V and began with the contours of the particles losing fluoride ions. For c- BiF_3 , the defluorination process occurred at a voltage below 0.2 V and could happen through both a direct mechanism and a dissolution-deposition mechanism. The processes are illustrated in Fig.2.7 When the particles were exposed to stronger excitation power, the dissolution-deposition mechanism was more dominant due to a thermal effect. Overall, the study showed that the defluorination of c- BiF_3 was slower than that of o- BiF_3 and began with the appearance of the bismuth nucleus.

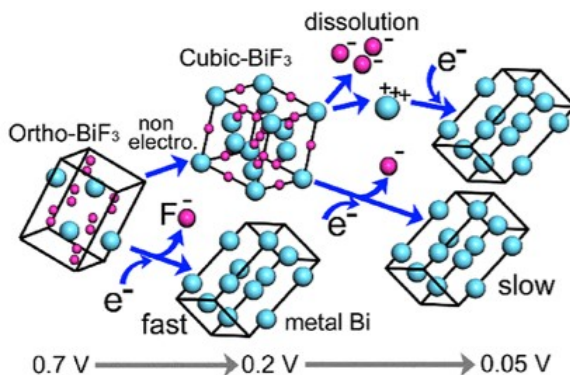


Figure 2.7: Reactivities and mechanisms in defluorination for orthorhombic BiF_3 and cubic BiF_3 while the voltage of BiF_3 /gold (cathode) vs a Pb counter electrode (anode) was decreased from OCV (0.7 V) to 0.05 V step by step.[26]

In 2020, Konishi [27] grounded BiF_3 into a powder and mixed it with a conductive material using a planetary ball mill. The results showed that increasing the rotation speed of the ball mill improved the adhesion between the conductive material and the BiF_3 particles. As a result, the BiF_3 electrode produced had a high practical capacity in the first cycle and maintained this capacity in subsequent cycles. Pristine BiF_3 and BiF_3/C electrodes are studied and show different performances as the discharge/charge capacities of the former and later electrodes in the first cycle were 212/95 and 427/239 mAh g^{-1} , respectively (Fig.2.8). However, BiF_3 is a type of conversion material that undergoes large volume changes during cycling, which causes it to partially separate from other components in a BiF_3/C composite. As a result, the composite electrode gradually loses capacity over successive cycles. Also, X-ray absorption fine structure analysis confirmed that the reversible electrochemical reaction of the BiF_3 electrode was progressing as intended during the cycling process.

After this research, the same group reported solid solutions of $\text{BiF}_3\text{-BaF}_2$, with varying ratios of the two compounds [28]. $\text{BiF}_3\text{-BaF}_2$ has an orthorhombic phase when $x=0$, a hexagonal phase when $x=0.2$, and a cubic phase when $x=0.4$. The performance also varies with the amount of Ba in the mixture. As seen in Fig.2.9, the initial reversible capacity of $\text{Bi}_{1-x}\text{Ba}_x\text{F}_{3-x}$ ($x=0.2$) was 211 mAh g^{-1} , which is higher than 175 mAh g^{-1} , the reversible capacity of $x=0$ in the first cycle. However, the reversible capacities of $x=0.2$

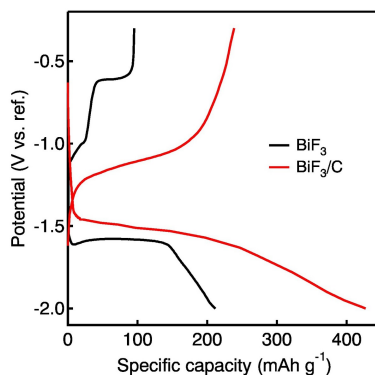


Figure 2.8: Charge and discharge profile of BiF_3 and BiF_3/C in the first cycle.[27]

decreased to 140 and 98 mAh g^{-1} in the second and third cycles, respectively. Although the reversible capacity of $x=0.2$ decreased gradually during cycling, it still showed better capacity retention compared to $x=0$. Changing the composition further to $x=0.4$ (cubic) led to even better capacity retention during cycling, although the initial reversible capacity decreased due to an excess of barium that did not participate in the redox reaction.

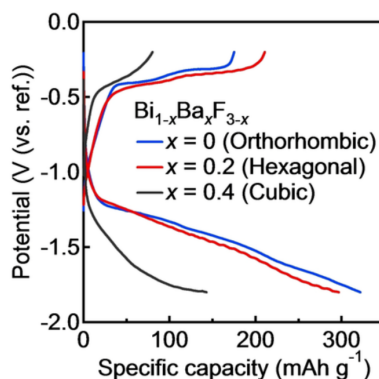


Figure 2.9: Charge and discharge curves of $\text{Bi}_{1-x}\text{Ba}_x\text{F}_{3-x}$ with $x=0, 0.2,$ and 0.4 over the potential range from -1.8 to -0.2 V (vs. Ag/Ag^+). [28]

For other conversion-based cathode electrode materials, NiF_2 , FeF_3 , and SnF_4 have lower cathode potentials than CuF_2 , but they have higher gravimetric capacities. Among them, FeF_3 is particularly interesting due to its low cost and high abundance in the Earth's crust. Inoishi et al.[29] investigated the reversibility of FeF_3 in conjunction with fluorite-type $\text{Ba}_{0.6}\text{La}_{0.4}\text{F}_{2.4}$ as the electrolyte and Pb as the counter-electrode material. This is the first time FeF_3 has been tested as the cathode in a fluoride battery for its performance. It initially had a discharge capacity of 579mAh g^{-1} and could retain 461mAh g^{-1} of its capacity after 10 cycles as seen in Fig.2.16. By using X-ray diffraction and X-ray absorption spectroscopy, the scientists were able to understand how FeF_3 reacts during

the charging and discharging process. The results showed that FeF_3 is converted to FeF_2 and then to Fe metal during discharge, and the reverse happens during charging. The researchers also used scanning electron microscopy to observe the changes in the cathode's morphology, which revealed that the voids were present due to electrode shrinkage during discharge. While NiF_2 and SnF_4 may be more expensive than CuF_2 or FeF_3 , they could still be useful in FIBs if they have better rate capability or cycle life. Recent studies have investigated the electrochemical properties of Ni and Co as cathode materials for all-solid-state FIBs. It was found that thin-film Ni and Co cathodes can potentially offer improved cycle life compared to Cu, especially at high temperatures of around 150°C [30].

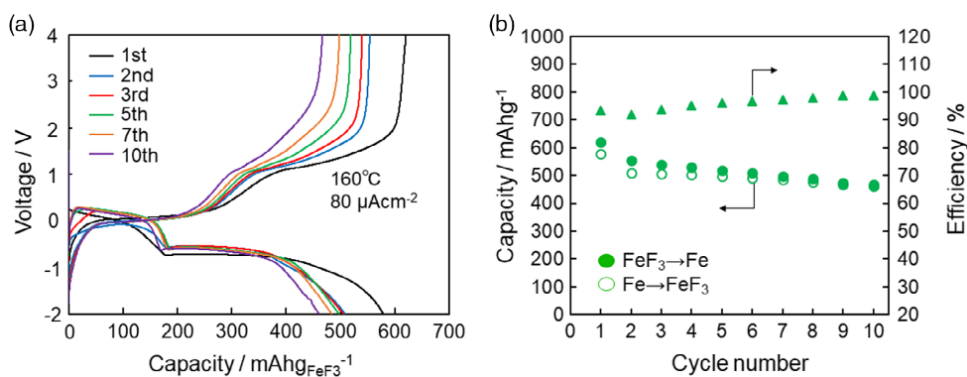


Figure 2.10: (a) Charge/Discharge profiles of FeF_3 electrode within all-solid-state. (b) Cycle properties of FeF_3 electrode within all-solid-state.[29]

Conversion-based anode materials

Conversion-type anode materials are made up of metals that have a low work function and can be classified into three major groups: alkali metals, alkaline earth metals, and rare earth metals. However, alkali metal fluorides are not suitable for use as anodes because they are more soluble in liquid electrolytes and their crystal structure has poor fluoride ion conductivity. This limits them to a single electron transfer per metal atom. Divalent and trivalent metal fluorides have lower solubility due to their higher charge density and smaller cation size, resulting in higher lattice energies. Unlike conversion cathodes, certain conversion anodes have crystal structures that prefer to conduct fluoride ions. [3]

PbF_2 is a widely used anion material with excellent fluoride ion conductivity. And elemental lead has a relatively low melting point, which can prevent the development of crystallization overpotentials that occur when PbF_2 is reduced during the charging of the cells. However, PbF_2 may not be suitable for a high-voltage battery as its voltage against an FGE is not very high ($\sim 3.6\text{ V}$). [6, 31]

Nowroozi et al. [31] demonstrated for the first time that a composite of Pb and PbF_2 could be used successfully as an anode in a fluoride-ion battery (FIB) when combined with an intercalation-based LaSrMnO_4 cathode. Based on DFT calculations, the

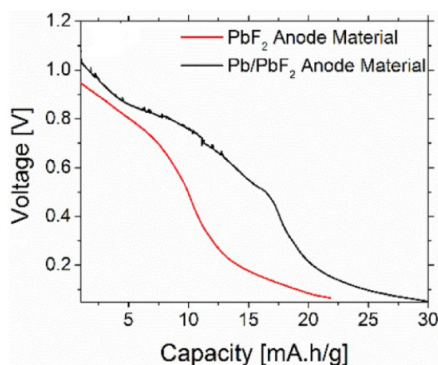


Figure 2.11: Discharging curves of $\text{LaSrMnO}_4/\text{PbF}_2$ and $\text{LaSrMnO}_4/\text{Pb-PbF}_2$ at 170°C with $I = -1.0 \mu\text{A}$. [31]

Pb/PbF_2 redox couple was predicted to have a redox potential of 2.26 V vs. Li/LiF , which makes it a suitable material for use as an anode in the FIB. In this research, Nowroozi also noticed that similar to the results observed with $\text{Mg} + \text{MgF}_2$ anodes, using the $\text{Pb} + \text{PbF}_2$ composite as the anode material instead of a composite containing only PbF_2 resulted in lower overpotentials and improved cycling performance as seen in Fig. 2.11. The use of the $\text{Pb} + \text{PbF}_2$ composite also led to more pronounced charging plateaus and higher phase fractions of fluorinated $\text{LaSrMnO}_4\text{F}_2$ in the cells. Even though the redox couple process occurring within the anode can significantly affect the charging and discharging behavior of the cells, the use of the $\text{Pb} + \text{PbF}_2$ composite showed promising results. So this same group decided to dig deeper. They investigated different conversion-based anodes, such as Pb and PbF_2 , Zn and ZnF_2 , and Mn and MnF_2 , against an intercalation-based cathode composite containing La_2CoO_4 as an active material [32]. The cells with $\text{Mn} + \text{MnF}_2$ anode showed a significant change in impedance response upon charging above a specific capacity, which was related to the strong volume decrease of MnF_2 when transformed to Mn ($\Delta V > 300\%$). This leads to a loss of contact between the active material and the electrolyte and carbon additive. On the other hand, the cells with $\text{Pb} + \text{PbF}_2$ anode composite exhibited better cycling performance and lower overpotentials compared to cells with $\text{Zn} + \text{ZnF}_2$ anode composite over prolonged cycling. The study attributed this to the stronger volume changes experienced by Zn and ZnF_2 during cycling.

CaF_2 is also an ideal conversion-type F_- anode. With a reduction potential of 0 V versus Li^+/Li and a capacity of 686.5 mAh g^{-1} . The fluorite crystal structure of CaF_2 makes it a favorable material for use in batteries as it undergoes minimal volume ($\sim 6\%$) changes during the process of (de)fluorination. The price of natural CaF_2 ($>97\%$) as “acid grade” Fluorspar is approximately $0.40 \text{ US}\$\text{kg}^{-1}$. [3]

Zhang et al. [33] have tested CaF_2 and MgF_2 as active anode materials for solid-state fluoride-ion batteries based on thin-film electrolyte. To improve the electronic conductivities, additives such as tin oxide, indium tin oxide, and carbon nanotubes were incorporated into the anode materials. The study found that using CaF_2 as the active anode material and carbon nanotubes as the conductive additive resulted in the best electro-

chemical performance in batteries. At a temperature of 160 °C, the battery using Bi-metal as the active cathode material achieved discharge capacities of 114 mAh g⁻¹ and 67 mAh g⁻¹ for the first and thirtieth cycles, respectively. MgF₂ has a comparable capacity with CaF₂, but it undergoes larger volume change (~40%) during defluorination and thus leads to huge contact issues. The researcher found that by incorporating a substantial quantity of electrolyte and carbon additives into the anode composition, it is possible to enhance both the electronic conductivity and F ion conductivity of CaF₂ and MgF₂ anode.

YF₃ and SrF₂ are materials with high energy densities generally just CaF₂ and MgF₂, but they pose different practical challenges. SrF₂ has a fluorite crystal structure and low volume change, but it has a lower capacity and a low redox potential that makes it difficult to use with many liquid electrolytes. Similarly, YF₃ has a more accessible anode potential, but it has a massive volume change and lacks an F⁻ conductive crystal structure. Davis et al.[34] demonstrated limited cycling of CeF₃ and LaF₃ in an organic F⁻ electrolyte, but they were unable to cycle CaF₂ in the same electrolyte due to its position at the edge of the electrochemical stability window. But LaF₃ and CeF₃ have tysonite-structured exhibiting a higher degree of reversible conversion compared to other anodes so that their reversible (re) conversion materials occur more readily.

In general, it seems that anodes composed of large cations and low-melting metals with high ionic conductivity in the metal fluoride state are more desirable for preserving structural integrity, which is crucial for achieving reversibility.

2.2.3. INTERCALATION-TYPE ELECTRODES

Another type of electrode is based on intercalation mechanism also called insertion mechanism or solid solution reaction. The structure of the host generally doesn't change in the material and the nature of bonding varies not so completely as in the conversion-type electrodes. Guest species are placed into empty spaces within the crystal structure of a stable host material that would not normally be occupied by any atoms or ions, such as interstitial sites or vacancies where anions would usually be found. Compared to the insertion reactions of Li⁺ in LIBs, the process of inserting F⁻ ions involves the oxidation of redox centers rather than their reduction. Intercalation-type electrodes have much lower volume change during reactions than conversion-type electrodes as ions can be reversibly inserted or removed from the host structure without significantly changing the basic crystal structure or amounts of the phase in the microstructure. Also, because of depending on the diffusion of only F⁻ without the formation and emigration of metal/metal fluorides interfaces, it has better cycling performances and superior rate capability. However, intercalation-type electrodes have lower specific capacities due to their heavier weight. The redox-inactive lattice atoms and the properties of accommodating fewer ions per redox-active species all contribute to the heavy mass.[3, 8, 6]

Intercalation-based cathode materials

There are three main types of potential intercalation-based cathode materials, Ruddlesden-Popper (K₂NiF₄-type structure), Schafarzikite (MSb₂O₄) and (anion-deficient) perovskite (AMO_{3-y}). Notably, MXenes are a type of cathode material that relies on intercalation and have demonstrated considerable potential for use in both lithium-ion batteries (LIBs)

and supercapacitors. Recently, people have been interested in the performance of MXenes as a cathode material for rechargeable FIBs.

The Ruddlesden-Popper structure is a type of crystal structure regarded as a perovskite-related structure. Its general formula is represented as $A_{n+1}M_nO_{3n+1}$ (or $(AMO_3)_nAO$), where 'n' indicates the number of layers of MO_6 that are connected through their vertices [8]. The structure consists of n perovskite layers that are stacked between rock-salt AO layers, which are arranged along the c-axis [8]. A typical structure exists as K_2NiF_4 (A_2MO_4) structure when $n = 1$. The unoccupied spaces for anions within the rock salt-type interlayers are well-suited for hosting fluoride ions as seen in Fig.2.12. This type of compound has the ability to accommodate a maximum of 2 fluoride ions for each unit of their chemical formula, which leads to theoretical capacities typically ranging from 130 to 160 mAh g^{-1} .

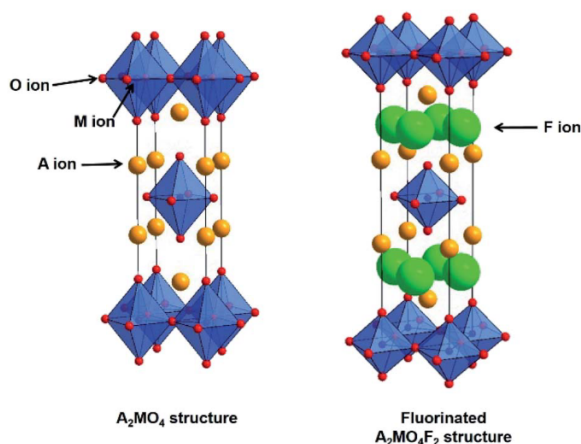


Figure 2.12: Schematic illustration of the $n = 1$ Ruddlesden-Popper (A_2MO_4) structure (left) and fully fluorinated $A_2MO_4F_2$ structure (right). [8]

One of the most promising intercalation-type electrode materials is $LaSrMnO_4$ which belongs to the Ruddlesden-Popper type. In 2017, Nowroozi et al.[31] reports on the investigation of $LaSrMnO_4$ with K_2NiF_4 type structure against PbF_2 anodes and shows that fluoride intercalation proceeds stepwise to form $LaSrMnO_4F$ and $LaSrMnO_4F_{2-x}$. $LaSrMnO_4$ is comprised of ABX_3 perovskite-type layers and AX rock salt subunits that alternate with each other. The interface between these layers contains significant interstitial sites that are capable of accommodating fluoride anions, as illustrated in Fig.2.13. The discharging capacity is around 20-25 mAh g^{-1} . According to the density functional theory, the first ($LaSrMnO_4 \rightarrow LaSrMnO_4F$) and second ($LaSrMnO_4F \rightarrow LaSrMnO_4F_{2-x}$) intercalation step are observed at approximately 1 and 2 V, respectively. It was shown that $LaSrMnO_4F$ maintains its structural stability during the removal of fluoride ions through galvanostatic discharging to -3 V against a $Pb-PbF_2$ electrode. This effectively compensates for overpotentials and allows for almost complete recovery of $LaSrMnO_4$ without fluorine, with a discharge capacity of approximately 100 mAh g^{-1} . It is noticed that this is the first report demonstrating the feasibility of extracting fluoride ions selectively from

an oxyfluoride matrix.

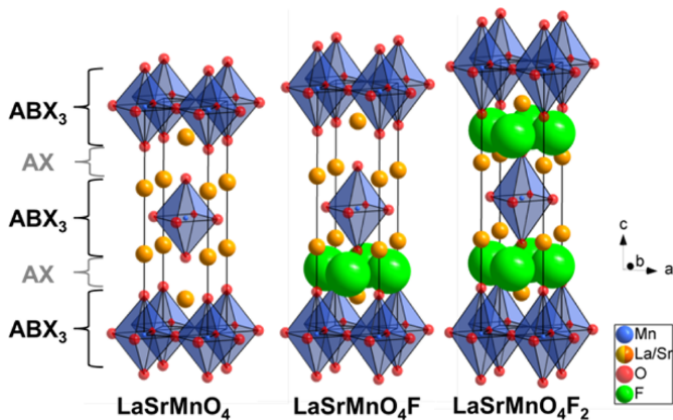


Figure 2.13: Schematic illustration of the structure of LaSrMnO_4 (left) in comparison to partly fluorinated $\text{LaSrMnO}_4\text{F}$ (middle) and fully fluorinated $\text{LaSrMnO}_4\text{F}_2$ (right). [31]

Schafarzikite-type compounds, which have the general formula MSb_2O_4 , exhibit a one-dimensional tunnel structure with tetragonal symmetry (space group $P4_2/\text{mbc}$). This structure is composed of chains of edge-linked MO_6 octahedra that are linked along the $[0\ 0\ 1]$ direction, and these chains are connected through trigonal pyramidal SbO_3 units (Fig. 2.14). [8]

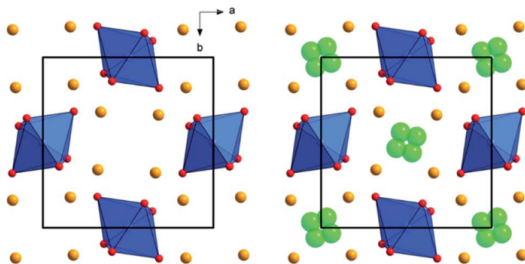


Figure 2.14: Schematic illustration of the non-fluorinated MSb_2O_4 (left) and fluorinated $\text{MSb}_2\text{O}_4\text{F}_y$ (right) Schafarzikite-type structure. Sb orange, M (Fe, Co) blue, O red, F (partially occupied to ~15%) green. [35]

For Schafarzikite-type cathodes, Zaheer et al. [36] demonstrated that the submicrometer-sized

FeSb_2O_4 particles exhibit reversible and uniform topochemical insertion and desorption of fluoride ions through bulk diffusion at room temperature in 2020. The insertion is confirmed by the formal oxidation of iron centers from Fe^{2+} to Fe^{3+} , resulting in a lattice volume contraction of less than 1% at a capacity of one F ion per iron center. Notably, this insertion process is observed to occur uniformly throughout the FeSb_2O_4 particles. While Schafarzikite compounds exhibited unsatisfactory cycling behavior when used as the cathode material with solid electrolytes in FIBs, this may suggest their potential util-

ity in battery systems that employ liquid electrolytes under ambient conditions [35].

Perovskite-type compounds with anionic deficiencies, such as $\text{BaFeO}_{2.5}$ and SrFeO_2 , have been studied as promising cathode materials for intercalation-based fluoride-ion batteries (FIBs). In a study conducted by Clemens et al. [37], $\text{BaFeO}_{2.5}$ was tested as an anode material against Ce/CeF_3 or Mg/MgF_2 using $\text{La}_{0.9}\text{Ba}_{0.1}\text{F}_{2.9}$ electrolyte at 150°C . The cell was charged up to 4.0 V (vs. CeF_3), which resulted in a capacity of about 80 mAh g^{-1} . X-ray diffraction experiments showed that the cell volume per BaFeX_{3-y} unit decreased during electrochemical fluorination, resulting in oxidatively fluorinated compounds. Also, a change in symmetry from a vacancy-ordered modification to a cubic perovskite is observed. These structural changes were consistent with chemical fluorination using F_2 gas, but the discharge capacities of the cell against CeF_3 were only negligible, around 6 mAh g^{-1} .

In 2019, Nowroozi [38] reported that at the applied experimental conditions ($T = 170^\circ\text{C}$), the active cathode material SrFeO_2 experiences an oxidation reaction due to the poor chemical stability towards other components, resulting in the formation of a compound that closely resembles SrFeO_2F .

In 2020, Yang et al. [39] conducted a comprehensive analysis of key characteristics of Ti- and V-based MXenes (M_2CH_2) to evaluate their potential as cathode materials for rechargeable fluoride-ion batteries (FIBs). This included studying their energetic and thermodynamic stability, electronic properties, ionic mobility driven by strain, average open circuit voltage, and theoretical specific capacity. The study found that Ti_2CH_2 MXene has a lower energy barrier for F^- diffusion compared to V_2CH_2 MXene over a large range of strains. Moreover, controlling the compression strain can enhance fluoride-ion mobility on Ti_2CH_2 due to changes in its surface state. The results also revealed that Ti_2CH_2 has a higher storage capacity (488 mAh g^{-1}) and open circuit voltage (4.62 V) for F^- intercalation than V_2CH_2 . Furthermore, ab initio molecular dynamics simulations showed that $\text{F}_2\text{Ti}_2\text{CH}_2$ is thermo-dynamically stable at 500 K , while $\text{F}_2\text{V}_2\text{CH}_2$ generates HF compounds at 300 K , suggesting that Ti_2CH_2 is better suited for severe conditions. Considering these factors, the study concludes that Ti_2CH_2 could be a promising cathode material for rechargeable fluoride-ion batteries due to its flexibility and strain controllability.

Intercalation-based anode materials

Anode materials based on intercalation have received little attention in research thus far.

K. Wissel et al. [40] prepared Ruddlesden-Popper compounds containing a large amount of low-valence Ti through a series of topological chemical reactions. By reacting Ruddlesden-Popper fluoride with NaH (a hydride-based reduction method), F^- was selectively extracted from the oxyfluoride. The compound $\text{Sr}_2\text{TiO}_3\text{F}_2$ can undergo reduction to a low valent Ti^{2+} compound at relatively low temperatures when sodium hydride (NaH) is used as a reducing agent. The authors have shown that oxyfluorides are more effective than oxides in lowering the reduction temperatures of titanates. Studies have been conducted on the chemical defluorination properties of $n = 1$ $\text{Sr}_2\text{TiO}_3\text{F}_2$, $n = 2$ $\text{Sr}_3\text{Ti}_2\text{O}_5\text{F}_4$, and $n = 1$ $\text{La}_2\text{NiO}_3\text{F}_2$. The NaF generated by the reaction has a high lattice energy, resulting in a negative electrode potential of less than 1 V (vs. Li/LiF) for the prepared anode material.

Hartman and Mishra [41] proposed the utilization of layered electrides as intercalation anodes, which have significantly lower electrode potentials. Electrides refer to compounds that contain a stoichiometric imbalance between anions and cations, leading to the presence of excess electrons occupying interstitial sites in the crystal as delocalized "anionic" electrons (i.e., $[\text{Ca}_2\text{N}]^+ \text{e}^-$, $[\text{Y}_2\text{C}]^{2+} \text{e}^{2-}$). The "nearly free" electrons in these materials have work functions similar to the corresponding metal, leading to extremely low redox potentials. For instance, the $\text{Ca}_2\text{N}/\text{Ca}_2\text{NF}$ redox couple was found to have an estimated potential close to 0 V vs. Li^+/Li . Due to their lower formula weight, layered electrides exhibit much higher one-electron gravimetric capacities compared to fluoride intercalation electrodes based on oxides such as $\text{Sr}_2\text{TiO}_3\text{F}_2$, LaSrMnO_4 , and FeSb_2O_4 . It is worth mentioning that the synthesis of layered Y_2CF_2 has already been achieved, and it can be classified as an MXene material [42].

2.2.4. METAL OXYFLUORIDE AND METAL OXIDE ELECTRODE MATERIALS

Recently, transition metal oxyfluorides, a type of mixed-anion electrode material, have recently gained more and more attention as potential candidates for the development of next-generation rechargeable batteries, including lithium-ion batteries, sodium-ion batteries, etc [43]. However, there are only a few articles reporting the transition metal oxyfluoride materials used as electrodes within fluoride-ion batteries. These metal oxyfluoride electrodes are potential materials as active materials since they have similarities with conversion or insertion electrodes but they are a derivative of the latter ones, with better properties. Transition metal oxyfluorides are different from transition metal oxides or fluorides as these types of materials achieve improved properties, including high capacity, high voltage, good conductivity, good cycling stability, optical and magnetic properties, and catalytic properties. These can be due to the combination of the benefits of fluorides and the advantages of oxides. Metal fluorides are an attractive option, as the M-F bond is highly ionic, which allows for the potential of achieving high redox potentials. However, pure metal fluorides are not conductive and have slow kinetics and low efficiency [44]. Metal oxides have been widely studied due to their flexible and diverse redox chemistry, which is determined by the characteristics of the ligand (oxygen) bond (M-O bond), however, they have not been widely used in fluoride ion batteries. Metal oxyfluorides represent a good compromise between oxides and fluorides, and the anion substitution changes the electronic state of the metal and crystal field adjusting the structures as well as the physicochemical properties. The difference in properties between metal oxyfluorides and metal oxides/fluorides results from changes in ionic bonding and valence state. Also, metal oxyfluorides itself have improved electronic conductivity, and metal cations with valence change could be beneficial to the electrodes. Deng [43] compares FeOF with FeF_2 illustrating that the substitution of F with O can move the F metal off-center towards the O atoms as Fig.2.15. FeOF combines the benefits of fluorides and oxides. The fluorides have high reaction potential and high output voltages while the oxides have improved capacity and cycling stability and the covalent Fe-O bonds enhance electronic conductivity in this highly ionic fluoride structure.

In 2017, while Grenier et al. [25] experimented on BiF_3/Bi redox couple and $\text{Bi}-\text{BiF}_3-\text{LBF}-\text{C}$ composite, they also demonstrated the formation of successive bismuth oxyfluoride phases at the Bi particle surfaces due to the increasing F/O ratio through

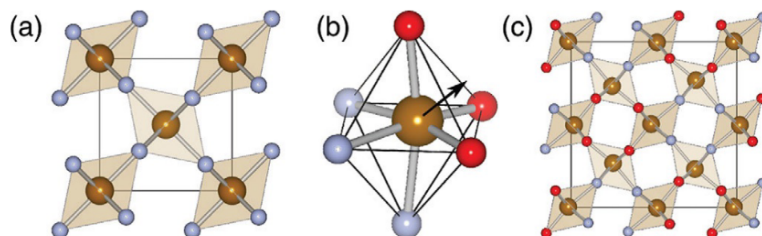


Figure 2.15: (a) FeF_2 and (b,c) FeOF . [43]

synchrotron XRD and PDF analysis. As the fluorination increases, the Bi-oxide initially forms oxygen-rich compositions such as BiOF ($F/O = 1$), which then gradually transform into phases with higher F/O , such as $\text{Bi}_7\text{F}_{11}\text{O}_5$ ($F/O = 2.2$), $\text{BiO}_{0.55}\text{F}_{1.9}$ ($F/O = 3.45$), and eventually BiF_3 , see Fig.2.16. It is possible that $\text{BiO}_{0.1}\text{F}_{2.8}$ ($F/O = 28$) is also present both in the anode and cathode, but it has a tysonite-type structure which has similar XRD and PDF patterns with LBF. The excellent reversible behavior and high capacity (approximately 190 mAh g^{-1}) can be explained by the mobility of fluoride ions within these various oxyfluoride phases. excess Bi oxyfluorides

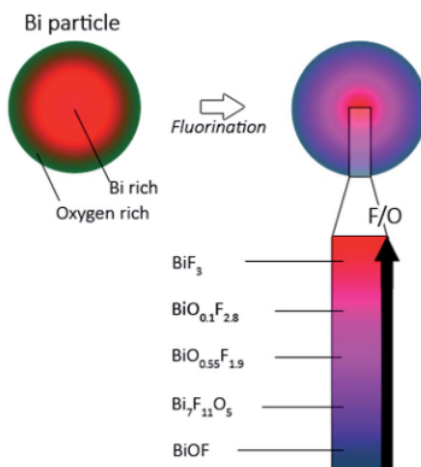


Figure 2.16: The formation of successive bismuth oxyfluoride phases due to the increasing F/O ratio at the Bi particle surfaces. [25]

In 2020 Takami et al. [45] reported a $\text{Bi}_{0.7}\text{Fe}_{1.3}\text{O}_{1.5}\text{F}_{1.7}$ (BFOF) phase synthesized via a non-topochemical reaction with a fluorination agent polyvinylidene difluoride (PVDF). Researchers use Pb as the counter electrode and $\text{Ce}_{0.5}\text{Ba}_{0.05}\text{F}_{2.95}$ as the electrolyte. The utilization of BFOF as a cathode in fluoride-ion batteries (FIBs) results in a discharge capacity of 360 mAh g^{-1} and a charge capacity of 225 mAh g^{-1} at 140°C . Through magnetization and x-ray diffraction measurements, it has been confirmed that F ions are transferred from the cathode to the Pb counter electrode during discharge, and vice versa during charge. During discharging, a phase transition to Bi and valence change

of Fe have been observed. Researchers provide valuable insights for the advancement of multinary oxyfluorides as potential cathodes for FIBs.

In 2023, Liu et al. [46] also researched oxyfluoride cathodes composed of Bi elements. They induced the conductive $\text{Bi}_7\text{F}_{11}\text{O}_5$ phase in the BiF_3 crystal by annealing treatment. This multi-phase cathode material shows an improved electronic conductivity reaching $1.6 \times 10^{-4} \text{ S cm}^{-1}$ which is 10 times higher than the BiF_3 ($2.9 \times 10^{-5} \text{ S cm}^{-1}$) indicating that $\text{Bi}_7\text{F}_{11}\text{O}_5$ phase facilitates electron transfer. The cell $\text{BiF}_3/\text{Bi}_7\text{F}_{11}\text{O}_5|\text{PbSnF}_4|\text{Sn}$ reaches a remarkable reversible capacity of 177.9 mAh g^{-1} and sustained a capacity of 132.7 mAh g^{-1} even after 50 cycles (Fig. 2.17). The introduction of $\text{Bi}_7\text{F}_{11}\text{O}_5$ caused a shift in the Bi 4f peak towards a higher energy region compared to BiF_3 , indicating that the coordination environment of Bi^{3+} has undergone a change.

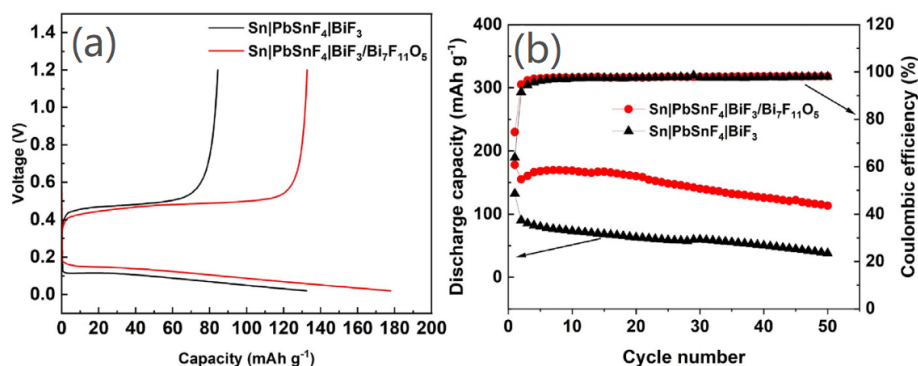


Figure 2.17: (a) The initial GCD curves of $\text{Sn|PbSnF}_4|\text{BiF}_3/\text{Bi}_7\text{F}_{11}\text{O}_5$ and $\text{Sn|PbSnF}_4|\text{BiF}_3$ obtained at RT. (b) Cycling performances of $\text{Sn|PbSnF}_4|\text{BiF}_3/\text{Bi}_7\text{F}_{11}\text{O}_5$ and $\text{Sn|PbSnF}_4|\text{BiF}_3$ at RT. [46]

In 2022, Wang et al. [47] presented a new intercalation material, $\text{Sr}_3\text{Fe}_2\text{O}_5\text{F}_2$, which has a Ruddlesden-Popper structure and can be used as a cathode material for FIBs. This material has both interstitial sites and anion vacancies that act as 3D percolation sites for the accommodation of fluoride ions. The material has a high capacity of 118 mAh g^{-1} and remains stable over 70 cycles as seen in Fig. 2.18b. Charge compensation occurs through $\text{Fe}^{2+}/\text{Fe}^{3+}$ redox reactions during charging and discharging. The crystal structure changes during the charging process from $\text{Sr}_3\text{Fe}_2\text{O}_5\text{F}_{0.46}$ to $\text{Sr}_3\text{Fe}_2\text{O}_5\text{F}_2$, utilizing 3D percolation sites with a small volume change of approximately 0.17%, and subsequently changes to $\text{Sr}_3\text{Fe}_2\text{O}_5\text{F}_3$ with a P4/mmm symmetry, utilizing interstitial sites with a large volume change of approximately 11%. During the charging process, the charge compensation from $\text{Sr}_3\text{Fe}_2\text{O}_5\text{F}_{0.46}$ to $\text{Sr}_3\text{Fe}_2\text{O}_5\text{F}_{1.5}$, from $\text{Sr}_3\text{Fe}_2\text{O}_5\text{F}_{1.5}$ to $\text{Sr}_3\text{Fe}_2\text{O}_5\text{F}_2$, and from $\text{Sr}_3\text{Fe}_2\text{O}_5\text{F}_2$ to $\text{Sr}_3\text{Fe}_2\text{O}_5\text{F}_{2.5}$ was achieved by iron ions, iron and oxide ions, and oxide ions, respectively, as shown in the charge/discharge profile in Fig. 2.18a.

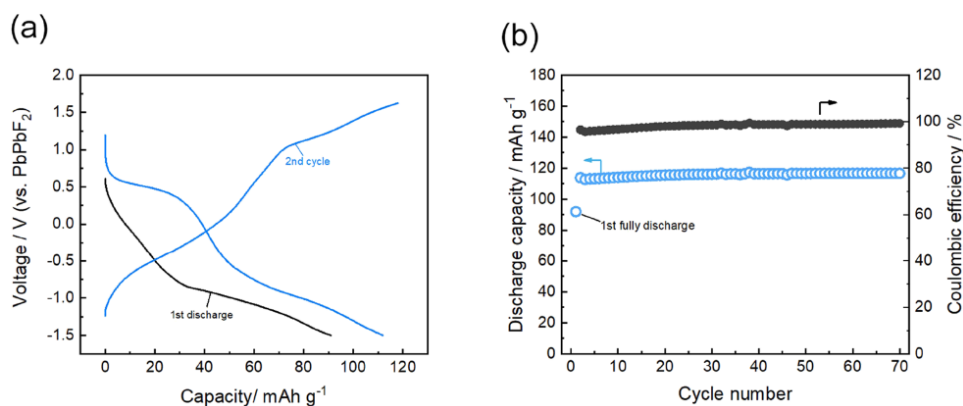


Figure 2.18: (a) Charge/discharge profiles of $\text{Sr}_3\text{Fe}_2\text{O}_5\text{F}_2$ for the first two cycles. (b) Capacity retention upon cycling of $\text{Sr}_3\text{Fe}_2\text{O}_5\text{F}_2$ under a current density of 5 mA g^{-1} . [47]

Motohashi et al. [48] introduced oxide-ion vacancy ($\text{V}_{\text{O}}^{\bullet\bullet}$), fluoride-ion vacancy ($\text{V}_{\text{F}}^{\bullet}$) and interstitial fluoride-ion (F_i') into Ruddlesden-Popper oxyfluoride $\text{Ba}_2\text{ScO}_3\text{F}$. It is found that introducing fluoride-ion defects (fluoride-ion vacancy and interstitial fluoride-ion) can enhance the ionic conductivities in $\text{Ba}_2\text{ScO}_3\text{F}$ while introducing oxide-ion vacancy can not improve it. The findings indicate that the fluoride ion can move through the interstitial spaces of the rock-salt structure in Ruddlesden-Popper oxyfluorides. The results also suggest that modifying the types of anion defects in the material could be a useful strategy for designing fast fluoride-ion conductors using mixed anion compounds.

The experimental visualization of anion-diffusion pathways in $\text{La}_{0.9}\text{Sr}_{0.1}\text{O}_{0.45}\text{F}_2$ was produced by Hibino et al. [49] in 2021. A three-dimensional network of anion-diffusion pathways and interstitial diffusion mechanisms are demonstrated. The migration of anions uses both the interstitial 32f X2 and lattice 8c X1 sites, which form curved 8c-32f-32f-8c pathways. This study provides clear evidence that the high conductivity of anions in LaOF-based materials is primarily due to the movement of anions through the interstitial sites. In the case of one-dimensional (1-D) diffusion, the presence of defects that obstruct the diffusion path can restrict the performance of the intercalation electrode. This is why two-dimensional (2-D) or three-dimensional (3-D) host structures are often favored, as they offer a larger diffusion pathway that is less likely to be impeded by defects.

Creating straightforward methods for producing transition metal oxyfluorides remains a challenging endeavor, particularly in terms of scalability and achieving high purity levels. In this project, instead of directly employing metal oxyfluorides as the cathode material, we utilize metal oxide materials as our cathode electrode. During the electrochemical reaction, the metal oxide undergoes fluorination, resulting in the formation of metal oxyfluoride materials.

Takami [45] illustrated that as oxides are generally more stable than fluorides, oxyfluorides are typically synthesized via topotactic reactions, which involve the fluorination of oxide precursors. LaOFeAs , for instance, can be transformed into $\text{LaO}_{1-x}\text{F}_x\text{FeAs}$ through fluorination. F_2 gas, NH_4F and PVDF are commonly used for fluorinating precursors to

produce single-phase compounds. PVDF is advantageous as it helps prevent the formation of metal fluoride impurities and the oxidation of metal ions. Due to their high chemical stability, there are very few non-topotactic reactions that use fluoride starting materials for the synthesis of fluorides and oxyfluorides.

In 2021, Wissel et al. [50] reported that RP-type $A_{n+1}B_nO_{3n+1}\square_2$ compounds are made up of alternating layers of n ABO_3 perovskite layers and one AO rock salt layer. The perovskite layers have fully occupied anion sites, while the rock salt layers contain interstitial vacancies \square that can be filled with additional anions (e.g., with oxide ions in over-stoichiometric oxides or with fluoride ions for the synthesis of oxyfluorides). Different methods of fluorination can be used to introduce additional fluoride ions into the interstitial vacancies of RP-type $A_{n+1}B_nO_{3n+1}\square_2$ compounds. Oxidative fluorination involves the use of fluorine gas or electrochemical fluorination to intercalate fluoride ions into the interstitial site, resulting in the formation of $A_{n+1}B_nO_{3n+1}F_x\square_{2-x}$ with $x \leq 2$. Non-oxidative fluorination, on the other hand, involves the use of fluorine-containing polymers like PVDF to intercalate two fluoride ions for every substituted oxide ion, forming $A_{n+1}B_nO_{3n+1-x}F_{2x}\square_{2-x}$ where $0 < x \leq 2$. They get new compounds $La_2NiO_3F_{2-\Delta}$ containing Ni^{2+} and $La_2NiO_3F_{2+\Delta}$ containing Ni^{3+} using galvanostatic charging and discharging of Ruddlesden-Popper type $La_2NiO_3F_2$ within all-solid-state FIBs. $La_2NiO_3F_2$ can be synthesized by topochemical fluorination of La_2NiO_{4+d} using PVDF. The structural reversibility of re-fluorinating and re-defluorinating is also demonstrated. And the reversible battery operation of full cell $La_2NiO_3F_2[La_{0.9}Ba_{0.1}F_{2.9}]Pb/PbF_2$ is demonstrated over up to 50 cycles. The structural alterations observed in this study were compared to those resulting from other topochemical modification methods, such as reduction using hydrides and oxidative fluorination with F_2 gas. Electrochemical defluorination produces hydride-free materials, unlike hydride-based reactions. Moreover, electrochemical fluorination produces considerably higher phase fractions of the fluorinated monoclinic phase ($La_2NiO_3F_3$) than chemical fluorination of $La_2NiO_3F_2$ using highly oxidizing F_2 gas. These all prove that electrochemical methods provide secure and manageable ways to produce new phases that cannot be obtained through other topochemical approaches.

Also, there are some transition metal oxides that can be fluorinated into oxyfluorides during reversible battery operations, which also leads to some new considerations.

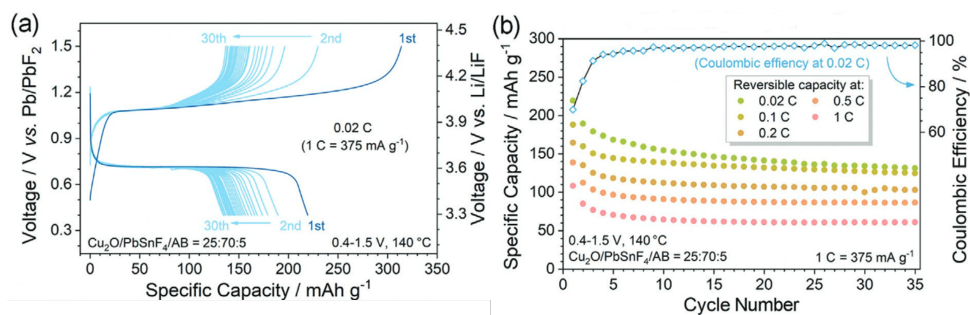


Figure 2.19: (a) Charge/discharge profiles of Cu_2O for cycles 1–35 at 0.02 C, 140 °C. (b) Cyclabilities of Cu_2O at various C rates, 140 °C. [19]

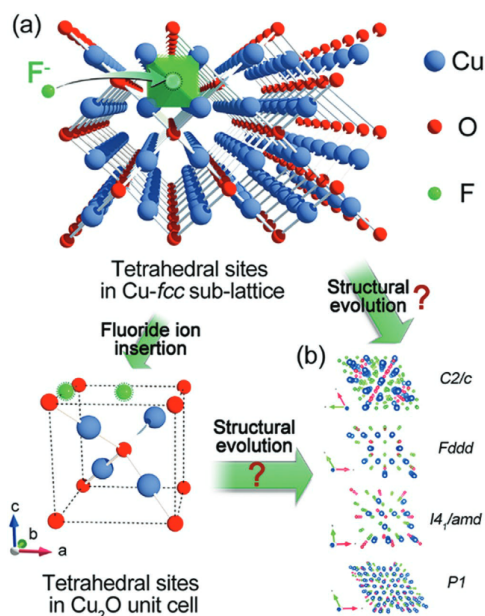
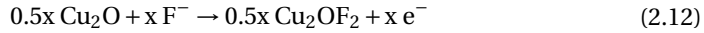


Figure 2.20: Probable tetrahedral sites (a) and configurations for F intercalation (b). [19]

In 2021, Zhang et al. [19] used cuprous oxide (Cu_2O) as a cathode material for all-solid-state fluoride-ion batteries while using PbSnF_4 as the electrolyte and Pb/PbF_2 as the anode. Cu_2O has highly reversible (de)fluorination behavior and a high theoretical capacity of 375 mAh g^{-1} (Fig. 2.19a). It has non-close-packed Cu-O configurations and an enhanced rate capability compared with Cu/CuF_2 cathode as it can reach 110 mAh g^{-1} at 1C during first discharge. And the KJMA equation suggested that phase boundary movement was the rate-determining step. The first discharge capacity is approximately 220 mAh g^{-1} (Fig. 2.19b), however, fast capacity fading is observed in the first five cycles ascribed to partially irreversible amorphization upon charging. Three presumptions regarding the possible structures of the charged products are proposed. First, the "topotactic Cu_2O " hypothesis proposes that the basic arrangement of copper and oxygen atoms in the material remains the same, but fluoride ions occupy the anionic vacancies in Cu_2O . The original structure of the starting material, $\text{Pn}\bar{3}\text{m-Cu}_2\text{O}$, consists of linear arrangements of oxygen and copper atoms with O-Cu-O as units. The copper atoms form a face-centered cubic sub-lattice, while some of the tetrahedral sites in this sub-lattice are occupied by oxygen atoms as seen in Fig. 2.20a. The unoccupied sites produce continuous channels in the $\langle 100 \rangle$ direction. But if all of the tetrahedral sites were occupied by fluorine atoms, the resulting lattice structure, Cu_2OF_3 , would contain six fluorine atoms per unit lattice. However, Cu_2OF_3 has not been proved to be thermodynamically stable. The second presumption is that the reaction expressed by Eq. 2.12 produces the imagined fully charged product, Cu_2OF_2 , which has not been synthesized and reported yet. Thus, according to the theoretical calculations (from *MaterialsProject*), four models of Cu_2OF_2 are illustrated in Fig. 2.20b. The last presumption is that the cal-

culated Cu_2OF_2 are considered to be thermodynamically unstable, and the immediate conversion products are CuF_2 and CuO nanocomposites. No reports about reactions between CuF_2 and CuO have been found so far.



Also in 2021, Bashian et al. [51] reported the electrochemical fluorination of A-site vacant perovskite ReO_3 using both high-temperature solid-state cells with a Ba-doped LaF_3 electrolyte and room-temperature liquid electrolytes. They found that ReO_3 can be oxidized by approximately 0.5 equiv of electrons while exposed to fluoride-rich electrolytes. Their findings indicate that the removal of electrons from the strongly hybridized Re-O orbitals at the Fermi level leads to partial oxidation of both Re and O. The compensation of charges is through the integration of fluoride ions into the electrode composition. The incorporation of fluoride ions leads to structural changes, as some Re atoms seem to move from octahedral sites to newly formed tetrahedral sites. The density functional theory (DFT) calculations showed that the mechanism for charge compensation is not as straightforward as the insertion of F-ions into the A-site of the perovskite structure, and the intercalated forms of FReO_3 are considered thermodynamically unstable. Bashian et al. gave a most likely explanation which is that F-ions intercalate onto the A-site of the perovskite host but quickly begin to decompose to the more thermodynamically favored phases over time. They also found that the fluorinating process of Re_3 is only partially reversible.

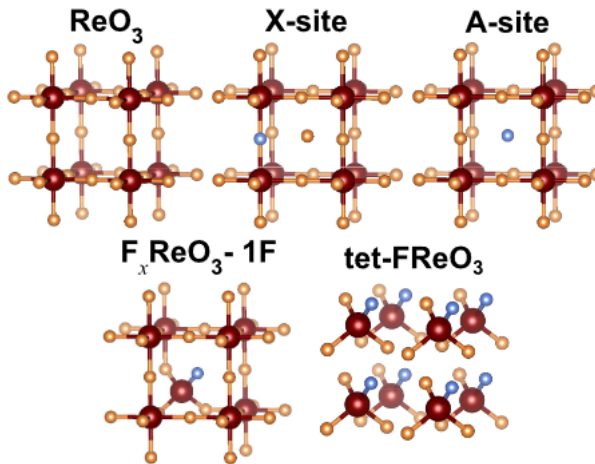


Figure 2.21: Models for the fluorination of ReO_3 with Re shown in red, oxygen in orange, and fluorine in blue. The tet-F ReO_3 model, where all of the Re ions migrate to the tetrahedral positions, can be considered an end member to the $\text{F}_x\text{ReO}_{3-1}\text{F}$ [51]

In this project, we have chosen the most common transition metal oxides, Cu_2O , FeO , and Mn_2O_3 , as the cathode materials for solid-state fluoride-ion batteries to investigate their electrochemical properties. This selection is motivated by the fact that many oxide materials have not yet been studied as electrode materials for fluoride-ion batteries. The

reason for opting for a solid-state battery system rather than a liquid-state system is due to the enhanced safety and potential for higher energy density and cycle life associated with solid-state batteries. Further explanation regarding the application of solid-state electrolytes in fluoride-ion battery systems will be provided in the following section.

2.3. SOLID ELECTROLYTES USED IN FLUORIDE-ION BATTERIES

Compared with liquid electrolyte batteries, all-solid-state batteries (ASSBs) have certain advantages in terms of safety. Solid F-ion electrolytes offer significant advantages in terms of achieving wide electrochemical stability windows. They are easier to work with due to their lower chemical reactivity, which enhances safety and simplifies the production process. Despite the relatively large ionic size of Fluoride ions ($\sim 1.33 \text{ \AA}$), it displays considerable mobility in solids, which is attributed to its monovalent nature and low charge density. Solid electrolytes (SEs) should fulfill the following criteria [2, 8]: (1) High ionic conductivity to ensure the fast diffusion of ions to electrodes. (2) Low electronic conductivity to avoid battery short circuits and self-discharge. (3) A wide electrochemical window to ensure electrochemical stability resulting in good cyclability. (4) It should be chemically compatible with electrode materials to ensure the rapid transmission of electrically active substances on the interface. (5) It should have certain mechanical properties, such as sufficient flexibility and softness, etc. Now, many of the solid electrolytes studied for FIBs lack sufficient conductivity for practical operation at room temperature, often requiring the cells to be operated at temperatures of $150 \text{ }^\circ\text{C}$ or higher [52].

Generally, solid electrolytes can be broadly categorized into three classes of compounds: tysonite-type systems, fluorite-type systems, and systems containing lead and tin. Tysonite-type ones which can be described by the formula $R_{1-x}M_xF_{3-x}$ (R is a rare-earth element such as La, Ce, Sm, and M is a divalent element such as Ba, Ca, Sr), their improved ionic transport is achieved by introducing F^- vacancies in RF_3 [52]. $La_{0.9}Ba_{0.1}F_{2.9}$ is a typical fluorite-type electrolyte having a conductivity of $10^{-6} \text{ S cm}^{-1}$ at $25 \text{ }^\circ\text{C}$ [52], which is insufficient for room-temperature cell operation. Fluorite-type systems which can be described as $A_{1-x}R_xF_{2+x}$ (A is an alkaline-earth element such as Ca, Sr, Ba, and R is a rare-earth element such as La, Sb). Their ionic transport relies on interstitial F^- . Take $Ba_{0.6}La_{0.4}F_{2.4}$ and $Ba_{0.7}Sb_{0.3}F_2$ for example, they exhibit low conductivities of $10^{-7} \text{ S cm}^{-1}$ at room temperature, which are also not satisfactory. Compounds containing lead or tin such as $BaSnF_4$ and $PbSnF_4$ (P4/nmm structure) exhibit high conductivity at room temperature, $10^{-4} \text{ S cm}^{-1}$ and $10^{-3} \text{ S cm}^{-1}$, respectively [52]. However, their ESWs are so narrow. In general, the first two classes often require high temperatures (approximately higher than $150 \text{ }^\circ\text{C}$), and fluorides containing lead and tin behave better at room temperature but have narrow ESWs [3]. The primary challenge in developing room temperature (RT) solid-state fluoride ion batteries (FIB) lies in creating a solid electrolyte capable of transporting fluoride ions with significant ionic conductivity at RT, while also maintaining a wide electrochemical stability window (ESW). A detailed introduction to some solid-state electrolytes applied in fluoride-ion batteries will be provided next.

The ionic conductivity of rare earth metal fluoride is very small without doping, however, after doping with alkali earth metals (Ba, Ca, and Sr), the F^- vacancies will be introduced. These F^- vacancies improve the mobility of F^- in the fluoride sublattice, and the ionic conductivity of the tysonite-type electrolyte is much improved. There-

fore, the conduction mechanism observed in tysonite-type structures is primarily based on a vacancy-type mechanism caused by Schottky defects [8]. Reddy et al. [53] prepared $\text{La}_{0.9}\text{Ba}_{0.1}\text{F}_{2.9}$ electrolyte with ionic conductivity of $2.8 \times 10^{-4} \text{ S cm}^{-1}$ (160 °C) by ball milling method. Subsequently, the ionic conductivity was further increased to $8.3 \times 10^{-4} \text{ S cm}^{-1}$ (160 °C) by sintering at high temperatures. They believe that the high-temperature sintering process will produce grain boundary fusion, reduce the grain boundary ratio, and increase the ionization conductivity. Bhatia et al. [54] prepared $\text{La}_{0.95}\text{Ba}_{0.05}\text{F}_{2.95}$ solid solution by a facile wet chemical method, and after sintering at 800 °C for 20 hours, the ionic conductivity was greatly improved to $1.26 \times 10^{-4} \text{ S cm}^{-1}$ (60 °C). This conductivity is approximately one order of magnitude higher than that of the pellet in its as-prepared state and about twice as high as the conductivity observed in sintered ball-milled batches. XRD and electrochemical impedance spectroscopy (EIS) analysis showed that compared with solid ball milling, the material prepared by the facile wet chemical method has lower impurity content, which is one of the reasons for the improved ionic conductivity.

After doping with heterovalent metal (rare-earth metal, R), the general formula of the fluorite-type material can be expressed as $\text{A}_{1-x}\text{R}_x\text{F}_{2+x}$. In order to ensure electrical neutrality, F^- in the interstitial site is produced. Therefore, the conduction mechanism is interstitial conduction. Mohammad et al. [55] prepared the BaF_2 solid solution doped with SbF_3 by ball milling and sintering. At 160 °C, the ionic conductivity of $\text{Ba}_{0.7}\text{Sb}_{0.3}\text{F}_{2.3}$ was as high as $4.4 \times 10^{-4} \text{ S cm}^{-1}$, which was twice as much as $\text{Ba}_{0.7}\text{La}_{0.3}\text{F}_{2.3}$. This may be caused by the lone pair electrons of Sb^{3+} , but the specific mechanism is not clear. In order to better understand the dispersion mechanism of F^- in fluorine-type fluorides, Mori et al. [56] accurately determined the structural information of $\text{Ba}_{1-x}\text{La}_x\text{F}_{3-x}$ through ^{19}F nuclear magnetic resonance and neutron diffraction tests, and obtained through the maximum entropy method (MEM) simulation calculation that the diffusion path of F was $\text{F}_1 - [\text{F}_2 - \text{F}_2] - \text{F}_1$. Along this path, La^{3+} replaces Ba^{2+} , introducing excess F^- at F_2 , which is biased away from the O center. This diffusion path can be explained by the interstitialcy diffusion mechanism.

Certain rare-earth-based fluorides, such as $\text{Ce}_{0.975}\text{Sr}_{0.025}\text{F}_{2.975}$ and $\text{Sm}_{0.95}\text{Ca}_{0.05}\text{F}_{2.95}$, exhibit high ionic conductivity on the order of $10^{-4} \text{ S cm}^{-1}$ even at RT [57, 58]. However, the reported high ionic conductivity in these compounds was achieved only using sintered discs, which pose challenges for integration into a full cell configuration. This is due to the mechanical incompatibility between sintered discs and ball-milled polycrystalline cathode and anode composites.

Regarding the third type of compounds containing lead and tin which are suitable to use at room temperature, The ionic conductivity of PbSnF_4 and BaSnF_4 is in the order of 1×10^{-3} and $1 \times 10^{-4} \text{ S cm}^{-1}$ respectively, at 298 K [59]. Fujisaki et al. [60] prepared $\gamma\text{-PbSnF}_4$ by mixing SnF_2 and $\alpha\text{-PbF}_2$ at room temperature and heated to 473 K to obtain $\beta\text{-PbSnF}_4$. XRD analysis shows that the whole phase transformation process is irreversible. The phase transformation of $\gamma\text{-PbSnF}_4 \rightarrow \beta\text{-PbSnF}_4$ increases the ionic conductivity by an order of magnitude. Neutron diffraction shows that in $\gamma\text{-PbSnF}_4$, F^- mainly exists in the conventional site of $\text{F}^\gamma(1)$ and the interstitial site of $\text{F}^\gamma(2)$, with a ratio of 5:3. The F^- of $\beta\text{-PbSnF}_4$ mainly existed in the regular sites of $\text{F}^\beta(1)$ and $\text{F}^\beta(2)$, and the interstitial sites of $\text{F}^\gamma(2)\text{F}^\beta(3)$, with the ratio of 5:4:7. The increase of the concentration of

F^- in the interstitial parts makes the transmission of F^- in single Sn and Pb layers along the $-F^\beta(1) - F^\beta(3) - F^\beta(3) - F^\beta(1) -$ path more efficient, which fully explains the reason why the ionic conductivity increases after the phase transition. In 2015, Florian et al.[61] employed mechanosynthesis through high-energy ball milling as well as annealing (573 K for 2 h in a dry, oxygen-free protective atmosphere) to modify the ionic transport characteristics of tetragonal $BaSnF_4$, which possesses a layer-structured configuration. The cubic phase of $BaSnF_4$ can transform completely to the tetragonal phase after annealing and the layered form shows a room temperature conductivity of $7 \times 10^{-4} \text{ S cm}^{-1}$. The annealing process causes a noticeable reduction in the width of the X-ray diffraction (XRD) peaks, primarily because of the enlargement of grain size. Typically, specimen annealing at a high temperature can not only elevate the defect count but also facilitate grain growth, consequently enhancing ionic conductivity[62]. In view of the harm of Pb to the environment, Liu et al.[63] prepared $BaSnF_4$ by ball milling and doped with neodymium (Nd) to obtain $Ba_{1-x}Nd_x SnF_{4+x}$, so as to further improve the ionic conductivity. When $x = 0.02$, the ionic conductivity of the product at room temperature is as high as $5.8 \times 10^{-4} \text{ S cm}^{-1}$, which is more than 3 times that before doping. The high ionic conductivity can be attributed to Nd doping increasing the number of point defects in $BaSnF_4$, which is beneficial to the transmission of F^- . For both $BaSnF_4$ and $PbSnF_4$, oxidation and reduction processes involve a shift in the valence state of Sn, resulting in the formation of high-valent Sn and elemental Sn as products, respectively. Importantly, the electrochemical potentials for these reactions exhibit minimal differences, resulting in narrow electrochemical stability windows (ESWs) of 0.45 V and 0.53 V for $BaSnF_4$, and $PbSnF_4$, respectively as shown in Fig.2.22. Thus, $BaSnF_4$, and $PbSnF_4$, possess limited stability, restricting them to support relatively low cell voltages, typically not exceeding 0.5 V[52].

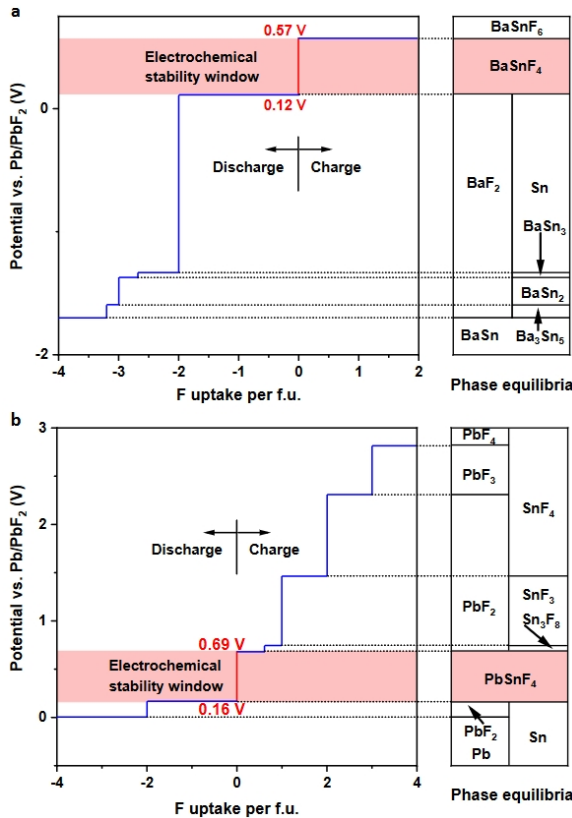


Figure 2.22: Calculated thermodynamic equilibrium voltage profiles and the phase equilibria for BaSnF_4 (a) and PbSnF_4 (b).[52]

Recently in 2021, Wang et al.[52] studied $\text{CsPb}_{1-x}\text{K}_x\text{F}_{3-x}$ with $x = 0, 0.05, 0.10, 0.15,$ and 0.2 (abbreviated as PK00, PK05, PK10, PK15, and PK20, respectively). The materials have a ABX_3 (A site is Cs^- , X site is F^- , and B-site simultaneously accommodates Pb^{2+} and K^+ .) perovskite structure with the $\text{Pm}\bar{3}\text{m}$ space group. They found that the room-temperature ionic conductivity increases first and then decreases with the increase of x while reaching the maximum value when $x = 0.1$, that is, the conductivity of PK10 is $1.23 \times 10^{-3} \text{ S cm}^{-1}$. On the contrary, the activation energy is first decreased and then increased. The reason for this is that aliovalent doping of K into CsPbF_3 introduces vacancies which improves F-ion transport. Furthermore, K-doping reduces the unit cell volume, thereby limiting the available space for F-ion migration. Initially, the first factor is dominant, but as the concentration of potassium increases, the latter factor becomes predominant, obstructing the transport of F-ions. Also, PK10 displays a low electronic conductivity, measuring $1.6 \times 10^{-7} \text{ S cm}^{-1}$. Unlike BaSnF_4 and PbSnF_4 , PK10 has a very wide ESW calculated as 1.8 V and its electrochemical redox reaction happens through the valence change of Pb. High-valent Pb is produced at 1.7 V versus Pb/PbF_2 in the oxidation process while the elemental Pb is produced at -0.1 V versus Pb/PbF_2 in the

reduction process. The LSV curves shown in Fig.2.23 provide clear evidence of oxidation commencing at 1.92 V and reduction initiating at 0.11 V. This difference of 1.81 V corresponds to the calculated ESW width of 1.8 V. With these favorable characteristics co-existing in the PK10, it will have great potential in the application of fluoride ion solid-state batteries at room temperature.

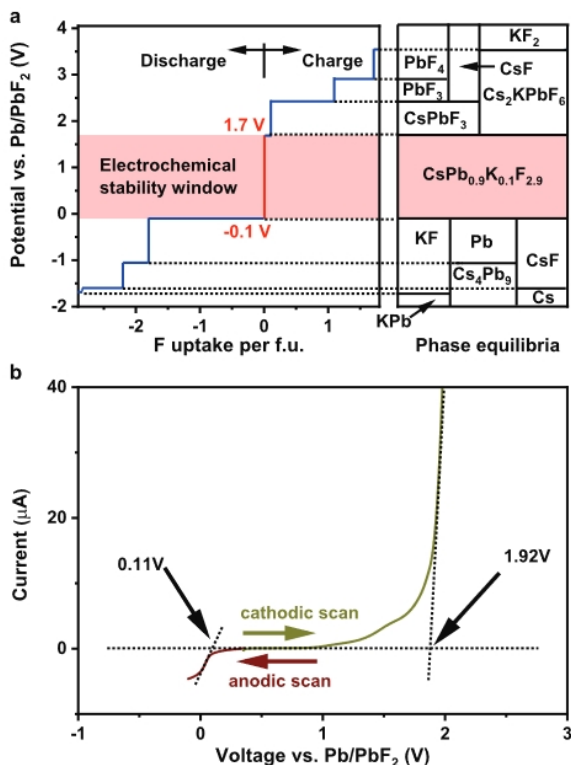


Figure 2.23: (a) Calculated thermodynamic equilibrium voltage profiles and the phase equilibria for PK10. (b) LSV curves of the PK10-MWCNTs/PK10/Pb-PbF₂-MWCNTs cell at 0.1 mV s⁻¹. [52]

Currently, the most common method for preparing solid electrolytes (SEs) is ball milling. The high-energy impacts generated during the ball milling process can grind the material grain size down to the nanoscale and introduce crystal defects. Higher rotational speeds result in greater impact energy on the material, leading to reduced crystal size and even structural damage, thereby generating more defects, including point defects and grain boundaries. The effect of grain boundaries on the fluoride ion conductivity differs between fluorite-type and tysonite-type fluorides. In fluorite-type fluorides, the transport of F⁻ ions primarily occurs along the grain boundaries, while grain boundaries hinder F⁻ conduction in tysonite-type fluorides. The reasonable rotational speed during ball milling is crucial for preparing SEs with high ionic conductivity. The high rotational speed during ball milling ensures thorough mixing of the starting materials, thereby promoting improved ionic conductivity. However, ball milling introduces some

impurities inevitably due to the sustained reaction under high rotational speeds for several hours. The degree of sample contamination during ball milling depends on factors such as milling time, rotational speed, atmosphere, and differences in hardness between the material and milling media.[55, 56]

Although ASSBs offer numerous advantages, they encounter several barriers on their path from the research laboratory to commercial production. These challenges include: (1)SSE Chemistry: As of now, no single Solid-State Electrolyte (SSE) possesses the required combination of properties for commercialization, such as high ionic conductivity, ease of processing, and broad electrochemical stability, among others. (2)Characterization Complexities: Due to their concealed and heterogeneous interfaces, as well as their vulnerability to electron beam damage, ASSBs prove challenging to characterize. (3)Scalability Issues: Despite recent advancements, issues related to air sensitivity and the insufficient mechanical properties of SSEs still hinder the implementation of roll-to-roll processes for scalable ASSBs production. (4)Sustainability Concerns: Currently, there are no established recycling models for ASSBs. Creating a sustainable ASSB model would necessitate strategies for recycling at the cell level that extend beyond mere electrode recovery.[64]

2.4. OBJECTIVE

In this project, transition metal oxides Cu_2O , FeO , and Mn_2O_3 are selected and tested as the cathode electrode material for solid-state fluoride ion batteries. The expectation is that during the electrochemical reaction, these metal oxide materials will undergo fluorination to form metal oxyfluorides. And this will lay the groundwork for research on oxyfluorides in solid-state fluoride ion batteries. The aim is to investigate the factors influencing the electrochemical performance of these solid-state fluoride ion battery systems and the underlying mechanisms. The solid electrolyte $\text{CsPb}_{0.9}\text{K}_{0.1}\text{F}_{2.9}$, denoted as PK10, is utilized, along with the anode Pb/PbF_2 composite. During experimentation, it is crucial to isolate the effects of the PK10 electrolyte and Pb/PbF_2 composites on these battery systems. Therefore, the present work targets the following questions:

1. Is the Pb/PbF_2 anode composite a proper reference/counter electrode when combined with PK10 solid electrolyte?
2. Is the combination of Cu_2O , FeO and Mn_2O_3 active cathode materials with PK10 solid electrolyte suitable for testing their electrochemical performance?
3. What is the compatibility between the electrochemical stability window (ESW) of PK10 and the fluorination reaction expected in Cu_2O , FeO and Mn_2O_3 full cells?

3

MATERIAL PREPARATION AND TESTING

3.1. SUBSTANCES AND EQUIPMENT

Substances and equipment used in this project are as shown in Table.3.1 and Table.3.2.

Substance	Manufacturer
Tin(II) fluoride, 99%	Merck Sigma
Lead(II) fluoride powder, $\geq 99\%$	Alorich
Potassium fluoride, 99%	Sigma-Aldrich
Cesium fluoride, 99%	VWR (Avantor) International BV
Lead powder, 99%	Alfa Aesar
Carbon nanotubes (CNTs), 98%	Merck Sigma
Silver powder	Merck Sigma
Copper(I) iodide, 98%	Merck Sigma
Iron(II) oxide, 99.9%	Alorich
Manganese(III) oxide, 99.9%	Alorich

Table 3.1: Substances. Note: All materials were dried overnight and stored in a MBRAUN Unilab glovebox filled with 1 atm (Linde) argon before use.

Equipment	Model, Manufacturer
X-ray diffractometer (XRD)	NLE1532C, PANalytical
Autolab AUT86298 - (EIS 10 MHz)	PGSTAT12, Metrohm
Autolab AUT71078 - (EIS 1 MHz)	PGSTAT302N, Metrohm
Planetary ball-mill with two jars - Solid State	P7, FRITSCHE
Ball mill jars (ZrO ₂)	FRITSCHE
Glovebox - Solid State	Unilab, MBRAUN
Maccor	SERIES 4000, Maccor
LANHE	G340A, LANHE
Vacuum drying oven	Row 9, Column 2
Oven (muffle) - Combustion / Synthesis (left oven)	L5/12/S27, Nabertherm
Memmert UF30+ Chamber (for EIS)	UF30+, MEMMERT
Memmert UF30 Chamber	UF30, MEMMERT

Table 3.2: Equipment.

3.2. EXPERIMENTAL SYNTHESIS

The synthesis of precursors and composites took place within a high-purity argon-filled glovebox (Unilab, MBRAUN) except for the ball-milling process.

3.2.1. BALL MILLING

Unlike traditional liquid batteries, solid-state batteries involve solid-solid contacts at the interfaces. The limited number of active sites on these solid interfaces significantly restricts ion transport, resulting in substantial interfacial impedance. Consequently, establishing a well-constructed interface contact is an effective approach to enhancing the electrochemical performance of all-solid-state batteries.[65]

To address this challenge, the application of high-energy ball milling has proven to be an exceptional method. This technique facilitates the creation of finely milled materials, which can potentially lead to improved solid-solid contact at the interface. By refining the interface, high-energy ball milling can effectively reduce the interfacial impedance and thereby enhance the overall performance of solid-state batteries [66]. The underlying principle of high-energy mechanical ball milling is similar to that of chemical synthesis; it involves the conversion of mechanical energy to facilitate chemical reactions, thereby inducing alterations in the material's structural organization and properties, a process commonly referred to as mechanochemistry. In the realm of high-energy ball milling, a mill that can attain the outcomes characteristic of this method is termed a high-energy ball mill. An example of such a mill is the planetary ball mill [67]. In a planetary high-energy ball mill, several milling jars are mounted on a rotating disc, and each jar not only orbits the disc but also spins on its own axis at a high speed. The grinding balls within these jars, subjected to inertial forces, exert substantial high-frequency impacts and friction on the materials, effectuating rapid and fine milling. Fig.3.1 is the schematic plot for the high energy ball milling processing.

The selection of milling conditions in the operation of a ball mill is critical and significantly affects the outcome of the final product[69]. These conditions include the grind-

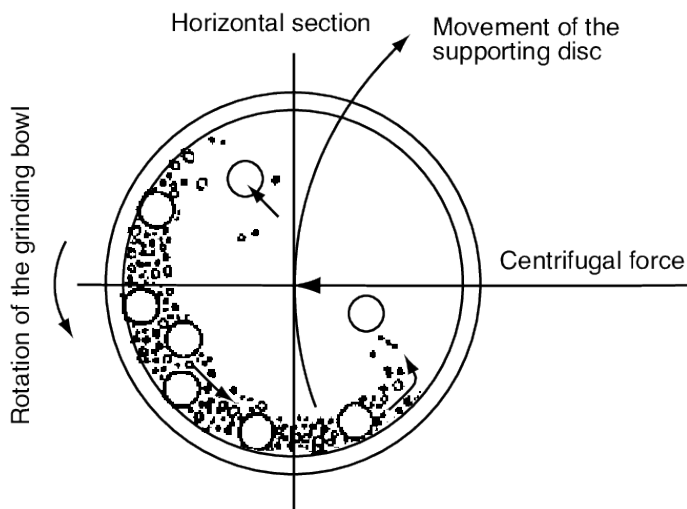


Figure 3.1: The schematic plot for the ball milling. [68]

ing time and the rotational speed of the mill. Insufficient grinding time may result in an inadequately ground product. On the other hand, Extended milling time in high-energy ball milling can bridge the miscibility gap and produce solid solutions that are otherwise difficult to synthesize. In crystalline materials, this process also serves to reduce grain size. However, beyond a certain milling duration, particles become exceedingly small and begin to agglomerate. This aggregation can have adverse effects on some materials. While the reduced particle size can enhance properties such as reactivity or sinterability, the agglomeration of these fine particles can detract from the material's overall performance by impacting properties like density, strength, or conductivity. Therefore, it is crucial to optimize milling time to balance the benefits of reduced particle size with the potential drawbacks of particle aggregation. The rotational speed of the mill plays a crucial role in the efficiency of the milling process. If the speed is excessively high, it can lead to the wear and potential breakage of the milling tools, resulting in contamination from tool debris. On the other hand, if the rotational speed is too low, the kinetic energy imparted by the balls onto the material may be insufficient. This lack of energy can lead to an inadequate impact force, failing to meet the energy requirements necessary for inducing solid-state reactions or the desired material transformations. Therefore, it is essential to carefully optimize the rotational speed to balance the need for effective milling without compromising the integrity of the milling tools and the purity of the final product. [70]

3.2.2. SYNTHESIS OF PRECURSORS

$\text{CsPb}_{0.9}\text{K}_{0.1}\text{F}_{2.9}$: $\text{CsPb}_{0.9}\text{K}_{0.1}\text{F}_{2.9}$ was synthesized through ball milling methods using CsF (VWR(Avantor), 99%), KF (Sigma-Aldrich, 99%), and PbF_2 (Alorich, $\geq 99\%$) as initial constituents. Initially, stoichiometric quantities of these materials were homogeneously mixed in an agate mortar. Subsequently, the mixture underwent ball milling using ZrO_2

balls (10 mm diameter) and ZrO_2 jars (45 ml) within a planetary mill (Pulverisette 7 premium line, FRITSCH). The milling process persisted for 8 hours at 500 rpm with 10 minutes pause for each 10 minutes milling under an Ar atmosphere (48 cycles), maintaining a ball-to-powder ratio of 20:1. The specific quantities of each substance used in each batch are detailed in the appendix.

3.2.3. ELECTRODE COMPOSITES

Pb/PbF₂ anode composite: Pb/PbF₂ composites are used as anode materials. All batches of Pb/PbF₂ composites are synthesized by mixing Pb, PbF₂, PK10 and CNTs in a weight ratio of 2:2:5:1 with mortar and pestle, except for the first batch named anode-1. Firstly, add lead (Pb), followed by PbF₂, then PK10, and finally, CNTs into the mixture. Ensure to grind for 2 minutes between each addition.

The synthesis process of anode-1 composite involves an additional step of ball milling compared to this. The ball milling using ZrO_2 balls (10 mm diameter) and ZrO_2 jars (45 ml) within a planetary mill (Pulverisette 7 premium line, FRITSCH). The milling process persisted for 13 hours at 100 rpm with a 10-minute pause for every 10 minutes milling under an Ar atmosphere (78 cycles), maintaining a ball-to-powder ratio of 24:1.

PK10-CNTs composite: PK10-CNTs composites serve as the working electrode in the Linear Sweep Voltammetry (LSV) measurement to evaluate the Electrochemical Stability Window (ESW) of the PK10 electrolyte. Mix PK10 and CNTs in a weight ratio of 9:1 with mortar and pestle.

Ag cathode composite: Mix Ag powder, PK10 and CNTs in a weight ratio of 4:5:1 with mortar and pestle. The composite is named Ag-1.

Cu₂O, FeO and Mn₂O₃ cathode composites: These composites are all formed by grinding and mixing active materials, PK10 and CNTs in a ratio of 3:6:1 using a mortar and pestle. The composites are named Cu₂O-1, FeO-1, and Mn₂O₃-1, respectively.

The actual masses of the precursors used in the synthesis of each material are included in the appendix.

3.3. BATTERY ASSEMBLY

The battery assembly process took place within a high-purity argon-filled glovebox (Unilab, MBRAUN). The solid-state battery device comprises a single PEEK cylindrical sleeve featuring a hole with a radius of 10 mm, two stainless steel current collectors, two sealing rubber rings and three metal bolts with gaskets as seen in Fig.3.2.



Figure 3.2: Device for solid-state battery.

The actual amounts of electrodes and electrolytes used for each battery are provided in the appendix.

3.3.1. EIS DEVICE

To make a solid-state battery for the EIS measurement, 200mg electrolytes were used. Add the electrolyte powder into the cylindrical sleeve and even it out by gently shaking the device on the desk. Apply a pressure of 50 bar for 5 minutes to compact the powder into a pellet, initially without incorporating the two sealing rubber rings. Subsequently, add the metal bolts and sealing rings, applying a pressure of 50 bar for an additional 5 minutes. Secure the bolts tightly. The process is as shown in the Fig.3.3. It's important to note that excessive pressure or misalignment of the collector can both potentially lead to a short circuit. During compression, avoid inserting the sealing rings as this may reduce the pressure applied to the powder.

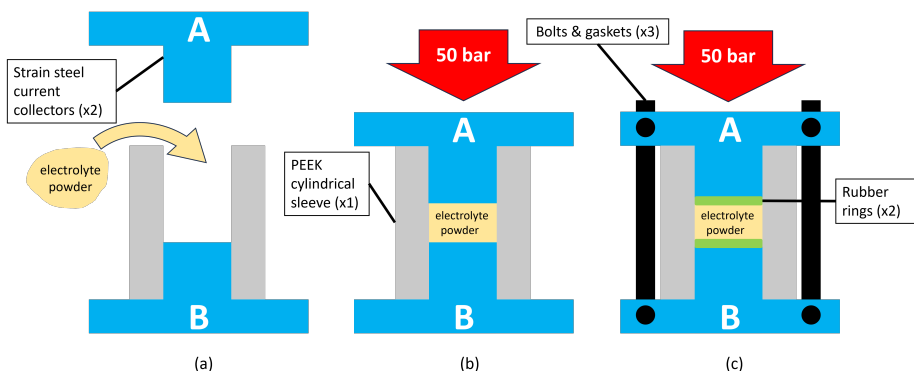


Figure 3.3: Illustration of the cell assembly for EIS measurement.

3.3.2. LSV DEVICE

In the linear sweep voltammetry measurement, PK10-CNTs composites serve as the working electrode, while Pb/PbF₂ composites function as the reference electrode due to the stable potential exhibited by the Pb/PbF₂ electrode. 200mg PK10 material, 46mg Pb/PbF₂ composites and 100mg PK10-CNTS composites are used. First add the electrolyte powder into the cylindrical sleeve and even it out by gently shaking the device on the desk. Apply a pressure of 50 bar for 5 minutes to compact the powder into a pellet. Then, apply Pb/PbF₂ composites on the bottom side (B side) and compress them at 50 bar pressure for 5 minutes. Then, place PK10-CNTS composites on the upper side (A side) and pressurize them at 50 bar for 5 minutes. Afterward, introduce the metal bolts and sealing rings, subjecting the assembly to an additional 5 minutes of 50 bar pressure. Finally, ensure the bolts are securely tightened.

3.3.3. FULL CELL DEVICE

To assemble a full cell, determining the necessary amount of active materials for each electrode is crucial. Therefore, calculating the specific capacity of the materials is essential.

To calculate the specific capacity of a certain material, the following equation is used:

$$Q = \frac{n \cdot F}{3.6 \cdot M} \quad (3.1)$$

Where Q represents the theoretical specific capacity in mAh/g, n denotes the number of electrons transferred, F signifies the Faraday constant (96,485.3321 sA/mol or C/mol), and M stands for the molar mass of the material in g/mol. The values of different materials are displayed in the Table.3.3.

The theoretical specific capacity of the corresponding composites is determined by multiplying the theoretical specific capacity of the material by its proportion within the composites. For instance, the theoretical specific capacity of Cu₂O is 373.97 mAh/g. Considering Cu₂O constitutes 30% of the Cu₂O composites, the theoretical specific capacity of the Cu₂O composites would be 0.3 multiplied by 373.97 mAh/g, which is 112.19 mAh/g. The theoretical specific capacities of different composites are displayed in the Table.3.3.

Electrochemical reaction	Theoretical specific capacity (mAh/g)	Theoretical specific capacity for composites (mAh/g)
Pb → PbF ₂	258.3	51.66
PbF ₂ → Pb	218.26	43.56
Ag → AgF	248.04	99.22
Cu ₂ O → Cu ₂ OF ₂	373.97	112.19
FeO → FeOF	372.42	111.73
Mn ₂ O ₃ Mn(III) → Mn(IV)	338.95	101.69

Table 3.3: Overview of the theoretical specific capacities of different materials and corresponding composites.

For the Cu₂O full cell, in order to create a full cell with a capacity of 1.5 mAh, a mere 0.0134 grams of Cu₂O composite would be required to serve as the cathode material.

Because this study focuses on the cathode electrode materials, the capacity of the anode electrodes should always be slightly greater than that of the cathode electrode materials, ensuring that the reaction occurs as fully as possible.

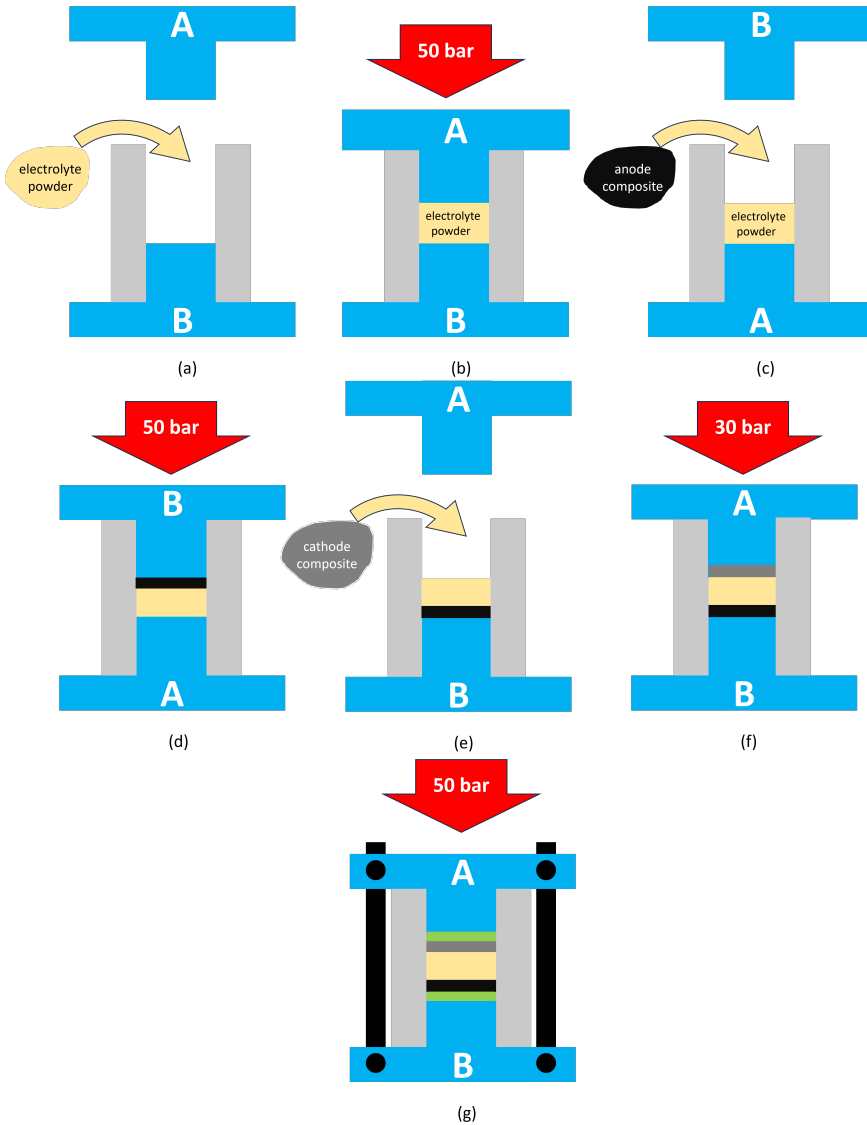


Figure 3.4: Illustration of full cell device assembly.

The steps for assembling the full cell batteries are identical to the LSV device setup, except for securing the cathode electrode on the upper side (A side) and the anode electrode on the bottom side (B side) for recording purposes. Additionally, due to the limited

quantity of positive electrode material used, a lower pressure of 30 bar is applied for compression, also to prevent any short circuits. Begin by pouring the electrolyte powder into the cylindrical sleeve, gently leveling it by shaking the device on the desk. Apply 50 bar pressure for 5 minutes to compact the powder into a pellet. Proceed by placing the Pb/PbF₂ composites on the bottom side (B side) and compressing them at 50 bar pressure for 5 minutes. Next, position the cathode composites on the upper side (A side) and apply 30 bar pressure for 5 minutes. Then, introduce the metal bolts and sealing rings, subjecting the assembly to an additional 5 minutes of 50 bar pressure. Finally, ensure the bolts are tightly secured. The process is illustrated in Fig.3.4.

3.4. X-RAY DIFFRACTION (XRD)

X-ray diffraction (XRD) is a powerful experimental method to characterize the atomic and molecular structure of a crystal. When X-rays enter the crystal, diffraction will occur in the crystal structure. By analyzing the intensity and angle information of the diffraction, the structural parameters of the crystal type can be known.[71]

3.4.1. X-RAYS SOURCE AND BLAGG'S LAW

X-rays are generated within an X-ray tube. This process commences with a high-voltage power source, which accelerates electrons emitted from a heated filament towards a metal target, typically composed of Cu, although Cr or Fe can also be utilized. As the electron beam strikes the metal target, the electrons in the K shell of Cu absorb energy, leading to ionization and creating a vacancy in the 1s orbital. Electrons from outer orbitals (such as the 2p or 3p orbital) promptly fill the vacancy in the 1s orbital, releasing energy in the form of X-rays. When electrons from the same outer orbital transition to the 1s orbital, they release energy of the same value, resulting in X-rays of the same wavelength. These X-rays, originating from different electrons within the X-ray beam, are then used for detection. The schematic representation of X-ray emission is depicted in Fig.3.5

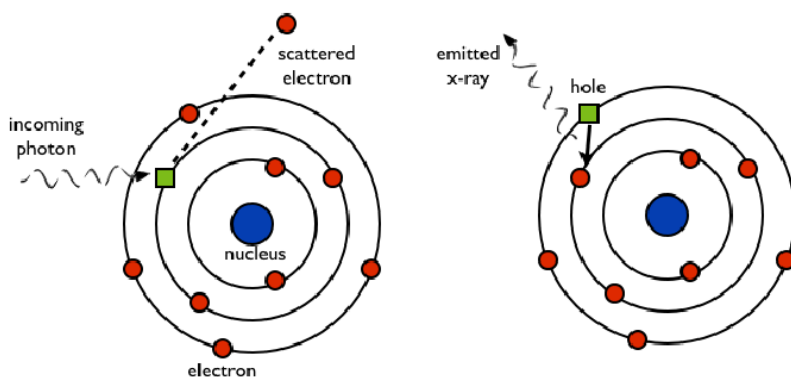
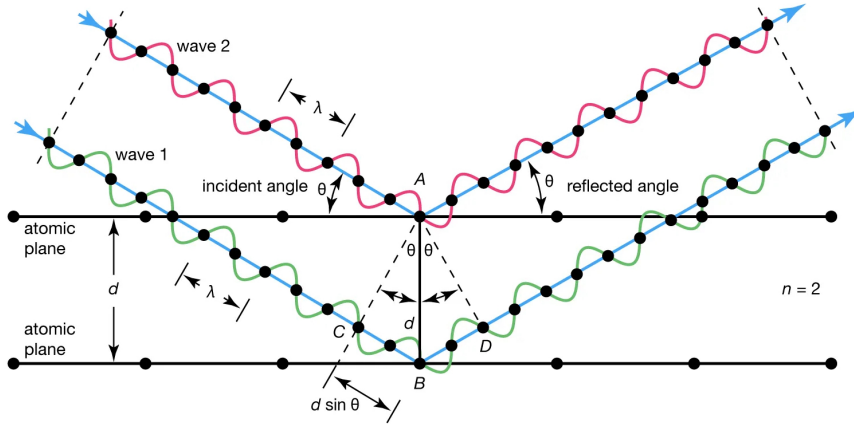


Figure 3.5: The schematic plot of X-ray emission. [72]

Diffraction occurs when X-rays are incident on a target crystal. As shown in Fig.3.6, two X-ray beams are reflected between two adjacent planes with an incident angle θ and a plane distance d . The second X-ray beam travels an additional optical distance ($2d \sin\theta$) compared to the first beam. When the optical path difference is an integer multiple of the wavelength, interference occurs between the two X-ray beams, enhancing the amplitude of the X-ray. This phenomenon is described by *Bragg's law* (Eq.3.2). Given that the wavelength is known, the interplanar spacing can be calculated by measuring the incident angle of X-ray diffraction, allowing for the analysis of the crystal structure.



© Encyclopædia Britannica, Inc.

Figure 3.6: The schematic plot of the X-rays diffraction from two atomic planes [73]

$$n\lambda = 2d \sin\theta \quad (3.2)$$

3.4.2. REFINEMENT

XRD refinement, commonly referred to as X-ray diffraction (XRD) pattern refinement, is a sophisticated analytical technique used in material science and crystallography to determine the crystal structure of a material. This process involves the refinement of a theoretical model to match the experimental X-ray diffraction pattern of a crystalline sample. In this project, Rietveld refinement and Le-bail refinement are used.

RIETVELD REFINEMENT

The Rietveld method analyzes the entire diffraction pattern, where a polycrystalline diffraction spectrum can be seen as a series of equidistant $2\theta - y_o$ data columns. If the crystal structure is known, the theoretical intensity y_{ci} at each 2θ can be calculated using crystal structure parameters and peak shape parameters. This is compared with the measured intensity y_{oi} using the least squares method, adjusting various parameters to minimize the difference M , achieving full spectrum fitting.

The difference M_i is calculated as:

$$M = \sum_i w_i (y_{oi} - y_{ci})^2 \quad (3.3)$$

The theoretically calculated intensity can be computed through the integrated intensity and peak shape function. The theoretical calculated intensity y_{ci} at a point 2θ on the diffraction spectrum can be expressed as:

$$y_{ci} = G_{ihkl}I_{hkl} + y_{bi} \quad (3.4)$$

Where G_{ihkl} is the peak shape function, commonly used in X-ray diffraction are the Pseudo-Voigt and Pearson VII functions, essentially a combination of Gaussian and Lorentzian functions; I_{hkl} can be calculated through the crystal structure and atomic composition; y_{bi} is the background intensity.

The integrated intensity I_{hkl} is calculated as:

$$I_{hkl} = SM_{hkl}L_{hkl}|F_{hkl}|^2 \quad (3.5)$$

Where S is the scale factor or proportionality factor, M_{hkl} is the multiplicity factor, L_{hkl} is the Lorentz factor, and $|F_{hkl}|$ is the structure amplitude.

LE-BAIL REFINEMENT

Le Bail analysis is a technique used in powder X-ray diffraction analysis, particularly when the crystal structure of the material under study is unknown or too complex to model. Unlike the Rietveld refinement, which requires a structural model to refine against the observed diffraction data, Le Bail analysis focuses solely on determining the intensity of each Bragg peak in the diffraction pattern without assumptions about the crystal structure. The method involves fitting the observed diffraction pattern by adjusting parameters such as peak positions, intensities, and widths. The central formula in this process is:

$$I_{obs}(1) = \frac{\sum y_i(obs) \cdot y_i(1)}{y_i(calc)} \quad (3.6)$$

Here, $I_{obs}(1)$ represents the observed intensity of a specific Bragg peak, $y_i(obs)$ denotes the observed intensity at each data point in the diffraction pattern, $y_i(1)$ refers to a part of the calculated intensity at each data point corresponding to a specific Bragg peak, and $y_i(calc)$ is the total calculated intensity at each data point, incorporating contributions from all Bragg peaks. Le Bail analysis is particularly valuable in the initial stages of crystal structure determination or in cases where the material's structure is not yet solved, allowing for the quantification of individual Bragg peak intensities from the overall pattern.

3.4.3. EXPERIMENTAL PARAMETERS

The examination of the samples' crystal structure employed powder X-ray diffraction (XRD) utilizing Cu $K\alpha 1$ radiation ($\lambda = 1.54 \text{ \AA}$). To safeguard against air exposure, the powder samples were encapsulated with a Kapton film-covered XRD sample holder throughout the measurement process as seen in Fig. 3.7. To effectively characterize materials containing FeO, the utilization of a monochromator is essential to reduce background interference on the sample.

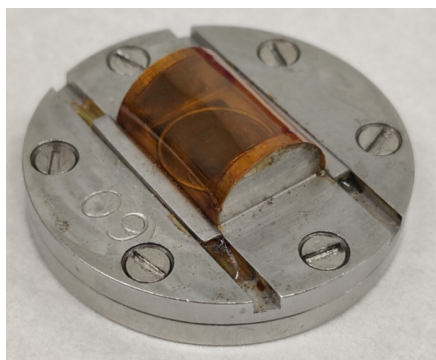


Figure 3.7: Kapton film-covered XRD sample holder. [72]

3.5. ELECTROCHEMICAL IMPEDANCE SPECTROSCOPY (EIS)

The fundamental principle of electrochemical impedance spectroscopy involves applying an alternating current (or voltage) signal in the form of a sinusoidal waveform to the electrode system. This perturbation generates a corresponding current (or voltage) response. Analyzing these signals enables the determination of the electrode's or solid electrolyte's impedance or admittance. So, Electrochemical Impedance Spectroscopy (EIS) technology involves determining the ratio of perturbation signal to response signal at different frequencies. This process yields the real part Z_{Re} and imaginary part Z_{Im} of impedance at various frequencies, as well as the magnitude $|Z|$ and phase angle ϕ . Subsequently, these quantities are plotted in various forms of curves to generate the EIS spectrum such as the Nyquist plot and Bode plot. The impedance is a complex number $Z(\omega)$, which can be expressed as the real part Z_{Re} and the imaginary part Z_{Im} , which forms a well-known equation:

$$Z(\omega) = Z_{Re} + iZ_{Im} \quad (3.7)$$

The resulting EIS spectrum is also divided into x and y axes by these two parts.

As for Experimental EIS data, it is interpreted using an equivalent electric circuit model. This model comprises electric and electrochemical components chosen to mimic the electrochemical system's reaction to the applied signal. Each element in the circuit represents a particular physicochemical process within the cell, contributing to a distinct impedance pattern.

It can be considered that there are several components in the system: Resistance of the cable; Resistance within the working electrode; Resistance at the interface between the working electrode and the electrolyte; Electrolyte resistance between the working electrode and the reference electrode; Capacitance induced by the double layer at the interface between the working electrode and the electrolyte. Since the cable resistance, resistance within the working electrode, and electrolyte resistance are all in series, based on physical principles, they can be regarded as a single resistance. Moreover, in relative terms, cable resistance and internal resistance of the working electrode are much lower than the electrolyte resistance. Therefore, they are generally referred to as the solution

resistance (R_{et}). The resistance at the interface and the capacitance induced by the double layer at the interface are considered to occur at the same location, hence assumed to be in parallel (R_{ct} and CPE2). From a physics perspective, a capacitor is an element composed of two extremely smooth metal plates. However, in electrochemistry, electrode surfaces are generally not very smooth, and in some applications, they may even be modified, resulting in non-smooth surfaces. To address this issue, the Constant Phase Element (CPE) was introduced as a replacement for the capacitor (C). However, if the charge transfer is affected by diffusion (mass transfer), this influence should be added as CPE1 here. Therefore, the overall system can be described as follows:

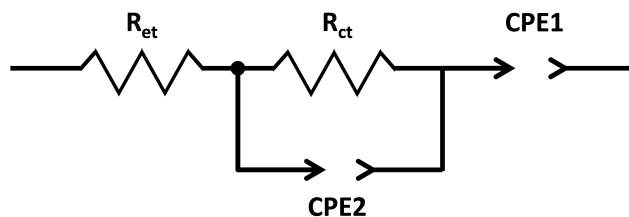


Figure 3.8: Equivalent circuit model with mixed kinetic and diffusion control.

At high frequencies, the R_{et} resistance predominates, so $Z = R_{et}$, and the phase angle is 0° . In the low-frequency range, the impedance of the double layer is high, and $Z = R_{et} + R_{ct}$, with phase angles all being 0° . At intermediate frequencies, the double layer capacitance influences the phase angle, and impedance measurements yield results between R_{et} and $(R_{et} + R_{ct})$. Thus, a 'semi-circle' part appears in the Nyquist plot as seen in Fig.3.9. Due to the influence of diffusion, the graph exhibits a linear state at a 45-degree angle to the horizontal axis. Overall, the EIS results in a typical "semicircle + tail" curve in the form of the Nyquist plot. From the perspective of frequency distribution, the dynamic control region belongs to the mid-to-high frequency range, while the diffusion region falls within the low-frequency range.

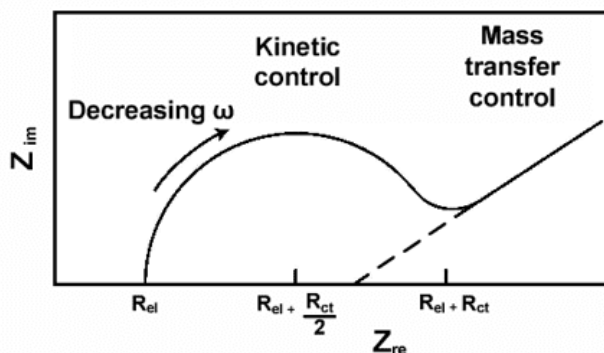


Figure 3.9: Qualitative Nyquist plot for a modified Randles circuit with mixed kinetic and diffusion control. [74]

And we can get the conductivity through the formula:

$$\sigma = \frac{L}{R \cdot A} \quad (3.8)$$

where R is the real part of the impedance also named the total impedance (resistance) in mS/cm, L is the thickness of the sample in cm, and A is the area of the sample in cm² (e.g. πr^2 for circular pellet and r is the radius of the pellet).

3.5.1. EXPERIMENTAL PARAMETERS

The Electrochemical impedance spectroscopy (EIS) analysis was performed utilizing an Autolab instrument (PGSTAT12, Metrohm) over a frequency range spanning from 0.1 Hz to 10 MHz, applying a driving potential amplitude of 100 mV.

3.6. LINEAR SWEEP VOLTAMMETRY (LSV)

When the electrode potential stays within a range where no reaction happens, there's no substance reduction or consumption, resulting in zero Faradaic current. This displays as a residual current curve (1–2 segments) in Fig.3.10. As the electrode potential surpasses the critical point for substance reaction, reductions occur, generating reduction current. Initially, due to substantial substance concentrations on the electrode surface, there's enough material available. As the potential shifts negatively, the reduction current gradually rises (e.g. 2–4 segments).

Continued consumption and the diffusion layer's growth lead to at potential 4, where substance concentration near the electrode hits zero, causing complete concentration polarization and the diffusion current hitting its limit. Further negative shifts (e.g. 4–6 segments) increase consumption, but thicker diffusion layers reduce material supply to the electrode, causing a depletion effect. The reduction current decreases, forming a peak-shaped voltammogram (as in Fig.3.10).

There's another kind of situation that after potential 4, the diffusion layer's thickness remains constant due to continuous convection constraint. Mass transfer near the electrode stays in a steady diffusion mode. Despite potential shifts consuming more material, the electrode's material supply remains constant. Reduction current magnitude depends solely on liquid-phase diffusion mass transfer, resulting in an "S"-shaped voltammogram (as in Fig.3.10).

In essence, when electron transfer rates are high, the electrode reaction often faces 'demand exceeds supply' scenarios, leading to sharper peak-shaped voltammograms. Conversely, lower electron transfer rates or faster liquid-phase mass transfer result in a stable current mode, often seen as flatter peak or "S"-shaped voltammograms. In this project, the LSV measurement is used to analyze the electrochemical stability window (ESW) of solid electrolytes.

3.6.1. EXPERIMENTAL PARAMETERS

The linear sweep voltammetry (LSV) assessments of PK10 were performed employing PK10-CNTs|PK10|Pb/PbF₂ cells, using a scan rate of 0.1 mV s⁻¹ with a step of 2 mV for both positive and negative sweeps. The positive sweep covered a voltage range from

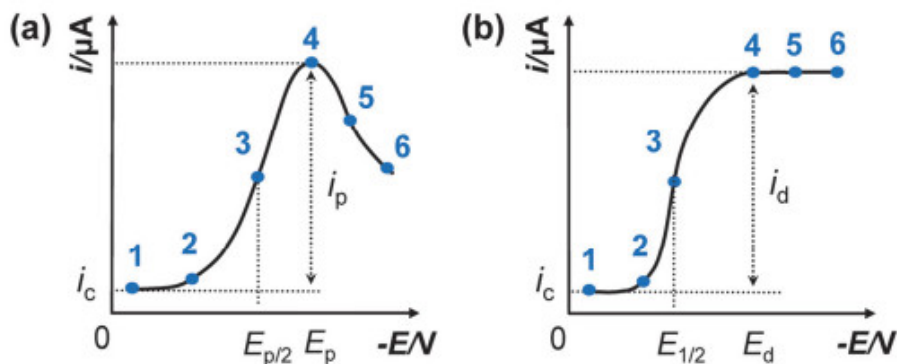


Figure 3.10: Schematic diagram of the formation process of linear sweep voltammetry during the reduction reaction. [75]

open circuit voltage to 3.3V vs. Ref, while the negative sweep spanned from open circuit voltage to -1V vs. Ref. The PK10-CNTs composite is used as the work electrode and the Pb/PbF₂ composite is used as the reference electrode.

3.7. CYLIC VOLTAMMETRY(CV)

Cyclic voltammetry (CV) is also a widely used electrochemical method that examines the redox reactions of molecules, offering insights into electron transfer-driven chemical reactions, including catalytic processes. The principle of cyclic voltammetry (CV) is similar to that of linear sweep voltammetry (LSV), but CV adds a reverse scan to the forward linear scan. In a typical CV process, during the cathodic scan, electroactive species at the electrode undergo reduction, resulting in a reduction peak. During the anodic scan, the reduced products are oxidized back on the electrode, creating an oxidation peak. Therefore, one cycle of CV completes one oxidation and reduction process.

From the voltammogram in Fig.3.11, it's evident that the voltammogram of a reversible electrode system appears sharp and symmetrical, whereas the curve for an irreversible system is broader, less symmetric, and asymmetrical. The transition from reversible to irreversible resembles a shift from a "peak" to an "S" shape.

From Fig.3.12, it can be seen that as the rate constants decrease, the curves shift toward more reductive potentials. This change can be explained by a slower establishment of surface equilibrium. Consequently, the peak separation becomes variable instead of fixed and is dependent on the scan rate. Likewise, the relationship between peak current and the square root of the scan rate no longer holds. Analyzing how the peak position changes concerning the scan rate variation offers a way to estimate the electron transfer rate constants.

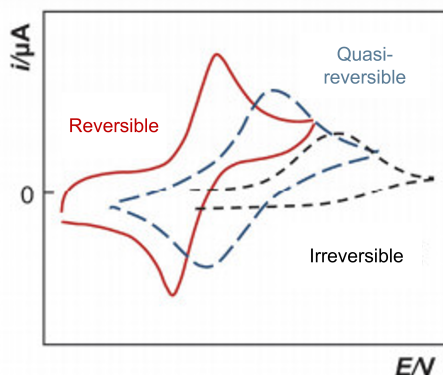


Figure 3.11: Reversible and irreversible CV diagram. [75]

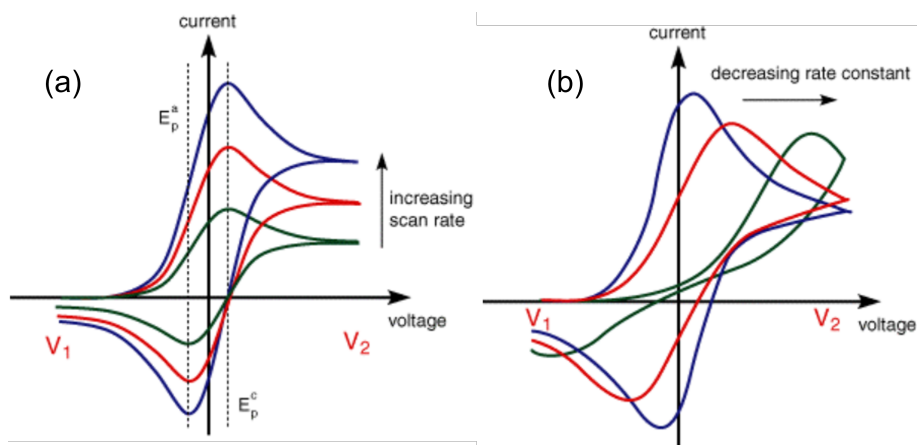


Figure 3.12: Variations in scan rate and rate constants influence the shapes of current-voltage (I-V) curves. [76]

3.7.1. EXPERIMENTAL PARAMETERS

Cyclic voltammetry (CV) was utilized for the Ag full cell, employing a voltage window ranging from 0.2 V to 1.8 V. The potential was scanned at a rate of 0.1 mV s^{-1} , and the testing comprised cycling for five rounds. Additionally, cyclic voltammetry (CV) was employed for the Cu_2O full cells operating at 60°C for five cycles, with a voltage window ranging from 0.2 V to 1.75 V. The potential was scanned at a rate of 0.05 mV s^{-1} .

3.8. GALVANOSTATIC CHARGE AND DISCHARGE (GCD)

The galvanostatic charge-discharge (GCD) method is the most commonly employed technique for battery testing. Under constant current conditions, the electrode under test is subjected to charging and discharging, and the variation of its potential over time is recorded to explore the function of potential with respect to time. Its fundamental prin-

principle involves subjecting the tested electrode to charge and discharge operations under constant current conditions while documenting the changes in potential over time. This investigation aids in studying the charge-discharge performance of the electrode and computing its actual specific capacity. Throughout the constant current charge-discharge experiments, the electrochemical response signal of the controlled current is monitored. The applied current serves as the controlling signal, while the potential represents the measured response signal, primarily studying the function of potential over time. The charge-discharge tests conducted on batteries allow for direct observation of the battery's charge-discharge capacity, Coulombic efficiency, and other changes throughout cycling. Post-data analysis enables assessment and evaluation of the battery's cycling performance, encompassing aspects such as cycle life, presence of capacity fade, and other critical indicators. The plateau on the charge-discharge curve corresponds to the redox reaction.

Given the impact of active material content and electrode dimensions on the test current, constant current charging is commonly represented in terms of current density, such as mA/g (current per unit mass of active material) or mA/cm² (current per unit electrode area). The magnitude of charge and discharge currents is often expressed in terms of C-rate. The C-rate is a measure indicating the rate capability of charge and discharge for a battery. It represents the constant current charge or discharge rate that a battery can sustain for 1 hour, calculated by dividing the nominal charge capacity of the battery by 1 hour. For instance, For a battery with a rated capacity of 100 Ah, a discharge of 20 A represents a discharge rate of $\frac{1}{5 \text{ hours}} = 0.2 \text{ C}$. Discharging the full capacity in 1 hour is termed as a 1C discharge; discharging it in 5 hours is termed as a 1/5 = 0.2 C discharge.

Battery rate capability testing involves subjecting the battery to constant current charge and discharge at various rates, characterizing and evaluating its performance under different charge and discharge rates. Commonly used charge and discharge rates include 0.02 C, 0.05 C, 0.1 C, C/3, 0.5 C, 1 C, 2 C, 3 C, 5 C, and 10 C.

When testing the cyclic performance of a battery, it is primarily necessary to determine the charge-discharge mode of the battery. This involves cyclically charging and discharging the battery until its capacity decreases to a specified value, often around 80% of the rated capacity. The evaluation includes tracking the number of charge-discharge cycles the battery undergoes or comparing the remaining capacity of the battery after a specific number of cycles. This characterization aims to represent the cyclic performance of the tested battery.

Through galvanostatic charge-discharge testing, the coulombic efficiency (CE) of the battery can also be determined. Coulombic efficiency, also known as discharge efficiency, typically refers to the ratio of the discharge capacity of a battery to its charge capacity during the same cyclic operation. It is represented as a percentage, calculated as the discharge capacity divided by the charge capacity as seen in Eq.3.9. The higher the Coulombic efficiency, the less capacity the battery loses in each charge/discharge cycle, resulting in a longer potential lifespan.

$$CE(\%) = \frac{\text{Discharge capacity}}{\text{Charge capacity}} \quad (3.9)$$

Galvanostatic charge-discharge tests can also yield information on the energy density and power density of batteries, which are important factors for assessing battery performance. The energy density of a battery refers to the electrical energy released per unit volume or mass of the battery, encompassing both mass energy density in terms of Wh/kg and volumetric energy density in terms of Wh/L. It is determined by the material properties. A higher energy density implies a greater amount of stored charge per unit mass or unit volume. From the perspective of the electrode's active material, specific energy density W denotes the amount of energy released per unit mass of the electrode material participating in the electrode reaction:

$$W(\text{Wh/kg}) = \frac{n \cdot F \cdot E^* \cdot 1000}{M} \quad (3.10)$$

where n represents the number of ions involved in the electrochemical reaction, F denotes Faraday's constant, E^* stands for the average operating voltage of the battery, and M signifies the total relative molecular weight of the cathode and anode electrode materials in the battery.

Power density P (W/kg or W/L) refers to the rate at which a battery, per unit weight, can output energy during discharge. Power density can be characterized by the following formula:

$$P(\text{W/kg}) = I(V - I \cdot R_{int}) \quad (3.11)$$

where I denotes the charging and discharging current of the battery, V signifies voltage, and R_{int} corresponds to the internal resistance of the battery. Lower internal resistance in a battery leads to higher power density. Yet, internal resistance primarily links to factors such as electrolyte ion conductivity, electrode material's ion and electron conductivity, charge transfer dynamics, battery storage mechanisms, and the interfacial resistance between electrodes and electrolytes.

The energy density and power density are not directly related. However, there exists a plot known as the Ragone plot also named the E-P plot that displays an energy–power correlation. In Ragone plots from literature, there are four elements: characteristic curves, enveloping bands, nominal points, and arbitrary shapes (Fig. 3.13)[77]. These elements can be freely combined within a single Ragone plot as well. Bringing together multiple Ragone characteristic curves to form enveloping characteristic bands illustrates the scope of energy and power values encompassed by an entire storage technology. Ragone plots may sometimes feature solely one operational point from a solitary storage instance, frequently the nominal point. To represent an entire technology, an arbitrary shape is used in the E-P plane, seen in Fig. 3.13, indicating the typical scale of E, P, or related specific quantities. These shapes, often squares, circles/ovals are chosen based on experience or manufacturer-provided data.

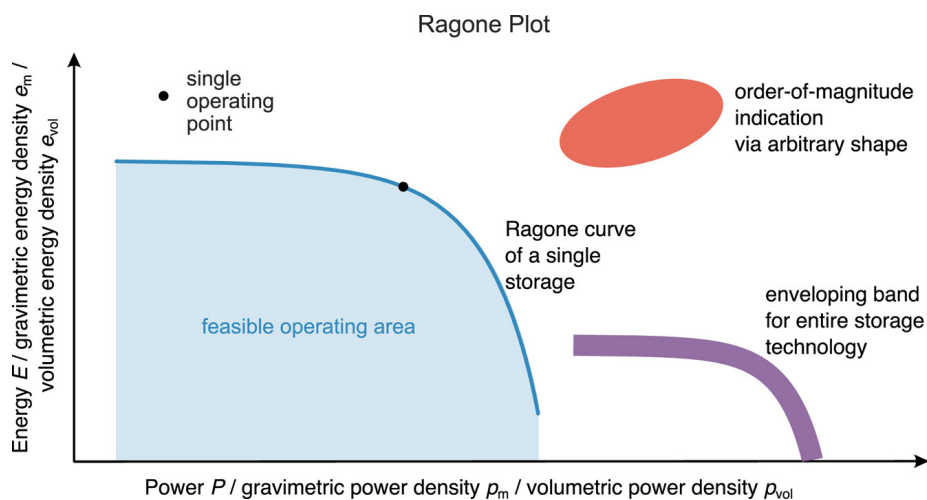


Figure 3.13: Illustration of common Ragone plot. [75]

3.8.1. EXPERIMENTAL PARAMETERS

Galvanostatic charge and discharge tests at room temperature were conducted using Maccor (SERIES 4000). For tests at 60 degrees Celsius, both charge and discharge procedures involved the use of a LANHE (G340A) and a constant temperature chamber (Memmert UF30 Chamber).

The symmetric cells, all employing tetrahedral PK10, were tested under constant current conditions of $50 \mu\text{A}$ (from SW-1 to s-50-3 as seen in Appendix) or $20 \mu\text{A}$ (from s-20-1 to s-20-6 as seen in Appendix).

The Ag full cell was tested under constant current density conditions of 5.2 mA/g , with a voltage limit window set between 0.2 V and 1.8 V .

The cells containing Cu_2O , FeO , Mn_2O_3 were tested under constant current density conditions of 7.5 mA/g , 17.9 mA/g and 6.8 mA/g , respectively. The voltage limit window was set between 0.2 V and 1.75 V for most cells, except for C-5-1 and C-35-1 (seen in Appendix), where the voltage limit window was adjusted to 0.4 V and 1.5 V .

4

RESULTS AND DISCUSSIONS

4.1. SOLID ELECTROLYTE SYNTHESIS - $CsPb_{0.9}K_{0.1}F_{2.9}$ (PK10)

$CsPb_{0.9}K_{0.1}F_{2.9}$, abbreviated as PK10 was used as electrolyte in this project. Three batches of PK10 were synthesized and named sequentially as PK10-1, PK10-3, and PK10-4.

The XRD patterns of the CsF, PbF_2 , and KF precursors were recorded to ascertain their phase purity, as shown in Fig.4.1, along with the indexed reflections for matched phases. Both CsF and KF exhibit a rocksalt structure, with a reported lattice constant of 6.00 Å for CsF and 5.34 Å for KF. The larger lattice constant for CsF is evident from the position of the (200) reflex at 29.75°, while for KF, it is apparent in the position of the (200) reflex at 33.58°. Both materials are confirmed to be phase pure within the detection limit of the technique. It can be observed that PbF_2 exists in two phases: cubic- PbF_2 with a space group of $F\bar{m}3m$ and orthorhombic- PbF_2 with a space group of Pnma. The proportion between orthorhombic and cubic phases is found to be 82% and 18%, respectively, for the PbF_2 -based phases. Apart from these two phases, no other impurities or side-phases are detected, confirming that all three precursors are suitable for further use in synthesis work.

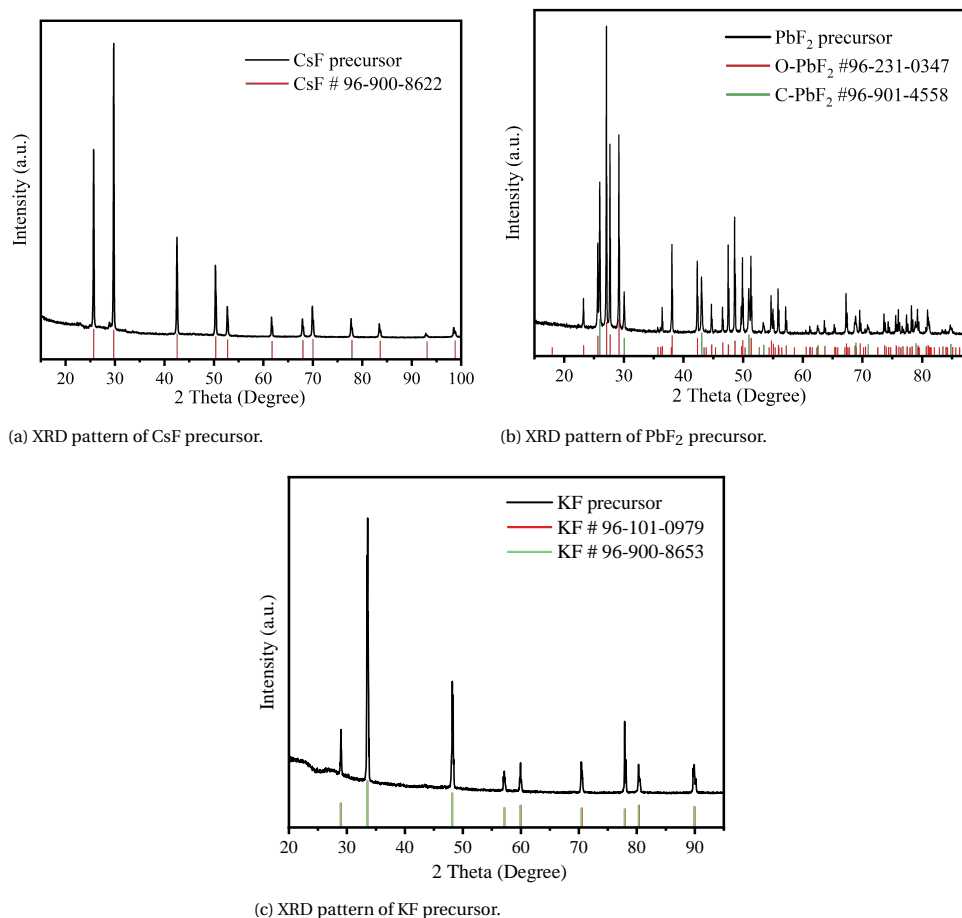


Figure 4.1: XRD pattern of precursors for PK10.

All of the synthesized materials, along with CsPbF₃, exhibit the cubic perovskite structure with $P\bar{m}3m$ symmetry. This consistency arises from the fact that only 10% of K replaces Pb, occupying Pb's site, and this doping is not sufficient to alter the space group type. The XRD patterns of various batches of PK10, both original and refined, are illustrated in Fig. 4.2. Since we know the structure of the phase CsPbF₃ at room temperature and its space group is $P\bar{m}3m$, we use it to perform the Le-Bail refinement to determine the lattice parameter of the synthesized PK10 materials. All three batches of PK10 exhibit the three strongest peaks at approximately 26.4°, 37.6°, and 46.5°, corresponding to the crystallographic planes (110), (200), and (211), respectively. The lattice parameters for three materials are 4.781(5) Å, 4.786(2) Å, and 4.785(7) Å, respectively, while the lattice parameter for the CsPbF₃ according to Wang et al. [52] is 4.79807(15) Å, which is larger than that of the synthesized materials. Although Pb²⁺ has a smaller radius of 1.19 Å compared to K⁺ with a radius of 1.38 Å, the introduction of K into CsPbF₃ results in a decreased lattice parameter. These all prove that the PK10 materials have been success-

fully synthesized.

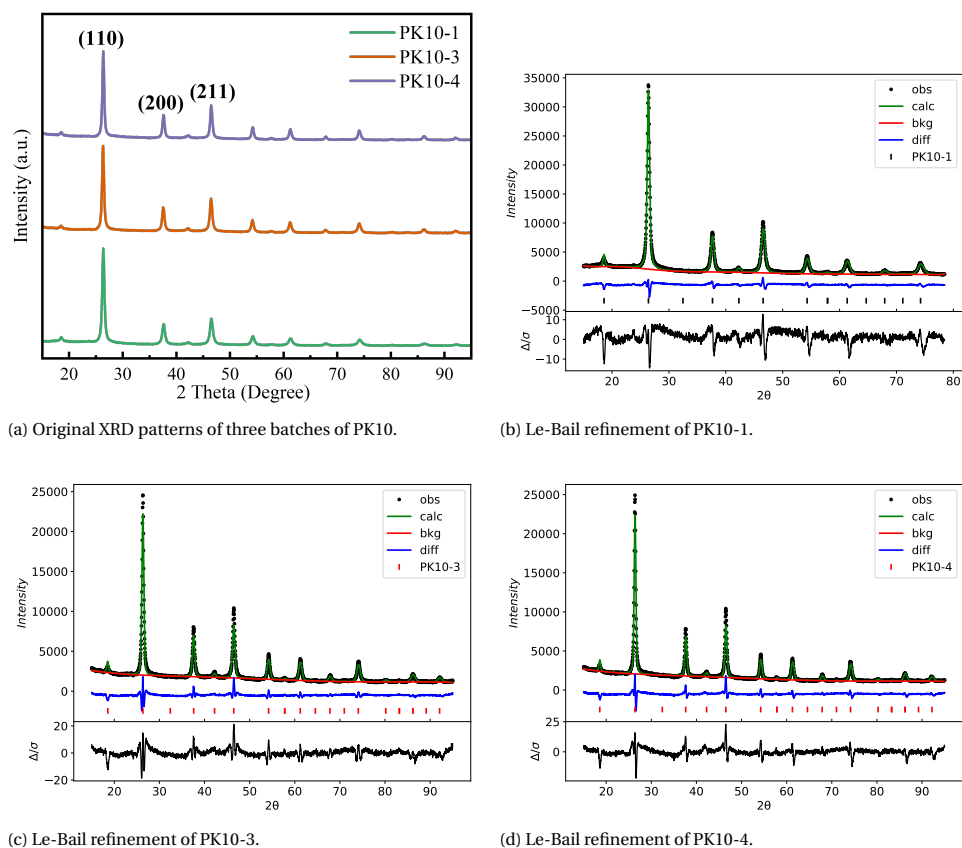


Figure 4.2: The XRD patterns for different batches of PK10, both in their original form and following Le-Bail refinement.

	Space group	a(Å)	Unit-cell volume (Å ³)
PK10-1	Pm-3m	4.781(5)	109.3(1)
PK10-3	Pm-3m	4.786(2)	109.6(4)
PK10-4	Pm-3m	4.785(7)	109.6(1)

Table 4.1: Le-Bail refinement results of the XRD pattern for PK10-1, PK10-3 and PK10-4.

EIS measurements were conducted to determine the ionic conductivity of the synthesized PK10 materials. The Nyquist plots for these measurements are depicted in Fig.4.3. In the qualitative aspects, a semicircle is observed at higher frequencies, indicating the presence of charge transfer processes, while a straight slope is evident at lower frequencies, suggesting diffusion-limited behavior.

Upon examining Table.4.2, it's evident that the ionic conductivities of all three materials are approximately in the order of 0.1 mS/cm at room temperature. Specifically, PK10-4 exhibits the highest ionic conductivity at 0.326 mS/cm, followed closely by PK10-3 with 0.324 mS/cm, and PK10-1 with 0.215 mS/cm.

As the temperature is raised to 60°C, the ionic conductivity increases significantly, reaching the order of 1 mS/cm. Notably, at this elevated temperature, the Nyquist plot shows the disappearance of the semicircular portion, leaving only a sloping line. This observation suggests that the diffusion process in the electrode becomes the rate-limiting step. In other words, while the charge exchange process occurs rapidly, the diffusion of charge carriers to the electrode surface becomes a slower process.

Comparing the qualitative aspects of the Nyquist plots, it's notable that the semicircle is largest for PK10-1, somewhat smaller but similar in width for PK10-3 and PK10-4, and absent for PK10-4 at the higher temperature. This observation suggests a higher real part of the impedance, and hence a lower conductivity for sample PK10-1 compared to the other two. Furthermore, it is remarkable that the two samples with matching impedance plots (PK10-3 and PK10-4) are also the two with the closest lattice parameters. This suggests a potential relationship between sample ionic conductivity and lattice parameter, possibly related to the actual amount of potassium incorporated as a dopant and its role in forming fluoride ion vacancies responsible for the ionic conductivity.

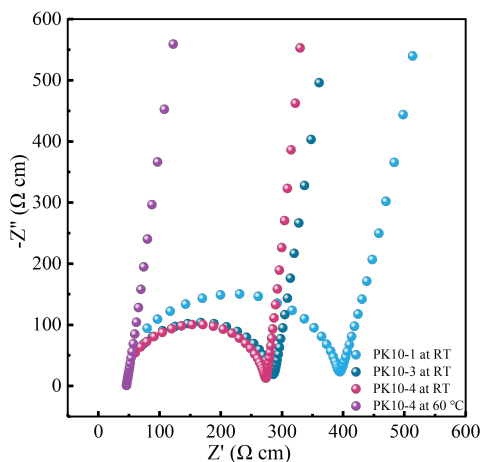


Figure 4.3: Nyquist plot of PK10-1, PK10-3 and PK10-4 at room temperature as well as PK10-4 at 60 °C.

	Impedance (Ω)	Pellet thickness (mm)	Conductivity σ (mS/cm)
PK10-1 at RT	312.4	0.527	0.215
PK10-3 at RT	200.7	0.511	0.324
PK10-4 at RT	192.1	0.491	0.326
PK10-4 at 60°C	46	0.447	1.238

Table 4.2: Calculated ionic conductivity of the electrolyte, presented in mS/cm per batch. * RT means room temperature.

4.2. Ag FULL CELL TESTING

Initially, the Ag full cell was tested to assess whether the fluoride ion battery, employing PK10 as the electrolyte and Pb/PbF₂ as the anode, functions as reported in Wang et al.'s study [52]. The Ag composite named Ag-1 was used as the cathode, and the second batch of Pb/PbF₂ anode named anode-2 was used here. A more detailed description and discussion of the anode composites can be found in section 4.4.

In the first step of the characterization for the Ag-based cell, the Ag metal powder precursor was characterized with XRD (Fig. 4.4a). Next, the Ag composite, named Ag-1, used as the cathode in the Ag-cell was also investigated. The pattern in Fig. 4.4b displays an XRD pattern that evidences the presence of both Ag metal and PK10 in the composite mixture. Furthermore, a preliminary Rietveld refinement of this pattern suggests a weight ratio of 41.5:58.5 between Ag and PK10-1. This ratio aligns seamlessly with the synthesized ratio of 4:5. However, an issue arises from the inability to determine with high certainty the position of the lighter atoms (F and O) relative to the Pb sub-lattice. Consequently, there is a corresponding uncertainty in simulating the scattering in the Rietveld procedure, and this uncertainty extends to the determination of phases by the bespoke procedure. Hence, phases based only on metal atoms (e.g. Ag) may respond differently than phases with lighter atoms (e.g. PbF₂), so that phase fraction obtained during Rietveld refinement is used only as a reference.

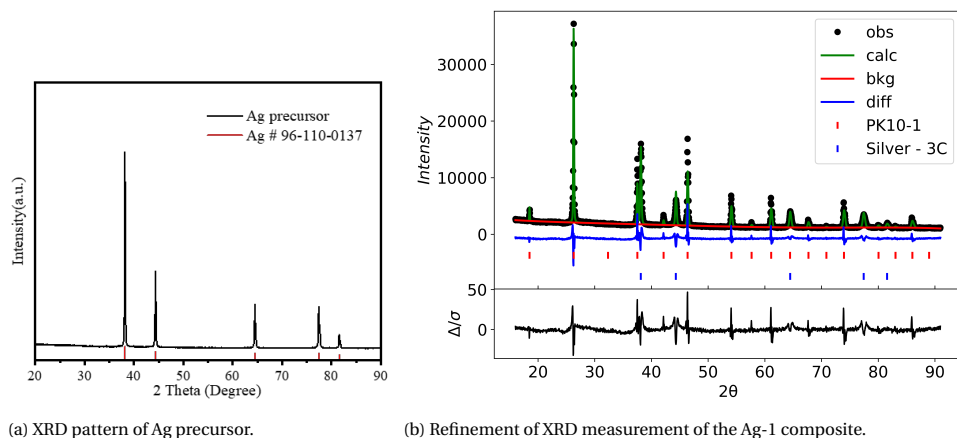


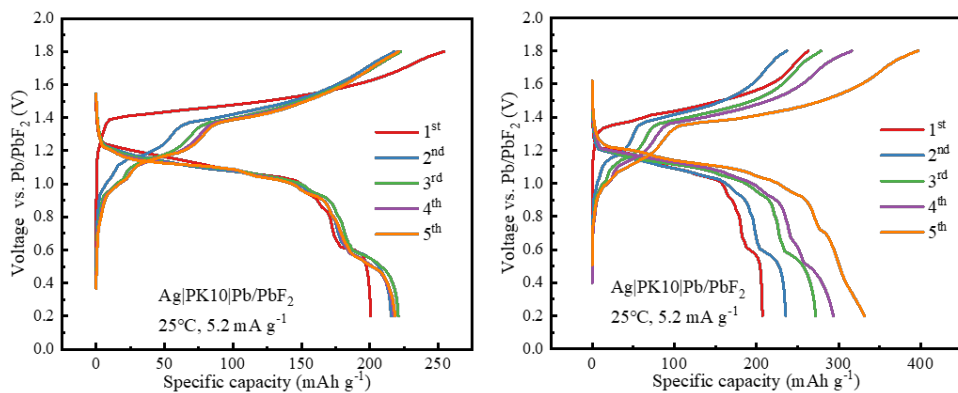
Figure 4.4: XRD pattern of the Ag precursor and refinement of the Ag-1 XRD pattern.

Following the structural characterization of the composites, full cells were assembled and the galvanostatic charge and discharge (GCD) and cyclic voltammetry (CV) measurements at room temperature were conducted here to test the electrochemical performance of the Ag full cell. The cells Ag-5-1 and Ag-5-2 were employed for GCD, while Ag-5-3 was used for CV, each running for a duration of 5 cycles. The nominal capacities of the cells are all the same, which is 1 mAh.

Fig. 4.5a depicts the GCD curve for cell Ag-5-1, with the first charge curve in red. This line first slopes from 9.93 mAh/g at 1.39 V and is characterized by a charged plateau at 1.5 V, from which a specific capacity of 254 mAh/g can be determined. It slightly surpasses the theoretical specific capacity of 248.04 mAh/g. This is related to the uncertainty associated with the specific capacity due to the weighing of the cathode materials. The uncertainty of the scale used to weigh the composite in the cell assembly is on the order of 0.1 mg, and when multiplied by 0.1 mg along with the theoretical specific capacity of Ag and experimental specific capacity 254 mAh/g, the uncertainty is calculated to be ± 6 mAh/g. Consequently, the experimental specific capacity of the Ag full cell aligns closely with the theoretical specific capacity. There is a noticeable decrease in specific charge capacity during the second cycle. The specific discharge capacity for the first cycle reaches 200.73 mAh/g which is satisfying.

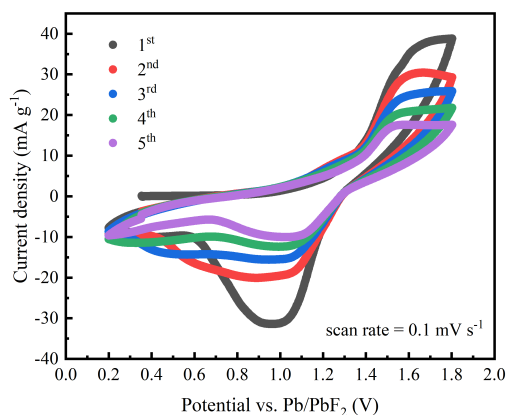
From the GCD curve of the Ag-5-1 cell, it is evident that there is a singular plateau during the initial charging phase, commencing at 1.5 V. This aligns with the noticeable slope change observed in the CV curve at 1.5 V (Fig. 4.5c). The presence of this plateau in GCD, along with the final oxidation peak in CV, implies the occurrence of the $\text{Ag} \rightarrow \text{AgF}$ oxidation reaction. Moreover, the plateau around 1.0 V corresponds to the reduction peak at approximately 1.0 V in the CV, indicating the $\text{AgF} \rightarrow \text{Ag}$ reduction process. The GCD curve of Ag-5-1 also reveals another two plateaus during cycles 2 to 5 of the charging process, at around 1.05 V and 1.2 V. This suggests the occurrence of other oxidation processes at the cathode, signifying the formation of distinct materials after the first cycle of charging and their subsequent oxidation at 1.05 V and 1.2 V. There is also a second

discharged plateau at around 0.55 V indicating another reduction process. A high level of reversibility was observed within 2 to 5 cycles. However, an interesting observation is that the charge-specific capacity of Ag-5-2 continues to increase from the second cycle to the last cycle, and the discharge-specific capacity shows a continuous increment.



(a) GCD curve of Ag-5-1 at current density of 5.2 mA g^{-1} .

(b) GCD curve of Ag-5-2 at current density of 5.2 mA g^{-1} .



(c) CV curve of Ag-5-3.

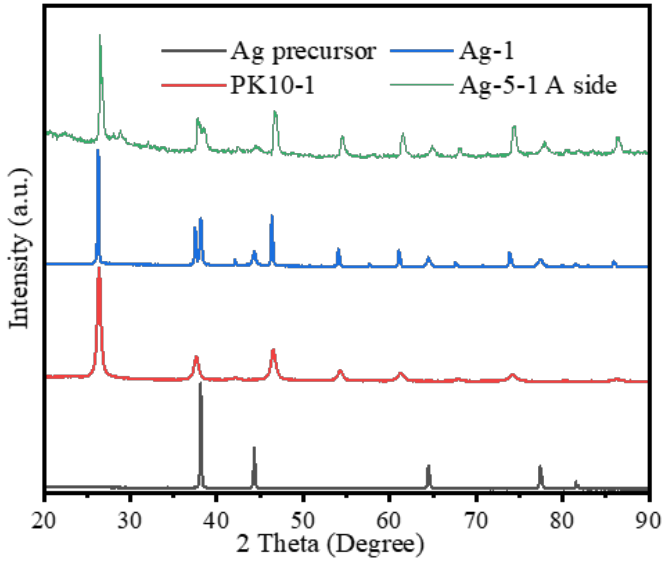
Figure 4.5: GCD and CV curve of Ag full cells at room temperature, each for five cycles.

After analyzing the electrochemical performance of the Ag full cell, ex situ XRD measurement is conducted to explore the irreversible materials at the cathode after cycling. It can be observed in Fig.4.6a that Ag exhibits four prominent peaks positioned at 38.29° , 44.51° , 64.73° , and 77.74° . Nevertheless, these primary peaks of Ag appear broadened, accompanied by a decrease in intensity. This phenomenon may be attributed to the electrochemical charge-discharge process, where Ag particles undergo decomposition into smaller-sized particles, consequently slightly affecting their crystallinity. This alteration in size and crystallinity could also contribute to the observed capacity fade. Although Wang et al.[78] suggested that a portion of AgF generated during the initial charge was not converted back to Ag in the subsequent discharge, no AgF phase was detected in

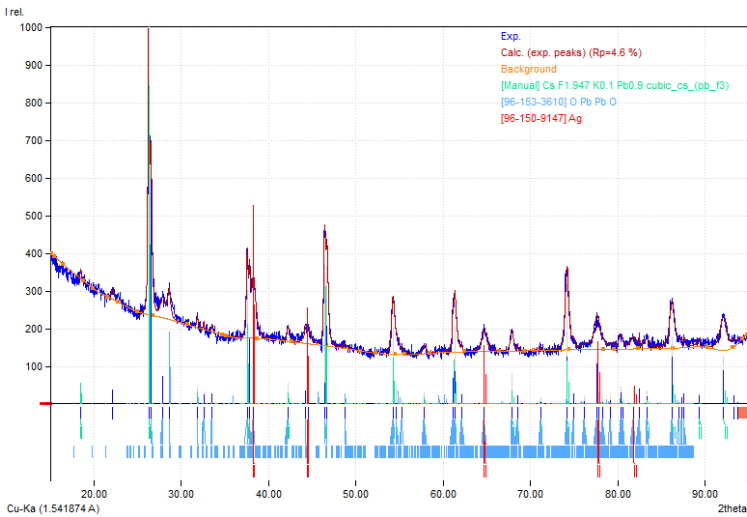
the pellet on A side after 5 cycles charge and discharge (Fig. 4.6b). However, additional obvious peaks are still observed which were identified as PbO. This is strange as in the original cathode composite, only PK10 has a Pb element. And according to the report of Wang et al. [52], potential products of the electrochemical decomposition for PK10 predicted from ab initio calculations are CsPbF₃ and Cs₂KPbF₆. The peaks belonging to PK10 are also influenced by the presence of PbO. Although they appear asymmetric, due to the presence of PbO, it is difficult to determine whether the electrolyte is actually decomposing or not.

For the CV measurement, the scan rate may influence the performance of the reversibility of the materials. Under high scanning speeds, materials that are initially reversible may tend to exhibit irreversible behavior. For this full cell, a scan rate of 0.1 mV s⁻¹ or even 0.02 mV s⁻¹ would be more suitable to accurately assess the reversibility of the cell.

But overall, the Ag full cell test was successful, as a reversible capacity close to the theoretical one could be attained. Consequently, we can broaden the scope of solid-state fluoride-ion batteries and explore other cathodes, such as metal oxides that may form metal oxyfluorides during electrochemical reactions. In this project, Cu₂O, FeO, and Mn₂O₃ are utilized as cathode material. The hope is to determine whether these full cells can operate at room temperatures while maintaining good electrochemical performance and analyze the phase changes that are accompanied by these electrochemical processes.



(a) XRD pattern of A side for Ag-5-1 cell, compared with XRD pattern of Ag-1, Ag precursor and PK10-1.



(b) XRD pattern of A side for Ag-5-1 cell. Ag in red line, PbO in blue line and PK10-1 in green line.

Figure 4.6: The XRD pattern of the Ag-5-1 pellet on cathode side (A side).

4.3. ROOM TEMPERATURE TESTING OF Cu_2O , FeO , Mn_2O_3 FULL CELLS

4.3.1. ROOM TEMPERATURE TESTING OF Cu_2O FULL CELL

The Cu_2O full cells utilize Cu_2O as the active material at the cathode, PK10 as the electrolyte, and Pb/PbF₂ composite as the anode. The Cu_2O precursor was initially analyzed using XRD measurement, as shown in Fig.4.7a, and was found to be highly pure. The three strongest peaks located at 36.38°, 42.26°, and 61.30° correspond to the crystallographic planes (111), (020), and (202), respectively. The Rietveld refinement of the Cu_2O cathode composite, referred to as Cu_2O -1, is presented in Fig.4.7b. The synthesized ratio of the composite is 3:6:1 (Cu_2O : PK10-3: CNTs). However, the refinement indicates a ratio of 48:52 (Cu_2O : PK10-3), deviating significantly. But it's worth noting that a larger amount of anode composites is employed to ensure the complete reaction of the cathode. The Cu_2O |PK10|Pb/PbF₂ full cells are tested in this section. The full cells all have a nominal capacity of 1.5 mAh.

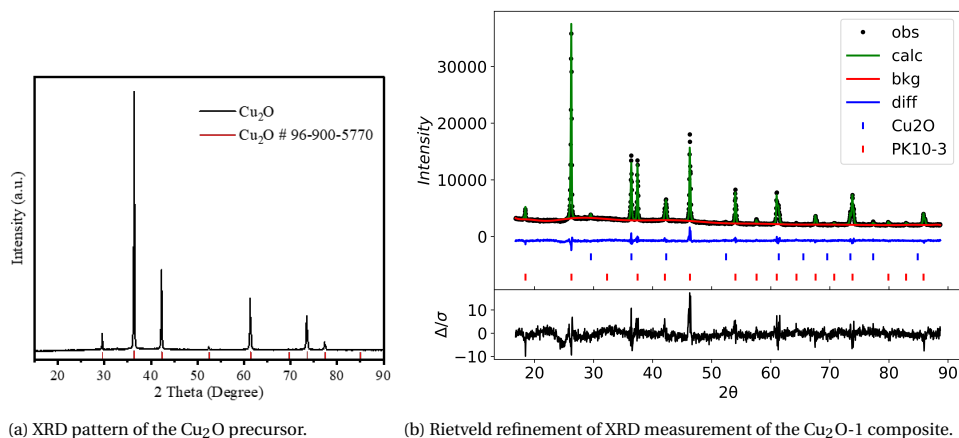


Figure 4.7: XRD pattern of the Cu_2O precursor and refinement of the Cu_2O -1 XRD pattern.

Galvanostatic charging and discharging measurements were performed for the C-5-1 cell, with the voltage limit set between 0.4 V and 1.5 V. In Fig.4.8a, a distinct plateau is noticeable during the initial charging process, as depicted in Fig.4.8a. The specific capacity after the first charging reaches 0.35 mAh/g, a notably low value that corresponds to approximately 0.09% of the theoretical specific capacity of 373.97 mAh/g. This corresponds to a capacity of 1.39×10^{-6} , representing only 0.07% of the employed capacity. The specific discharge capacity is even lower, measuring 0.03 mAh/g. Capacity fade becomes apparent starting from the second cycle. The reason for the sawtooth pattern observed in some parts of the curves is attributed to the slow rise in battery capacity. When the specific capacity of the battery remains consistent at similar voltages without significant growth, a sawtooth pattern may emerge. Additionally, the plateau seems to be on the verge of appearing in the subsequent charge and all the discharge cycles. Therefore, the

voltage limit window needs to be expanded to observe the further reaction performance.

For cell C-5-2, the voltage limit window is set to be 0.2 V to 1.75 V. It is noticeable that the specific charge capacity in the first cycle increases to 0.88 mAh/g, corresponding to a capacity of 3.55×10^{-6} mAh. The observed actual specific charge capacity of 0.88 mAh/g is merely 0.2% of the theoretical specific capacity of 373.97 mAh/g. Despite being higher than the specific capacity of the C-5-1 cell, it remains exceptionally low. However, this performance is still quite low for a battery. From the Fig.4.8c, The voltage plateau during the charge from cycles 2 to 5 is noticeably situated at around 1.7 V, starting from 1.4 V. Nevertheless, the plateau during the discharge process remains indiscernible. So, there is a need to either expand the voltage limit window or decrease the potential barrier for the electrochemical reaction to facilitate its occurrence. This will be elaborated upon in Section 4.5.

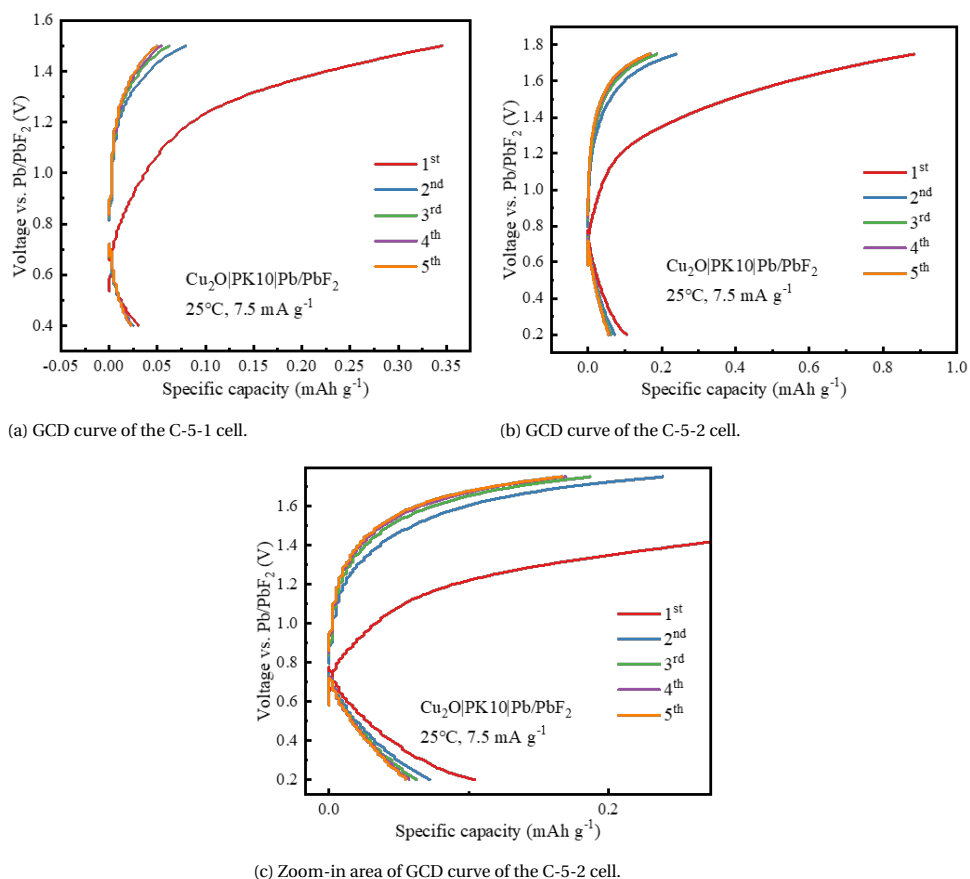


Figure 4.8: GCD curves of C-5-1 and Cu-5-2 cells, both tested at room temperature, running for five cycles.

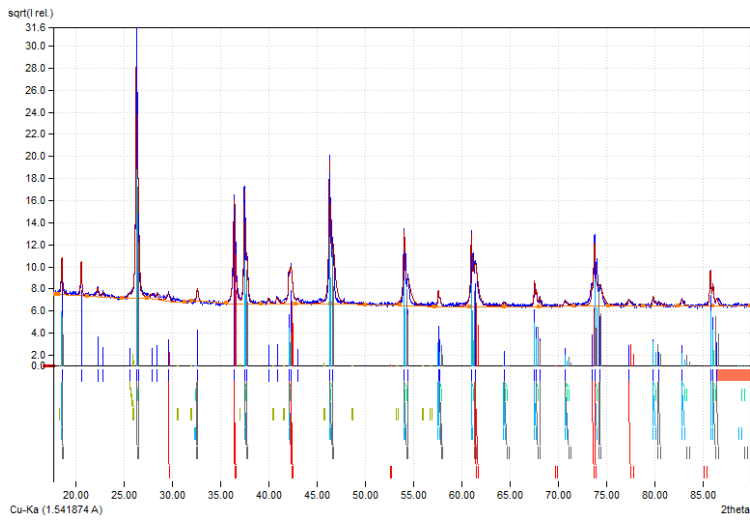


Figure 4.9: XRD pattern of the cathode side (A side) of the cell C-5-2. Green lines for PK10-3, gray cyan lines for Cs_2KPbF_6 , blue and gray lines for CsPbF_3 and red lines for Cu_2O .

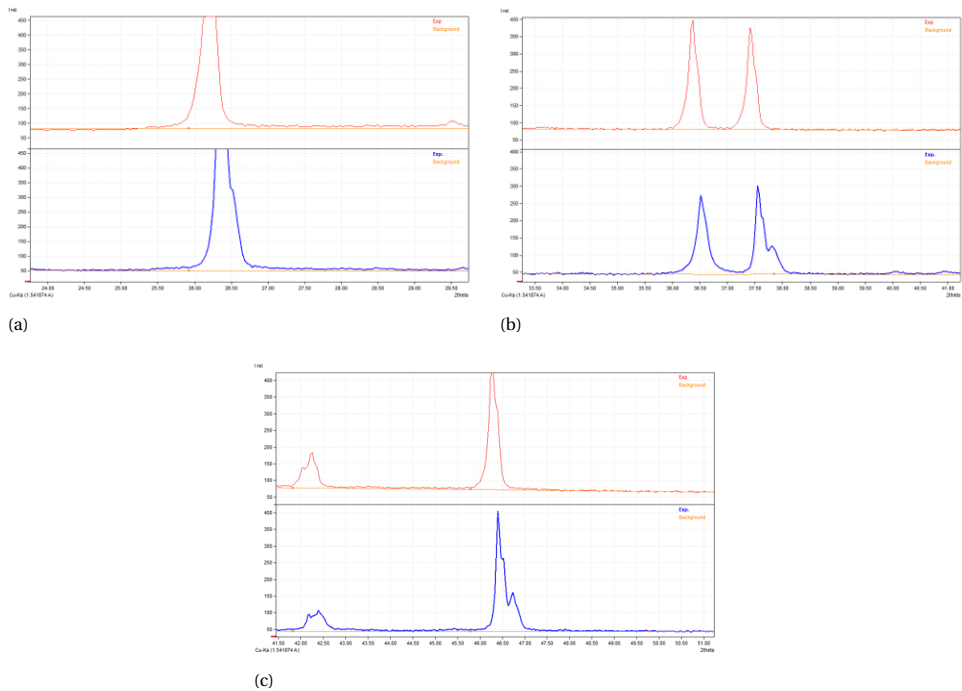
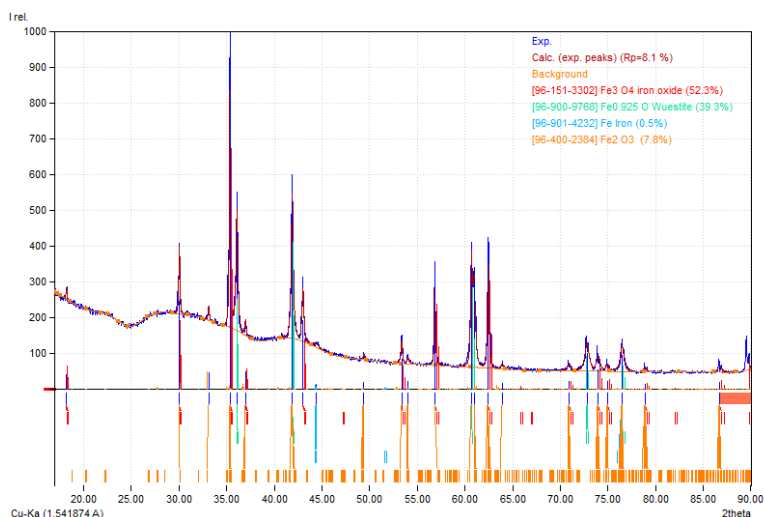


Figure 4.10: The XRD zoom-in region highlights the main peaks of the electrolyte in Cu_2O -1 (marked with a red line) and in the pellet of the C-5-2 cell on the cathode side (Cathode side, marked with a blue line).

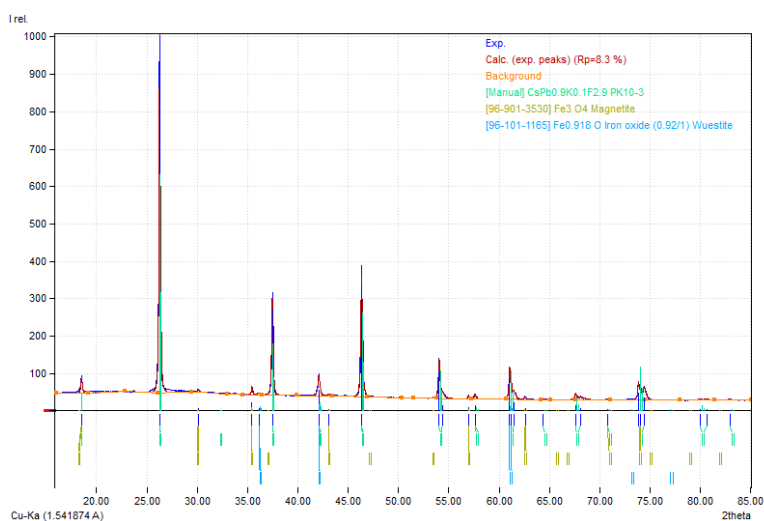
Despite the electrochemical performance, the XRD pattern of the A side of the cell C-5-2 is shown in Fig. 4.9. Except for the Cu_2O , no other materials containing Cu elements are detected. This is quite reasonable, given the limited capacity achieved, indicating that only a small amount of materials participate in the reaction. However, Cs_2KPbF_6 and CsPbF_3 are detected with low intensity, suggesting a slight decomposition of the electrolyte. This is evident in the zoom-in region (Fig. 4.10, where the three main peaks of the PK10 are broadened, and there is a splitting of the peaks attributed to the presence of CsPbF_3 . This suggests the possibility that PK10 may exhibit slight electrochemical activity, and there could potentially be electrolyte decomposition occurring. Nevertheless, it is important to note that several peaks located at 20.50° , 22.23° , 22.79° , and 28.33° were not detected, with the first peak exhibiting a relatively strong intensity.

In summary, the Cu_2O full cell demonstrates unsatisfactory electrochemical performance at room temperature, primarily reflected in the notably low specific capacity of the cathode. Additionally, the suitability of the electrolytes for the cathode raises questions, considering the potential electrolyte decomposition.

4.3.2. ROOM TEMPERATURE TESTING OF FeO FULL CELL



(a) XRD pattern of FeO precursor. FeO in green lines, Fe₃O₄ in red lines, Fe₂O₃ in orange lines and Fe in blue lines.



(b) XRD pattern of FeO-1 composite. PK10-3 in green lines, Fe₃O₄ in army green lines, and FeO in blue lines.

Figure 4.11: XRD pattern of FeO precursor and FeO-1 composite.

The FeO full cells utilize FeO as the active material at the cathode, PK10 as the electrolyte, and Pb/PbF₂ composite as the anode. The FeO precursor underwent initial analysis using XRD measurement, as depicted in Fig. 4.11a. The analysis revealed the presence of multiple phases: FeO, Fe₃O₄, Fe₂O₃, and metallic Fe, with respective ratios

of 39.3:52.3:7.8:0.5. This implies that the FeO precursor has undergone oxidation. The cathode composite derived from FeO is labeled as FeO-1 . The XRD pattern of FeO-1 , depicted in Fig.4.11b, reveals the presence of FeO , Fe_3O_4 , and PK10 phases, while Fe_2O_3 and metallic Fe are notably absent. This observation is intriguing, given the original ratio of 3:6 between the FeO precursor and electrolyte. According to the precursor analysis, there should be approximately 7.8% Fe_2O_3 , translating to about 2% Fe_2O_3 in the composite. Nevertheless, since there are no other impurities present in the composite, it remains a viable option for use. The nominal capacity of the FeO full cell, Fe-5-1 , should be 1 mAh. However, due to excessive impurities, the actual employed capacity is only around 0.4 mAh.

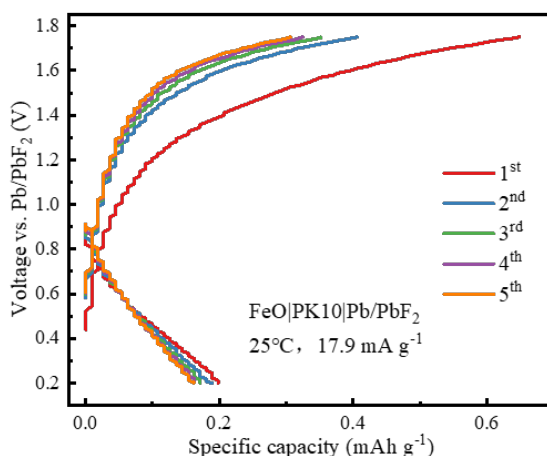
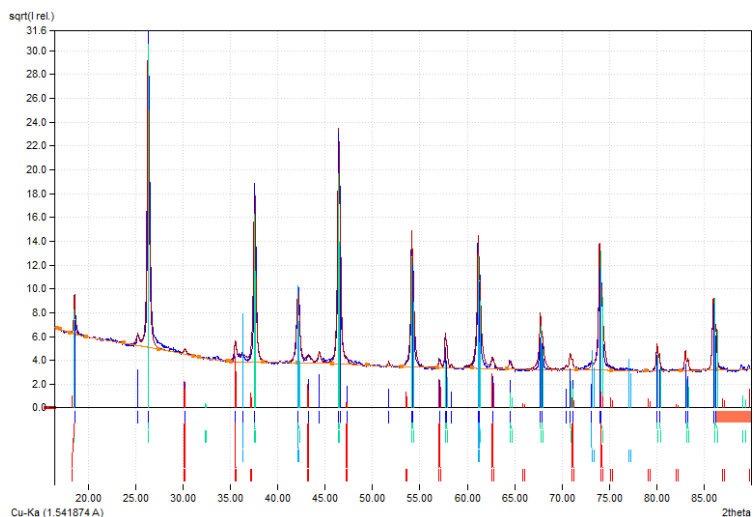


Figure 4.12: GCD curve for cell Fe-5-1 running at room temperature for five cycles.

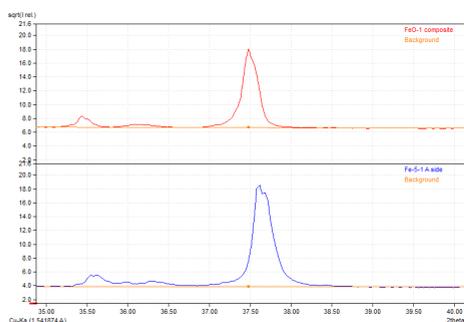
In Fig.4.12, the GCD curve of the Fe-5-1 cell after five cycles is presented. The specific charge capacity in the first cycle is measured at 0.65 mAh/g, representing only 0.17% of the theoretical specific capacity of 372.42 mAh/g. A capacity fade is evident after the initial cycle, with the specific capacity decreasing to 0.41 mAh/g. The specific discharge capacity is even lower at 0.2 mAh/g during the first cycle. Notably, the plateaus observed during the charge in cycles 2 to 5 commence around 1.6 V to 1.7 V, mirroring the behavior observed in the Cu_2O full cell.

The XRD pattern of the A side (cathode side) pellet of the Fe-5-1 cell is depicted in Fig.4.13a. Apart from the identified matches for PK10-3, FeO , and Fe_3O_4 , no other materials are detected. However, three peaks located at 25.24°, 44.39°, and 51.68° remain unmatched with any suitable materials based on the elements Fe , O , Cs , Pb , K , and F . Observing Fig.4.13b and Fig.4.13c, a slight splitting of the peaks associated with the PK10-3 electrolyte is evident. This phenomenon may suggest a minor decomposition of the electrolyte.

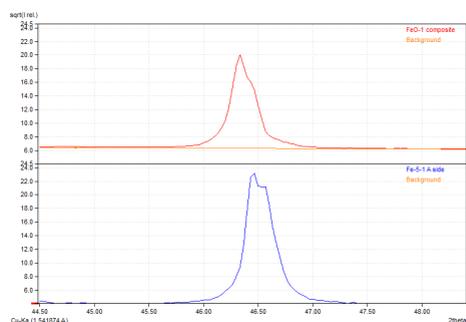
In conclusion, similar to the challenges encountered by the Cu_2O full cell operating at room temperature, the FeO full cell also fails to deliver satisfactory capacity under these conditions.



(a) XRD pattern for the cathode side (A side) of Fe-5-1 after GCD. PK10-3 in green lines, FeO in blue lines, and Fe_3O_4 in red lines.



(b) comparison of the peaks of PK10 before and after GCD. FeO-1 composite in red lines and A side of Fe-5-1 after GCD in red lines.

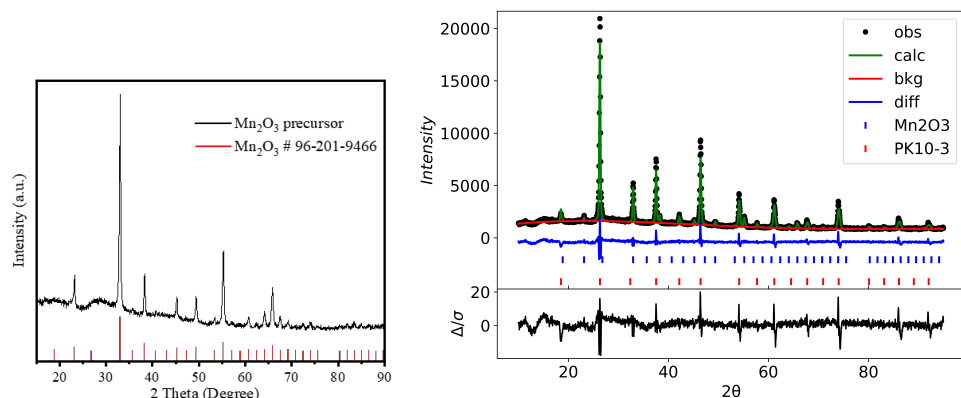


(c) comparison of the peaks of PK10 before and after GCD. FeO-1 composite in red lines and A side of Fe-5-1 after GCD in red lines.

Figure 4.13: The XRD pattern for the cathode side (A side) of Fe-5-1 after GCD, along with a comparison of the peaks of PK10 before and after GCD, as illustrated in the zoomed-in areas.

4.3.3. ROOM TEMPERATURE TESTING OF Mn_2O_3 FULL CELL

The Mn_2O_3 precursor was initially analyzed and found to be highly pure. The Rietveld refinement of the Mn_2O_3 cathode composite, denoted as Mn_2O_3 -1, is presented in Fig. 4.14b. The synthesized ratio of the composite is 3:6:1 (Mn_2O_3 : PK10-3: CNTs). However, the refinement indicates a slightly deviated ratio of 42.6:57.4 (Mn_2O_3 : PK10-3). The Mn_2O_3 |PK10|Pb/PbF₂ full cell named Mn-5-1 is used for galvanostatic charge and discharge testing in this section, and it exhibits a nominal capacity of 1 mAh.

(a) XRD pattern of the Mn_2O_3 precursor.(b) Rietveld refinement of XRD measurement of the Mn_2O_3 -1 composite.Figure 4.14: XRD pattern of the Mn_2O_3 precursor and refinement of the Mn_2O_3 -1 XRD pattern.

From the GCD curve of Mn-5-1 shown in Fig. 4.15, it is observed that the specific charge and discharge capacities of the first cycle are 1.17 mAh/g and 0.65 mAh/g, respectively. This specific charge capacity is only 0.35% of the theoretical specific capacity of 338.95 mAh/g.

Despite having the smallest theoretically expected specific capacity, Mn-5-1 exhibits the largest specific capacity at room temperature among these three cells. Additionally, it shows the lowest capacity fade. The plateau during the charge process occurs at approximately the same voltage, around 1.7 V.

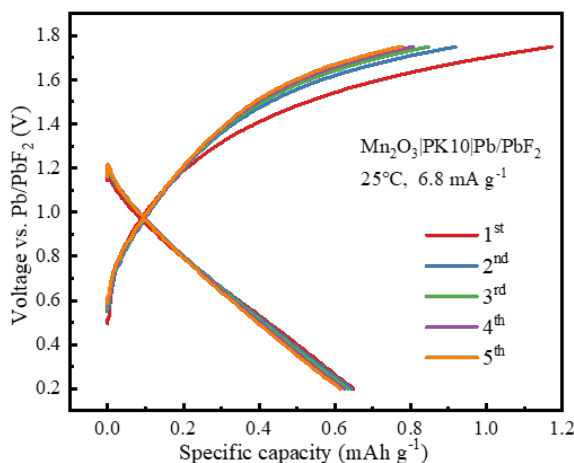


Figure 4.15: GCD curve for cell Mn-5-1 running at room temperature for five cycles.

The XRD pattern of the cathode pellet after charge and discharge shows no other peaks except the peaks for Mn_2O_3 and PK10-3 as seen in Fig. 4.16. However, upon closer

examination of the main peaks in the zoomed-in region, which correspond to the electrolyte peaks, it is evident that these peaks exhibit greater asymmetry compared to those in the original Mn_2O_3 -1 composite. Additionally, there is increased splitting in the peaks, suggesting a potential electrochemical activity of the electrolyte.

The Cu_2O , FeO , and Mn_2O_3 full cells generally show significantly low specific capacity at room temperature, possibly attributed to limited electronic diffusion in the electrode. However, interestingly, the plateaus in the GCD curve during charge are consistent among these three types of batteries: Cu_2O full cell, FeO full cell and Mn_2O_3 . And varying degrees of peak splitting of the electrolyte PK10 is observed in all these cells, indicating a potential electrochemical activity of the electrolyte PK10.

The curiosity arises as to whether the operating voltage range of these batteries at room temperature has exceeded the electrochemical stability window (ESW) of the electrolyte PK10. Therefore, the insignificant capacity is likely supplied by the decomposition of the electrolyte, explaining why the plateau voltage positions observed on the GCD (Galvanostatic Charge-Discharge) curve are so closely aligned. Therefore, it is advisable to verify the electrochemical stability window of the electrolyte. Linear sweep voltage measurements are frequently employed to assess the electrochemical stability window of the electrolyte. However, prior to conducting such tests, it is imperative to establish that the Pb/PbF_2 anode can serve as the reference electrode and that the working voltage window of the Pb/PbF_2 anode falls within the electrolyte's electrochemical stability window (ESW). Furthermore, it is essential to exclude the impact of the Pb/PbF_2 composite anode. Therefore, symmetric cell testing utilizing Pb/PbF_2 composite electrodes on both the anode and cathode sides is conducted. This will be discussed in detail in the next subsection.

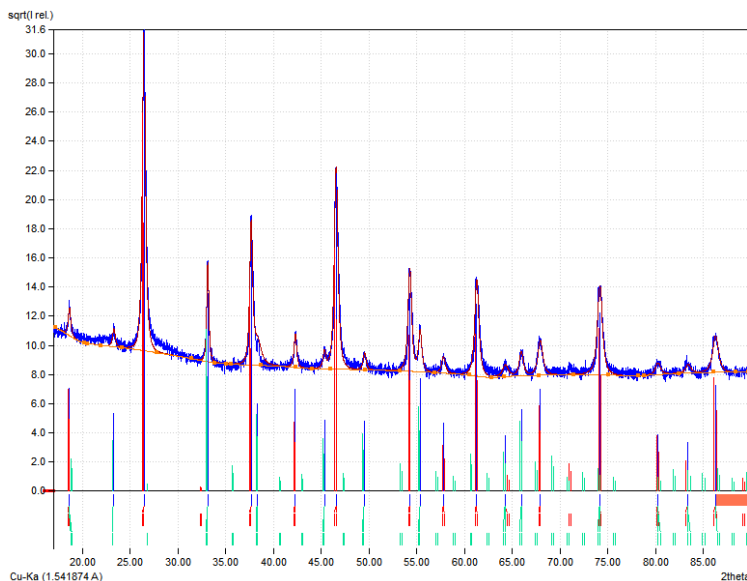


Figure 4.16: XRD pattern for the cathode (A side) pellet of the cell Mn-5-1. PK10-3 in red lines and green lines for Mn_2O_3 .

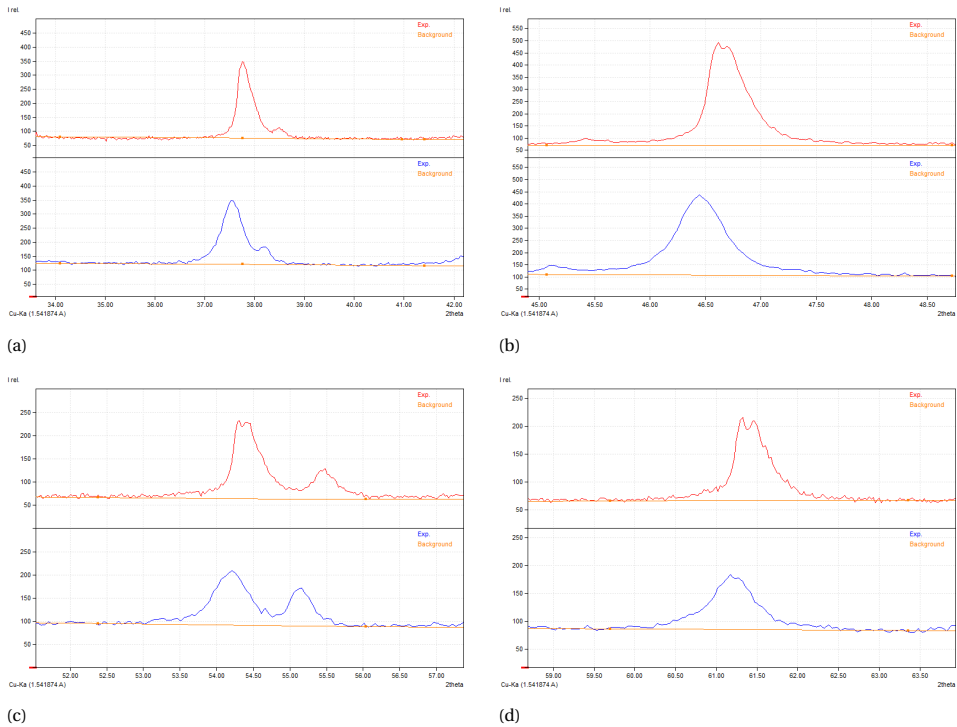


Figure 4.17: The XRD zoom-in region highlights the main peaks of the electrolyte in Mn_2O_3 -1 (marked with a blue line) and in the pellet of the Mn-5-1 cell on the cathode side (A side, marked with a red line).

4.4. SYMMETRIC CELL TESTING

To do the symmetric cell testing, we use Pb/PbF₂ anode to be the active materials both on A side (cathode side) and B side (anode side). However, the mass of the composite used on the B side is twice that of the A side, aiming to ensure a thorough reaction of the active material on the A side.

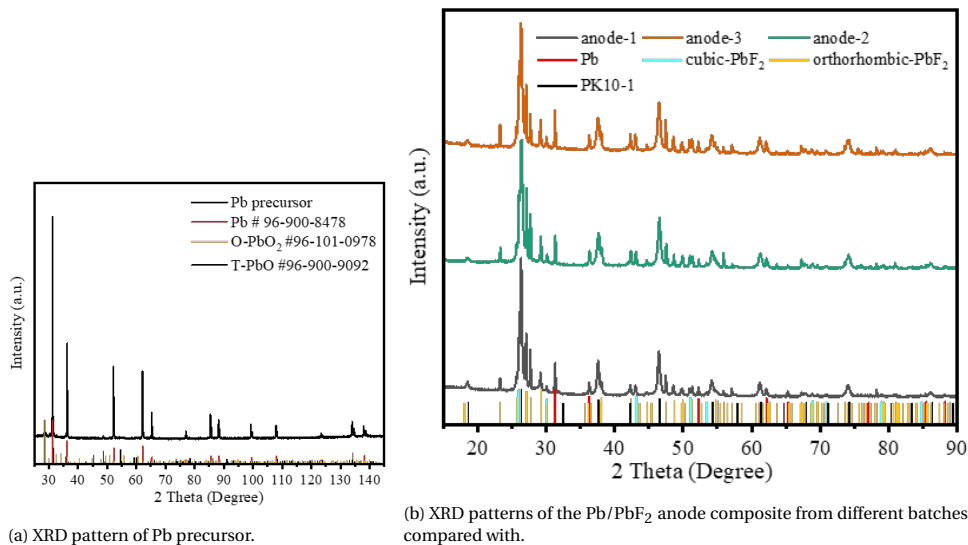


Figure 4.18: XRD patterns of the Pb precursor and Pb/PbF₂ anode composite from different batches.

The PbF₂ precursor is discussed in section 4.1, so only the Pb precursor needs to be discussed here. Figure 4.18a illustrates that the Pb precursor comprises three phases: cubic lead metal, orthorhombic PbO₂ (scrutinyite), and tetragonal PbO (litharge), with a ratio of 92.2:3.3:4.5. The presence of scrutinyite and litharge indicates the oxidation of a small amount of the Pb precursor. The XRD patterns of various batches of the Pb/PbF₂ anode composite are presented in Figure 4.18b. Refining the anode composites poses challenges, as previously mentioned. The issue arises from the inability to determine with high certainty the position of the lighter atoms (F and O) relative to the Pb sublattice. Consequently, there is a corresponding uncertainty in simulating the scattering in the Rietveld procedure, and this uncertainty extends to the determination of phases by the bespoke procedure. Therefore, obtaining substantial information from the lighter atoms present in each CIF used for Rietveld refinement is not anticipated. Especially when there are numerous additional phases, the task becomes even more challenging and prone to inaccuracy. However, the phase fraction obtained from matching and refinement can serve as a reference, and the ratio of PK10:Pb:c-PbF₂:O-PbF₂ is approximately 62:6:7:25. The proportion between cubic PbF₂ and orthorhombic PbF₂ is nearly identical to that in the PbF₂ precursor. Nevertheless, it seems there is a lower concentration of lead metal in the composites. This could be attributed to the presence of Pb oxide, which forms a thin cover on the Pb particles. These layers on the surface of the Pb

particles would likely be very thin or possibly have an amorphous phase, making them challenging to detect by XRD. Also, in the full cell configuration, the actual active material within the Pb/PbF₂ composite is PbF₂, rather than Pb when used as an anode during the charging process, which constitutes the first half-cycle. Therefore, even if there is a deviation in the Pb ratio, it should not influence the performance of the full cell significantly.

4.4.1. ELECTROCHEMICAL PERFORMANCE

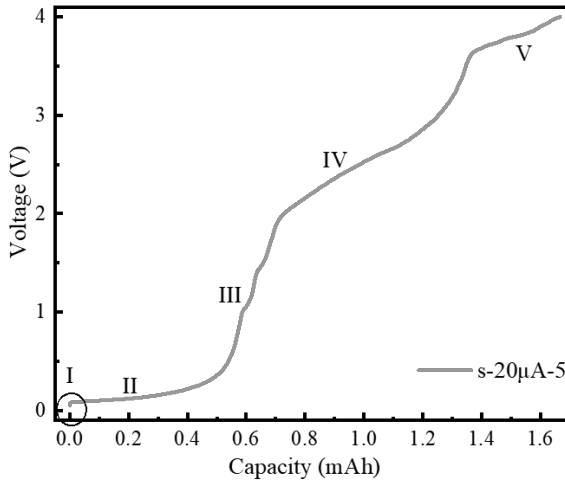
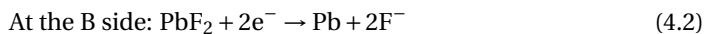
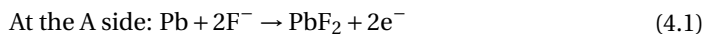


Figure 4.19: GCD curve of the cell s-20 μ A-5, which is charged to 4 V.

As depicted in Fig. 4.19, the symmetric cell s-20 μ A-5 exhibits a distinct GVD curve upon charging to 4 V, highlighting five noteworthy segments. Notably, in the first part (I), the initial potential is observed at 0.095 V instead of 0 V. In reality, given that the composite materials on both A and B sides are identical, the potentials on these two sides should theoretically be equal, indicating a starting potential of zero. However, the observed voltage disparity can be attributed to the presence of ohmic resistance. Ohmic polarization manifests promptly upon the initiation of current flow, stemming from contact resistances among the electrolyte, electrode materials, membrane, and various components. And Ohmic polarization should be directly proportional to the magnitude of the current. We can observe some initial instability in the first few data points, attributed to the transient effects induced by the recent initiation of current flow.

Moving on to the second part (II), it appears as a plateau but exhibits a slight slope. This plateau results from the oxidation of Pb on the A side and the reduction of PbF₂ on the B side, as indicated by the following equation:



When there is a charge balance and material equilibrium in the electrode reaction, a constant potential difference is established, known as the electrode's equilibrium potential. However, when an external current passes through, it disrupts this equilibrium state, causing a change in the electrode potential. And the marginal slope of the plateau is attributed to polarization. Polarization encompasses three types: ohmic polarization, concentration polarization, and electrochemical polarization. We have discussed Ohmic polarization before. Concentration polarization arises due to the insufficient replenishment of reactants at the electrode surface, either because of their consumption without timely replenishment or the accumulation of certain products that cannot be promptly removed. This leads to a deviation in the electrode potential. In the illustration below (Fig. 4.20), concentration polarization is exemplified by the slow diffusion of fluoride ions in the solid-state electrolyte. This sluggish diffusion results in the insufficient supply of reactants to the A side surface. By the time the current has left the electrode on the A side, fluoride ions have not reached the electrode surface region in time, causing their concentration at the electrode surface to be lower than in the bulk electrolyte. Consequently, a significant accumulation of positive vacancies occurs on the A electrode surface, leading to an excess of positive charges and an increase in the electric potential at the A side due to the resulting electric field. Electrochemical polarization, also known as activation polarization, occurs when the rate of electrochemical reactions involving positive and negative electrode-active substances is slower than the electron movement rate, leading to polarization. In essence, this implies that electrode reactions require a certain activation energy, causing a relatively slow reaction rate. Therefore, when a current flows through the cell, the slow electrochemical reaction causes a difference in the degree of electrode charging compared to the reversible case. This results in a deviation of the electrode potential, known as electrochemical polarization. Both concentration polarization and activation polarization leads to an increase in voltage on the A side.

The occurrence of the third segment (III), marked by a significant change in slope on the curve, signifies the reaction starts off unbalanced and eventually, electrolytes begin to undergo slight decomposition. This leads us to the fourth section (IV). In this part, a second plateau emerges, corresponding to the voltage associated with electrolyte oxidation. Subsequently, a third plateau becomes evident at higher voltage (V), commencing at approximately 3.6 V. This may be attributed to the reaction involving carbon nanotubes: $C + F^- \rightarrow CF + e^-$, as proposed by Nowroozi et al. [31].

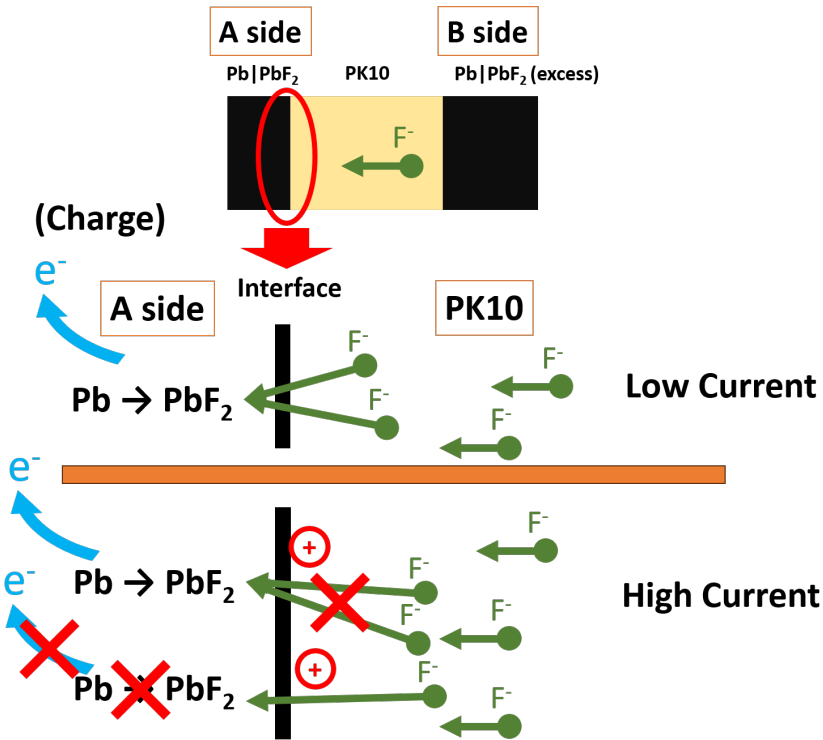
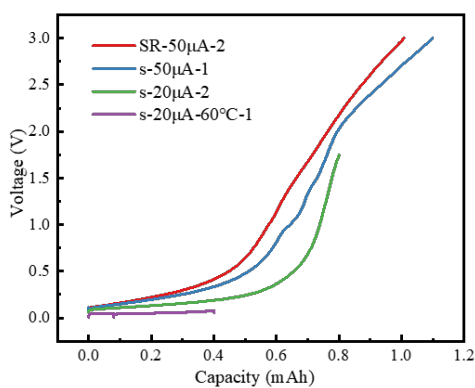
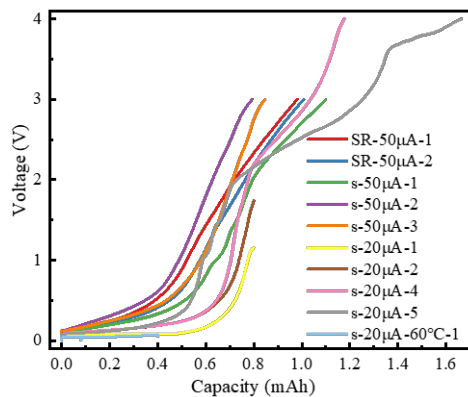


Figure 4.20: Polarization schematic plot.

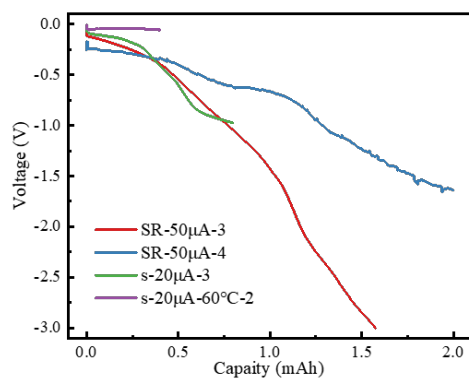
There are four types of symmetric cells named $s\text{-}50\mu\text{A}$, $s\text{-}20\mu\text{A}$, SR and SW. The $s\text{-}50\mu\text{A}$ type involves the correct configuration of cell assembly, using hand-milled anode composite, and testing the cell under a current of $50\mu\text{A}$. The correct assembly configuration of the cell involves following the correct order: first, press the electrolyte to the pellet, then assemble the B side, and finally the A side. Similarly, $s\text{-}20\mu\text{A}$ involves the correct configuration of cell assembly, employing hand-milled anode composite, and testing the cell under a current of $20\mu\text{A}$. SR signifies the correct cell assembly configuration, where rubber rings are removed during pellet pressing, and the pressing order is accurate. Anode-1 composite (produced using ball milling) is used in SR cells. SW indicates an incorrect cell assembly configuration, where rubber sealing rings are not removed during pellet pressing, and the order of pellet pressing is incorrect. In SW cells, the anode composite powder is first pressed on the B side, followed by pressing the electrolyte pellet, and then the pellet on the A side. During the pellet pressing stage, the battery device is never reversed, and the B side is consistently placed at the bottom of the battery. Anode-1 composite (produced using ball milling) is also used in SW cells.



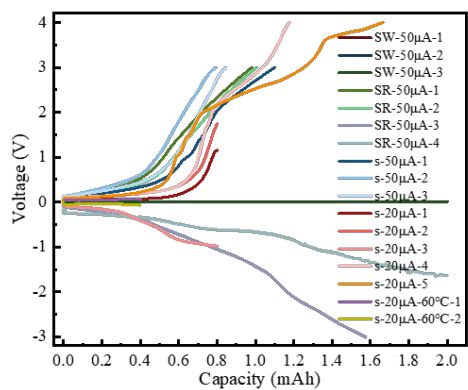
(a) GCD curves of representative charged symmetric cells.



(b) GCD curves of all charged symmetric cells.



(c) GCD curves of all discharged symmetric cells.



(d) GCD curves of all the symmetric cells.

Figure 4.21: GCD curves of the symmetric cells.

It can be observed in Figure 4.21d that the GCD curve of the SW cells comprises several horizontal lines along the x-axis, indicating the absence of capacity. Consequently, the SW cells experienced a complete failure in operation. This is due to the fact that, when adding the powder to the B side, the powder will be trapped on the wall of the cylinder. This situation can lead to a short circuit when the B side is connected to the A side, as illustrated in Fig. 4.22. Additionally, when compressing the electrode with the rubber sealing rings, the pressure applied to the electrode is less than the specified value, which is not conducive to the compaction process.

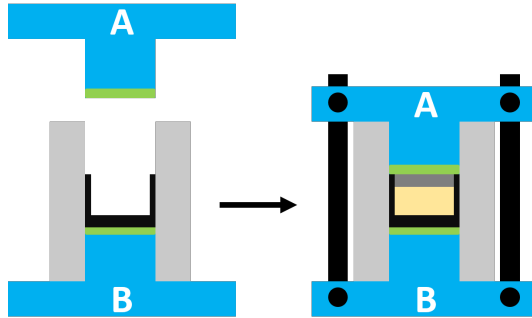
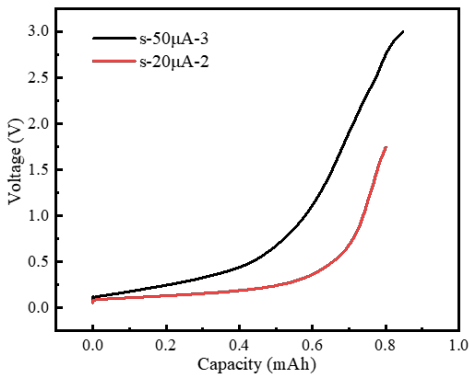
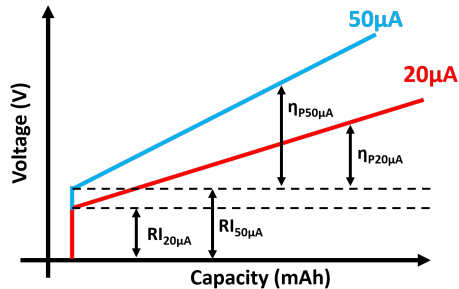


Figure 4.22: Pressing the electrode pellet first instead of pressing the electrolyte pellet first will cause a short circuit.



(a) Zoom-in area of cell s-50 μ A-3 and s-20 μ A-2.



(b) Schematic plot of the zoom-in area of cell s-50 μ A-3 and s-20 μ A-2.

Figure 4.23: Polarization comparison between cells using 50 μ A and 20 μ A.

Now, let's shift our attention to stages I, II, and III, as these segments collectively play a crucial role in determining the performance of the Pb/PbF₂ composite. The average ohmic drop and the average slope of the first plateau are calculated for SR-50 μ A, s-50 μ A, s-20 μ A, and s-20 μ A-60 $^{\circ}$ C cells, as illustrated in Table 4.3 and Table 4.4. The average capacity achieved by the anode composite before any discernible electrolyte de-

composition is calculated and presented in Table 4.5. There is minimal difference in ohmic drop observed between SR-50 μ A and s-50 μ A cells, with both exhibiting an average ohmic drop of approximately 0.1 V. The first plateau of SR-50 μ A cells appears slightly flatter than that of s-50 μ A cells, with average slopes of 0.95 and 1.05, respectively. Despite this, the average capacity of s-50 μ A cells surpasses that of SR-50 μ A cells, reaching 0.48 mAh compared to the latter's 0.43 mAh. This similarity is reasonable, considering that the ball milling rate for the anode-1 used in SR-50 μ A is quite low, specifically at 100 rpm. The performance of symmetric cells operating at 20 μ A is notably superior, characterized by a lower average ohmic polarization of only 0.079 V. Additionally, the plateau is flatter, with the average slope decreasing to 0.31, and the average capacity is higher, reaching 0.64. From Fig.4.23, it is evident that cells operating at lower currents exhibit reduced ohmic polarization ($R = U \times I$). Additionally, these cells demonstrate lower combined activation and concentration polarization, as indicated by the flatter plateau observed in the charge profile. Elevating the temperature further enhances performance, as evident in the s-20 μ A-60 $^{\circ}$ C cells. For analysis, we exclusively consider the data acquired before the voltage protection of the equipment, as this dataset is sufficient for highlighting the advantages of increasing the temperature to 60 $^{\circ}$ C while maintaining a 20 μ A current. In s-20 μ A-60 $^{\circ}$ C-1, the first plateau is nearly a straight line, closely parallel to the x-axis. The ohmic drop decreases to only 0.033 V, and the slope is 0.064, approaching zero.

4

	SR-50 μ A	s-50 μ A	s-20 μ A	s-20 μ A – 60 $^{\circ}$ C
1	0.1009	0.0875	0.0828	0.0330
2	0.1002	0.1096	0.0773	discharge
3	discharge	0.1102	discharge	-
4	discharge	-	0.0799	-
5	-	-	0.0748	-
average ohmic drop (V)	0.10	0.10	0.079	0.033
standard error	0.00035	0.010	0.0030	0
ohmic drop (V)	0.1 ± 0.00035	0.1 ± 0.010	0.079 ± 0.0030	0.033 ± 0

Table 4.3: Ohmic drop

	SR – 50 μ A	s – 50 μ A	s – 20 μ A	s – 20 μ A – 60°C
1	1.00065	0.68906	0.05647	0.063946
2	0.90279	1.34084	0.29556	discharge
3	discharge	1.10950	discharge	-
4	discharge	-	0.402358	-
5	-	-	0.494372	-
average slope	0.95	1.05	0.31	0.064
standard error	0.049	0.27	0.16	0
slope	0.95 \pm 0.049	1.05 \pm 0.27	0.31 \pm 0.16	0.064 \pm 0

Table 4.4: Slope

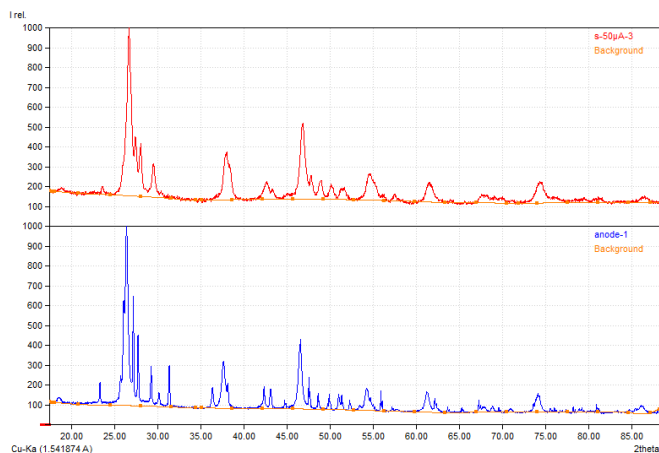
	SR – 50 μ A	s – 50 μ A	s – 20 μ A
1	0.3887	0.49767	0.67745
2	0.46409	0.43546	0.67758
3	discharge	0.50800	discharge
4	discharge	-	0.681819
5	-	-	0.517579
average capacity (mAh)	0.43	0.48	0.64
standard error	0.038	0.032	0.070
capacity (mAh)	0.43 \pm 0.038	0.48 \pm 0.032	0.64 \pm 0.070

Table 4.5: Capacity

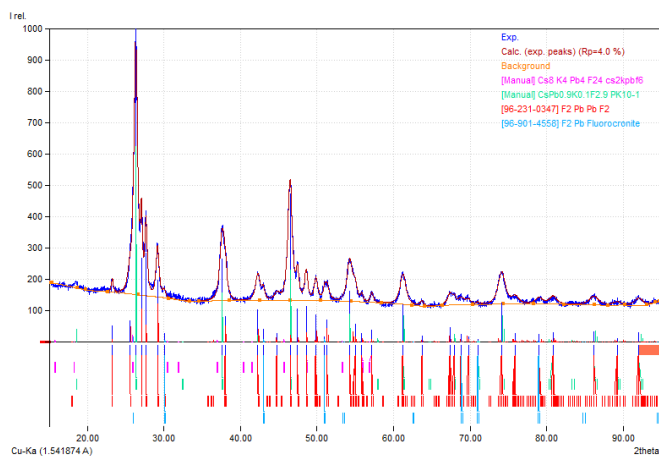
In the discharged cells, as illustrated in Fig.4.21c, it is evident that the symmetric cells perform optimally at lower currents and higher temperatures during the discharge process, mirroring its behavior during the charging process. The ohmic drop of the s-20 μ A-60°C cell is notably the lowest, followed by the s-20 μ A cell, and then the s-50 μ A cells. Additionally, the plateau in the s-20 μ A-60°C cell is more uniformly flat compared to other cells. The plateau of the cell utilizing 20 μ A at room temperature exhibits the second-highest level of stability.

4.4.2. XRD CHARACTERIZATION

It is evident that the peaks associated with Pb diminish during charge as seen in Fig. 4.24a. Specifically, the peaks located at 31.31° and 52.24° , attributed to Pb, disappear, and the peak at 36.30° , composed of Pb and orthorhombic PbF_2 , decreases dramatically. Additionally, the intensity of the peak at 42.50° corresponding to PK10 and orthorhombic PbF_2 reveals an increase, surpassing the peak at 43.23° attributed to cubic- PbF_2 . In the original anode-2 composite, these peaks were relatively similar in height. This is reasonable as Pb is oxidized to PbF_2 . However, definitively determining the extent of electrolyte decomposition poses a challenge, given the consistent influence of PbF_2 on the peaks of PK10. Confirming the formation of Cs_2KPbF_6 remains elusive under these circumstances. Considering that all $s\text{-}50\mu\text{A}$ cells are charged to 3 V, it can be reasonably inferred that the electrolyte in the anode composites has likely undergone decomposition, leading to the formation of CsPbF_3 and Cs_2KPbF_6 , or potentially PbF_3 , CsF , and Cs_2KPbF_6 , as predicted from quantum chemical simulations and corresponding thermodynamic data in the report by Wang et al. Interestingly, the peak of PbF_2 becomes more rounded, causing some nearby peaks to appear merged, forming a new broader peak. This phenomenon may be attributed to electrochemical reactions causing a reduction in particle size, akin to our previous discussion regarding Ag particles.

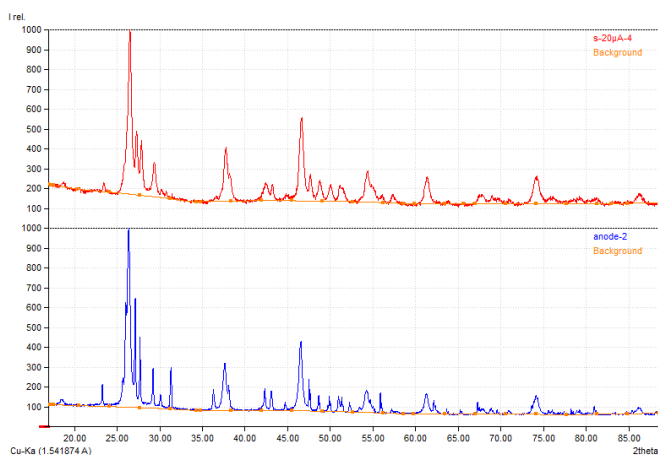


(a) Ex situ XRD patterns of A side of s-50 μ A-3 cell, compared with anode-2 composite. Anode-2 composite in blue line and s-50 μ A-3 in red line.

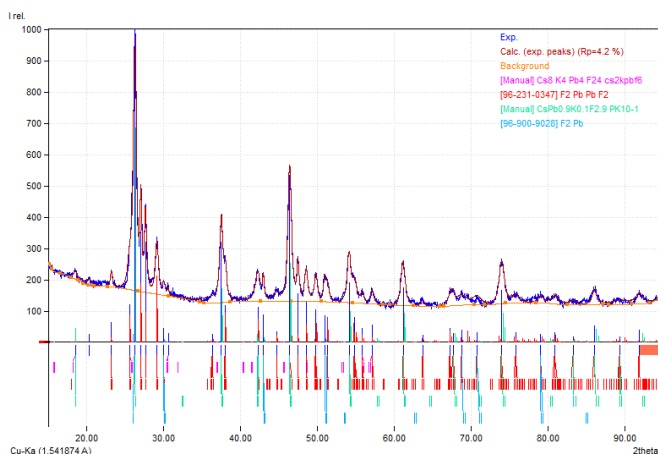


(b) XRD pattern of A side of s-50 μ A-3 cell. Cs₂KPbF₆ in purple line, PK10-1 in green line, orthorhombic PbF₂ in red line, and cubic PbF₂ in blue line.

Figure 4.24: XRD patterns of A side (cathode side) of s-50 μ A-3 cell, compared with anode-2 composite.



(a) XRD patterns of A side of s-20 μ A-4 cell, compared with anode-2 composite. Anode-2 composite in blue line and s-20 μ A-4 in red line.



(b) XRD pattern of A side of s-20 μ A-4 cell. PK10-1 in green line, orthorhombic PbF₂ in red line, and cubic PbF₂ in blue line.

Figure 4.25: XRD patterns of A side of s-20 μ A-4 cell, compared with anode-2 composite.

For s-20 μ A-4 charged cell, the XRD patterns reveal a disappearance of Pb peaks, mirroring the overall trend observed in s-50 μ A cells. Notably, in the XRD pattern of A side for s-20 μ A-4, Cs₂KPbF₆ is more distinctly detectable than other charged cells, as highlighted in the zoom region in Fig.4.26. This observation is reasonable, considering that s-20 μ A-4 is charged to the highest voltage (4 V), implying a more extensive electrolyte decomposition and a higher likelihood of Cs₂KPbF₆ formation.

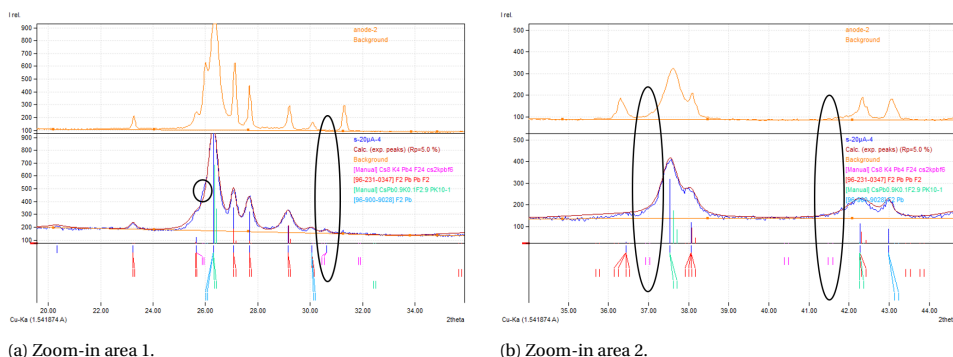


Figure 4.26: Zoom-in area of A side of s-20 μ A-4 cell and anode-2 composite. A side pellet in blue line, anode-2 in orange line, and Cs₂KPbF₆ in purple line.

The ex situ XRD pattern of the cathode pellet from the s-20 μ A-3 cell, depicted in Fig.4.27, reveals the presence of PK10-1, orthorhombic PbF₂, and elemental Pb. As the cell undergoes discharge, the primary reaction entails the reduction of PbF₂ to Pb. There's no cubic-PbF₂ phase detected which means it's reduced to Pb. According to Wang et al.'s calculations [52], the PK10 electrolyte is expected to decompose into KF, Pb, and CsF when the voltage drops below -0.1 V to -1.0 V. However, it is noteworthy that KF and CsF are not detected in the current analysis.

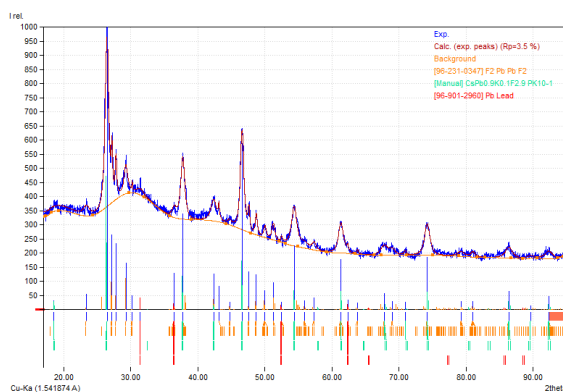


Figure 4.27: Ex situ XRD pattern of cell s-20 μ A-3 cell, which is discharged to -1.0 V. Pk10-1 in green, orthorhombic PbF₂ in orange, and Pb metal in red.

Collectively, our findings demonstrate that the Pb/PbF₂ composite can effectively serve as both the counter and reference electrode, particularly under conditions of lower current and higher temperatures. This observation excludes the impact of the anode on the full cell systems during testing at room temperature. While the precise electrochemical stability window (ESW) of our synthesized PK10 remains undetermined, we have adopted the Pb/PbF₂ composite as the reference electrode and PK10-CNTs composites as the working electrode for linear sweep voltage (LSV) measurements. This approach

aims to elucidate and ensure the ESW of PK10 in our experimental setup. The result of the LSV is displayed in Fig.4.28. It can be seen that the ESW of PK10 is between -0.14 V to 1.92 V. However, it is noticeable that slight electrolyte instability has been observed at specific voltage points near 0.14 V and 1.4 V. This suggests that the electrolyte PK10 may become electrochemically active at these two points. But the activity should be minimal at the outset.

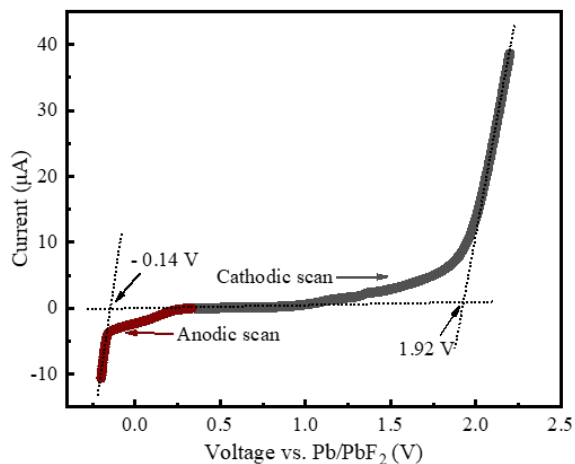
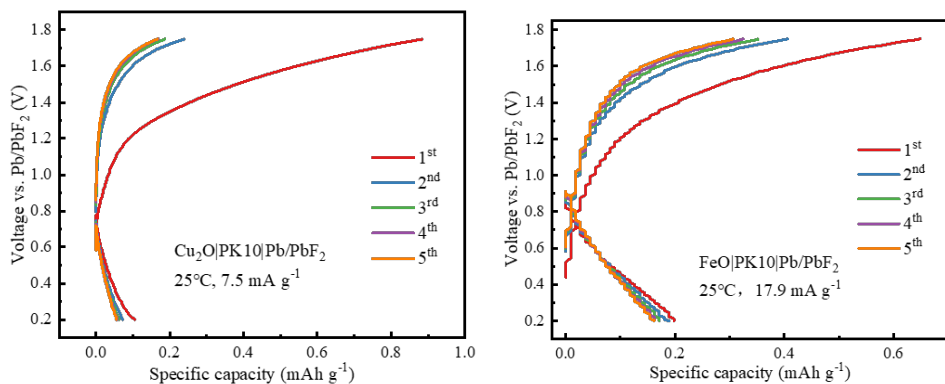
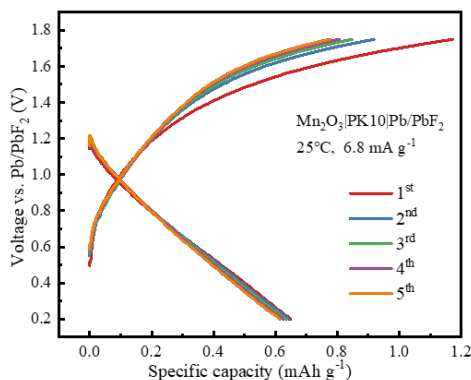


Figure 4.28: LSV curves of PK10-CNTs|PK10|Pb/PbF₂ cell at 0.1 mV/s.

4.5. Cu_2O FULL CELL TESTING AT 60 °C

(a) GCD curve of the cell C-5-2, running at room temperature for five cycles.

(b) GCD curve of the cell Fe-5-1, running at room temperature for five cycles.



(c) GCD curve of the cell Mn-5-1, running at room temperature for five cycles.

Figure 4.29: Comparison of the GCD curves of Cu_2O , FeO , Mn_2O_3 full cells running at room temperature.

Now, let's revisit the Cu_2O , FeO , and Mn_2O_3 full cells that were tested at room temperature. Upon comparing the galvanostatic charge-discharge (GCD) curves among these three full cells, it becomes evident that none of them exhibited a discharge plateau. This suggests that the potential difference of the cells exceeds the voltage limit window. Therefore, we need to either expand the voltage limit setting or adjust the potential difference to fall within the voltage-limited window. Opting for the latter solution is wiser, as the former one may potentially affect the stability of the electrolyte. From Eq. 2.11, it's evident that the potential difference is correlated with temperature. Ideally, with an increase in temperature, the potential difference should decrease. In response to the observed challenges with the metal oxide full cells at room temperature, the decision to elevate the testing temperature to 60 °C is finally made. This decision also aims to assess the impact of increased temperature on the electrochemical performance of the

metal oxide full cell. The LANHE system, coupled with the Memmwet UF30 Chamber, will facilitate these experiments on the Cu_2O full cell.

4.5.1. ELECTROCHEMICAL PERFORMANCE

Cell C-5-3 underwent galvanostatic charge and discharge measurements for 5 cycles at 60°C . In Fig. 4.31, it is observed that the charge capacity in the first cycle reaches 239.64 mAh/g, representing approximately 64.08% of the theoretical capacity of 373.97 mAh/g. This corresponds to a capacity of 0.963 mAh, which is 64.2% of the theoretical applied capacity of 1.5 mAh. However, a noticeable capacity fade occurs from the second cycle onwards, with the charged capacity decreasing to 96.23 mAh/g. The discharged specific capacity in the first cycle is measured at 109.1 mAh/g. After 2 cycles, the reaction demonstrates high reversibility. This is attributed to the initial two cycles serving as an activation process, during which certain side reactions might occur, leading to the formation of substances that enhance the electrode's conductivity. However, it's important to note that these substances are irreversible. And this is also proved by the XRD pattern.

Several additional Cu_2O full cells, including C-5-3, are tested and documented in Appendix.6.1. The average charged specific capacity for these cells in the first cycle is calculated to be 310.24 mAh/g, equivalent to 82.96% of the theoretical specific capacity of 373.97 mAh/g. The average capacity reaches 1.06 mAh, accounting for 70.67% of the theoretical applied capacity of 1.5 mAh. The average discharged specific capacity is measured at 142.1 mAh/g. The noticeable increase in capacity with the rise in running temperature indicates the positive impact of elevated temperature conditions on the capacity performance of the Cu_2O full cell. In Fig. 4.31b, it is evident that the charged plateau is around 1.7 V, starting from approximately 1.2 V, as opposed to 1.4 V observed at room temperature in cycles 2 to 5. Additionally, the discharged plateau now occurs at 0.4 V, whereas at room temperature, no plateau was observed within the range of 0.2-1.75 V. This indicates that elevating the running temperature has effectively reduced the overpotential of the cell and also increased the F^- diffusion rate.

It's evident that some irregularities have appeared in the GCD curve, and these are attributed to the voltage protection feature of the equipment. The automatic pausing of the program during voltage protection events has been occurring frequently. The primary cause of these frequent voltage protection incidents is attributed to current leakage from the oven. This phenomenon will impact our data results, leading to a lack of aesthetic appeal in the data presentation.

The presence of a convex hull at the onset of the plateau is evident, indicating the overpotential of the reaction. This is illustrated in Fig. 4.30, where the reaction must overcome a barrier to initiate. The GCD curve suggests an increasing need for a higher applied potential to initiate the discharge reaction, as observed in successive cycles where the starting voltage of the discharge plateau decreases. The growing overpotential from cycle to cycle implies a progressively challenging initiation of the reaction.

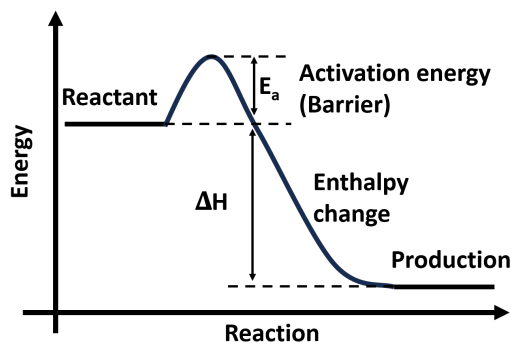
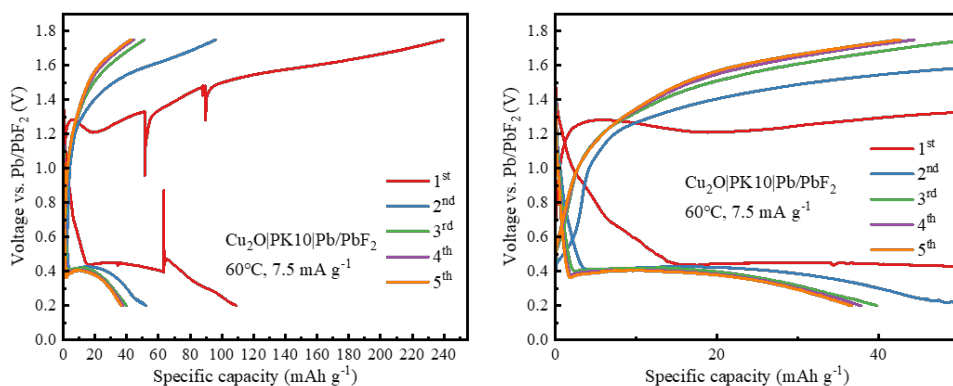


Figure 4.30: The activation energy (E_a) of a reaction represents the energy barrier that must be surpassed for the reactants to transform into products.



(a) GCD curve of the C-5-3 cell.

(b) Zoom-in area of GCD curve of the C-5-3 cell.

Figure 4.31: GCD curves of C-5-3 cell, tested at 60°C , running for five cycles.

The CV curves of the Cu_2O full cells operating at 60°C are shown in Fig. 4.32. It is evident that the reduction peaks around 0.4 V align with the discharged plateaus observed in the GCD curve. However, there are two oxidation peaks between 0.4 V and 0.8 V. Despite their prominence, no corresponding plateau is observed in the GCD curve, suggesting a discrepancy in charge behavior. Additionally, the oxidation peak observed at 1.4 V in Fig. 4.32b may be attributed to the oxidation process of the Cu_2O active material. However, it is noteworthy that this peak is absent in cell C-1-6, which underwent testing under identical conditions, indicating possible variations in cell behavior. Overall, the CV curves of the Cu_2O full cells tested at 60°C exhibit asymmetry, suggesting the presence of irreversible reactions.

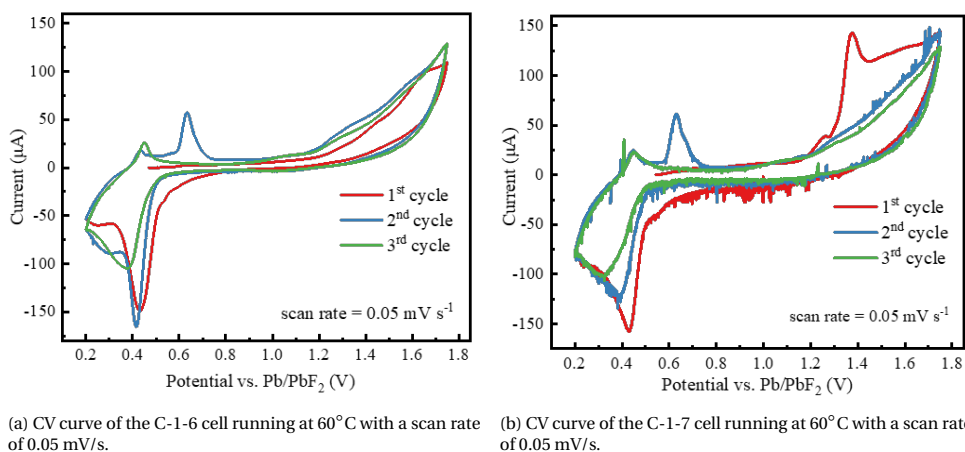
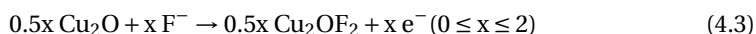


Figure 4.32: CV curves of Cu_2O full cells running at 60°C with a scan rate of 0.05 mV/s .

4.5.2. XRD CHARACTERIZATION

Ex situ XRD analysis of the A side (cathode side) is conducted, as depicted in Fig. 4.36. Firstly, let's examine the XRD pattern of the cathode after charging for the first cycle. During charging, Cu_2O should undergo oxidation while the anode should be reduced. It can be observed from the XRD pattern of the charged cathode pellet (Fig. 4.33) that the peaks corresponding to Cu_2O , located at 36.28° , 61.27° , and 73.44° , have decreased, indicating an oxidation reaction involving Cu_2O . According to Zhang et al. [19], three hypotheses exist regarding Cu_2O fluorination. The first hypothesis suggests that all remaining tetrahedral sites of the Cu_2O face-centered cubic (fcc) lattice are occupied by fluorine atoms, leading to the formation of Cu_2OF_3 . However, this material has not been reported, and its thermodynamic stability remains unknown. The second hypothesis suggests that Cu_2OF_2 is formed through the following reaction:



Here are four calculated models according to the Materials Project, as shown in Fig. 4.34. However, they are all thermodynamically unstable, and none of them has been reported in terms of synthesis and characterization. Phases P1 and $\text{I4}_1/\text{amd}$ cannot be matched to the XRD pattern of the pellet after charging, as seen in Fig. 4.35. There are no peaks for the strongest reflections of P1 and $\text{I4}_1/\text{amd}$ phases, at 17.78° and 31.71° , respectively. For phases Fddd and C2c, although there is a peak corresponding to the strongest reflection of Fddd phase and C2c phase at 18.5° , this peak also results from the reflection of PK10. Furthermore, there are no peaks for the second strongest reflection of Fddd phase located at 53.52° and C2c phase located at 53.43° . Overall, none of these four calculated phases of Cu_2OF_2 can be matched to the pellet after first charging. The third hypothesis is that the Cu_2OF_2 is unstable that it will decompose into CuO and CuF_2 . However, there are no peaks observed for the strongest reflection of CuO at 38.65° and no peaks observed for the second strongest peak of CuF_2 at 33.53° . Thus, there should be other reactions occurring instead of forming one or more of these four phases of Cu_2OF_2 or

forming CuO and CuF_2 . Also, it is unusual to find orthorhombic PbF_2 , as this material should only occur in the anode.

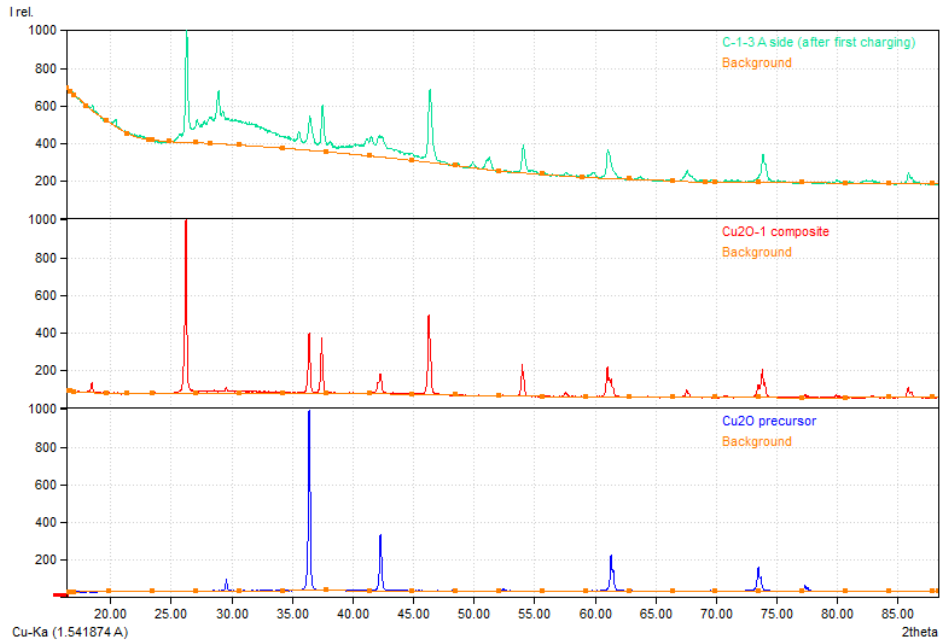


Figure 4.33: Comparison of A side (cathode side) of the cell C-1-3 among Cu_2O precursor, Cu_2O -1 composite and the pellet after charging. Cu_2O precursor is in blue, Cu_2O -1 composite is in red and the cathode pellet of cell C-1-3 after charging is in green.

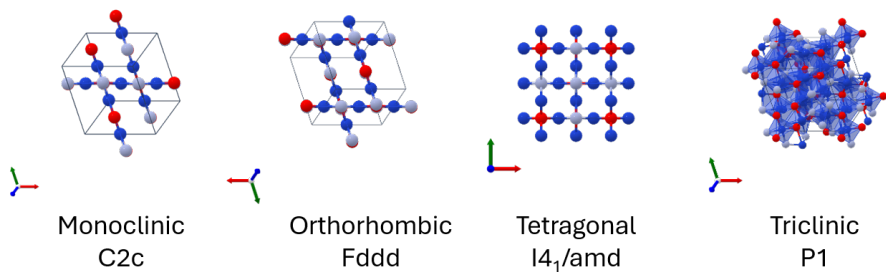
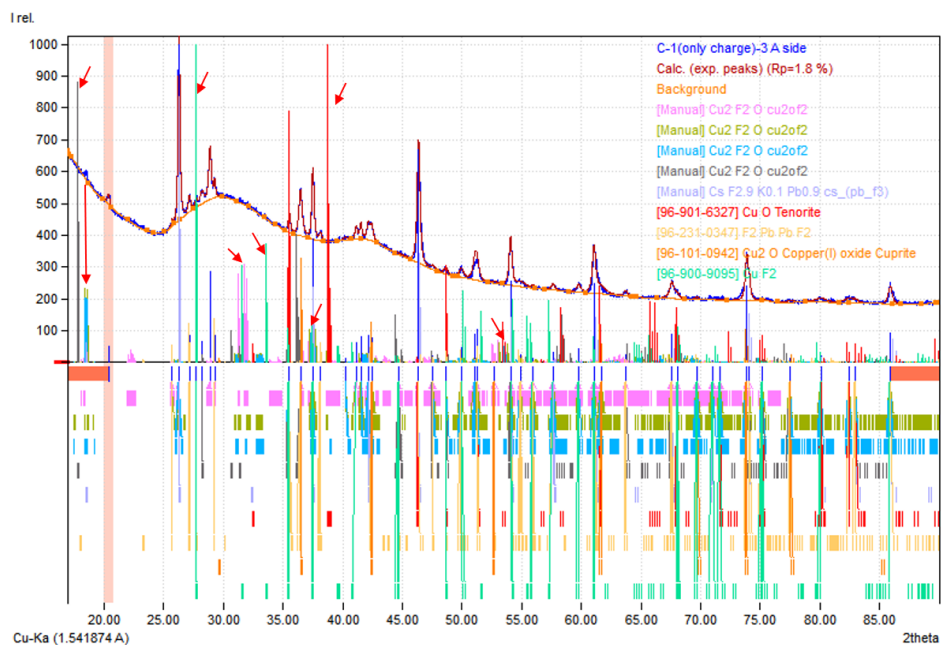


Figure 4.34: Four calculated models of Cu_2OF_2 from Materials Project.



4

Figure 4.35: Ex situ XRD patterns of the A side (cathode side) of the c-1-3 at 60°C after first charging. Cu_2OF_2 of the P1 phase is shown in pink lines, C2c phase is in army green, Fddd phase is in blue and $I4_1/amd$ phase is in grey. PK10-3 is in light purple, CuO is in red, orthorhombic PbF_2 is in light orange, Cu_2 is in orange, and CuF_2 is in blue-green.

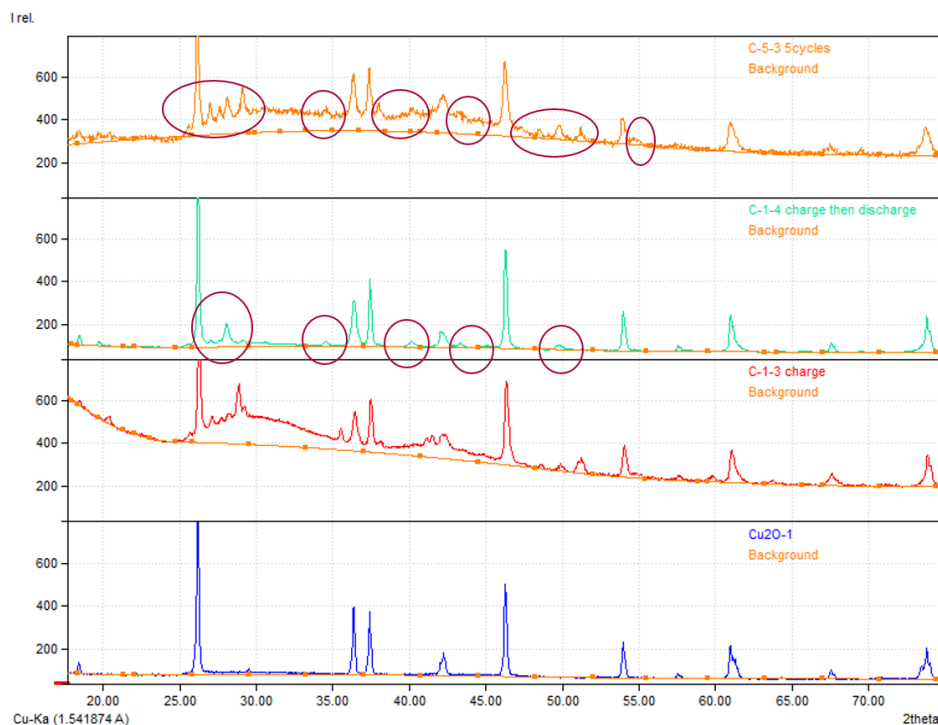


Figure 4.36: Ex situ XRD patterns of the A side (cathode side) of the Cu_2O full cell at 60°C. Cu_2O -1 cathode composite is indicated by the blue line, cathode pellet after first charging is shown in red, the cathode pellet after the first cycle is depicted in green, and cathode pellet after 5 cycles is represented in orange.

After the first cycle, the XRD patterns of the cathode differ from the original Cu_2O -1 composite, as seen in Fig. 4.36. Although peaks indicating Cu_2O are observed at 29.61°, 36.47°, 42.35°, 61.47°, 70.96°, 73.62°, etc., additional peaks are present after discharging. Peaks at 25.74°, 27.14°, 28.16°, 29.26°, 30.66°, 34.65°, 38.07°, 40.26°, 43.43°, 45.18°, 48.61°, 49.89°, 51.37°, and 65.77° indicate the presence of irreversible materials resulting from the electrochemical reactions. The PbF_2 is also matched after cycling. After five cycles of cycling, more peaks are present, and the characteristics of the XRD pattern of the charged cathode pellet combine the characteristics of the XRD pattern of the first charging and discharging pellet. This suggests the presence of more irreversible materials, which can explain the significant capacity fade between the first and third cycles.

Overall, in this section, it was found that Cu_2O full cells exhibit higher specific capacity and can achieve larger capacity at 60°C than at room temperature due to reduced overpotential and improved F^- diffusion rates. However, there was a noticeable capacity fade between the first and third cycles observed in the GCD curve, which can be attributed to irreversible reactions and materials formed during cycling, as indicated by CV curves and XRD patterns. Furthermore, the materials produced during charging could not be matched to the suggested products, which include four kinds of Cu_2OF_2 phases or its decomposed materials CuO and CuF_2 . This suggests the presence of other reactions.

5

CONCLUSIONS AND OUTLOOK

In summary, the comprehensive investigation into solid-state fluoride-ion batteries, particularly focusing on the utilization of Cu_2O , FeO , and Mn_2O_3 as cathode materials, PK10 as solid electrolyte, and Pb/PbF_2 composite as anode materials, has yielded valuable insights into the electrochemical performance and operational characteristics of metal oxide cathode-based solid-state fluoride-ion battery systems.

The successful Ag full cell test, utilizing PK10 as the solid electrolyte and Pb/PbF_2 composite as anode materials, demonstrated promising reversible capacity close to theoretical values. This achievement paves the way for further exploration of metal oxide cathode materials in solid-state fluoride-ion battery systems while employing PK10 electrolyte and Pb/PbF_2 composite anode.

At room temperature, the Cu_2O , FeO , and Mn_2O_3 full cells all exhibited negligible capacity during charge. Furthermore, no significant reduction reaction was observed during the subsequent discharge at the cathode side, as evidenced by the absence of discharged plateaus in the GCD curves. However, intriguingly, the consistent potential of the oxidation reaction was observed during the charge at the cathode across all three battery types. This suggests that the potential difference required for the fluorination reaction of the cathode exceeds the voltage limit window set for these experiments, and indicates the occurrence of another reaction common to all three distinct cell compositions. Additionally, varying degrees of electrolyte PK10 peak splitting were observed in *ex situ* diffraction data, indicating possible electrochemical activity of the electrolyte.

Investigation into the electrochemical stability window (ESW) of the electrolyte PK10 revealed a voltage range between -0.14 V to 1.92 V, with slight electrolyte instability noted at specific voltage points near 0.14 V and 1.4 V. Symmetric cell testing using Pb/PbF_2 composite electrodes confirmed the suitability of the Pb/PbF_2 composite as both counter and reference electrodes, especially at lower current and higher temperatures. This observation eliminates the anode's impact on full cell performance at room temperature.

Furthermore, Cu_2O full cells demonstrated enhanced specific capacity at elevated temperatures (60°C), achieving a specific charge capacity of 310.24 mAh/g during the first cycle. This capacity is equivalent to 82.96% of the theoretical specific capacity. The

significantly larger capacity at higher operation temperature is attributed to reduced overpotential and enhanced fluoride ions diffusion rates. Nonetheless, capacity fade between cycles indicated irreversible reactions and the formation of unidentified materials during cycling, warranting further investigation into reaction mechanisms and product identification.

At an elevated temperature of 60°C, the $\text{Cu}_2\text{O}|\text{PK10}|\text{Pb}/\text{PbF}_2$ full cell demonstrates intriguing electrochemical behavior. Understanding the specific mechanisms driving its performance is essential for optimizing its potential. This will lay the groundwork for further research on oxyfluorides as electrode materials. By exploring the electrochemical behavior of the $\text{Cu}_2\text{O}|\text{PK10}|\text{Pb}/\text{PbF}_2$ full cell at elevated temperatures, we may gain deeper insights into the role and performance characteristics of oxyfluorides in solid-state fluoride-ion batteries. Further investigation into the performance of $\text{FeO}|\text{PK10}|\text{Pb}/\text{PbF}_2$ and $\text{Mn}_2\text{O}_3|\text{PK10}|\text{Pb}/\text{PbF}_2$ full cells at higher temperatures could provide new insights into the electrochemical mechanisms of these materials, thereby helping to optimize their performance and advancing the research and application of oxyfluorides as electrode materials. Beyond the current focus on Cu_2O , FeO , and Mn_2O_3 , the exploration of other oxide materials for SSFIBs also holds great promise.

Apart from the exploration of new cathode materials, the development of novel solid electrolytes and anode materials could further expand the repertoire of materials for SSFIBs, enabling enhanced performance and broader applicability in various energy storage applications, especially when considering the application of SSFIBs at room temperature.

In conclusion, the prospects for SSFIBs are bright, with ongoing research efforts focused on understanding and optimizing the electrochemical mechanisms of existing materials and exploring new materials to unlock their full potential. These advancements could lead to the development of high-performance, cost-effective, and environmentally friendly energy storage solutions to meet the growing demands of the modern world.

6

APPENDIX

Electrolyte Name	PK10 PK10-1		PK10 PK10-3		PK10 PK10-4		PK10 PK10-2
	Jar1	Jar2	Jar1	Jar2	Jar1	Jar2	XRD characterization failed
CsF(g)	1.4437	1.4438	1.4447	1.4452	1.4449	1.446	
KF(g)	0.0542	0.0561	0.0557	0.0553	0.0555	0.056	
PbF ₂ (g)	2.0984	2.0996	2.1005	2.1005	2.0988	2.1	
Total(g)	6.69		6.73		6.1		
Pellet mass (g)	0.2		0.2006		0.1999	0.2	
R real (Ω)	312.4		200.7		192.1	46	
Pellet thickness avg. (mm)	0.5274		0.511		0.491	0.447	
Conductivity (mS/cm) at RT	0.215		0.324		0.326	1.238 at 60°C	

Table 6.1: PK10

Composite	Pb/PbF ₂ (with PK10)		
	anode-1	anode-2	anode-3
Name			
Specific capacity (mAh/g)	43.2	43.7	43.6
Pb(g)	0.5942	0.2	0.1999
PbF ₂ (g)	0.6036	0.2	0.2004
Electrolyte	PK10-1	PK10-1	PK10-1
Mass(g)	1.5055	0.5	0.5002
CNTs(g)	0.2973	0.0999	0.1002
Total(g)	2.8691	0.985	0.989
Note	ball mill (100 rpm)	hand mill	

Table 6.2: Pb/PbF₂ composite

Composite Name	PK10-CNTs PK10-CNTs	Ag cath Ag-1	Cu ₂ O cath Cu ₂ O-1	FeO cath FeO-1	Mn ₂ O ₃ cath Mn ₂ O ₃ -1
Specific Capacity (mAh/g)	-	99.2	112.2	111.8	101.6
Active material	PK10-3	Ag	Cu ₂ O	FeO	Mn ₂ O ₃
Mass (g)	0.4502	0.3998	0.1502	0.0751	0.075
Electrolyte	-	PK10-1	PK10-3	PK10-3	PK10-3
Mass (g)	-	0.4999	0.3003	0.15	0.1502
CNTs (g)	0.05	0.0995	0.05	0.0251	0.0251

Table 6.3: Composites

Cell	Pb/PbF ₂ PK10 Pb/PbF ₂					
Name	SW-50μA-1	SW-50μA-2	SW-50μA-3	SW-50μA-4	SR-50μA-1	SR-50μA-2
Theoretical Capacity (mAh)	1mAh					
Active material (g) A side	anode-1 0.0194	anode-1 0.0193	anode-1 0.0195	anode-1 0.0195	anode-1 0.0200	anode-1 0.0199
Electrolyte Mass(g)	PK10-1 0.2001	PK10-1 0.2002	PK10-1 0.2002	PK10-1 0.2001	PK10-1 0.1998	PK10-1 0.1999
Active material (g) B side	anode-1 0.0389	anode-1 0.0388	anode-1 0.0386	anode-1 0.0388	anode-1 0.0390	anode-1 0.0392
State	charge	charge	discharge	discharge	charge	charge

Cell	Pb/PbF ₂ PK10 Pb/PbF ₂					
Name	SR-50μA-3	SR-50μA-4	s-50μA-1	s-50μA-2	s-50μA-3	s-20μA-1
Theoretical Capacity (mAh)	1mAh					
Active material (g) A side	anode-1 0.0195	anode-1 0.0197	anode-2 0.0195	anode-2 0.0196	anode-2 0.0195	anode-2 0.0194
Electrolyte Mass(g)	PK10-1 0.2000	PK10-1 0.2000	PK10-1 0.2001	PK10-1 0.1998	PK10-1 0.2003	PK10-3 0.2000
Active material (g) B side	anode-1 0.0389	anode-1 0.0388	anode-2 0.0389	anode-2 0.0389	anode-2 0.0387	anode-2 0.0387
State	discharge	discharge	charge	charge	charge	charge

6

Cell	Pb/PbF ₂ PK10 Pb/PbF ₂					
Name	s-20μA-2	s-20μA-3	s-20μA-4	s-20μA-5	s-20μA-6	s-20μA-7
Theoretical Capacity (mAh)	1mAh					
Active material (g) A side	anode-2 0.0194	anode-2 0.0196	anode-2 0.0195	anode-2 0.0195	anode-3 0.0195	anode-3 0.0194
Electrolyte Mass(g)	PK10-3 0.2006	PK10-3 0.2004	PK10-3 0.2006	PK10-3 0.1999	PK10-4 0.2002	PK10-4 0.1999
Active material (g) B side	anode-2 0.0387	anode-2 0.0388	anode-2 0.0389	anode-2 0.0388	anode-3 0.0388	anode-3 0.0389
State	charge	discharge	charge	charge	charge	discharge

Table 6.4: Symmetric cells

Cu ₂ O PK10 Pb/PbF ₂						
Cell Name	C-5-1	C-35-1	C-5-2	C-5-3	C-1-1	
Theoretical Capacity (mAh)	1.5mAh					
Cu ₂ O-1 (g) (A side)	0.0134	0.0134	0.0134	0.0134	0.0134	0.0136
Electrolyte	PK10-3	PK10-3	PK10-3	PK10-3	PK10-3	PK10-4
Mass (g)	0.2004	0.2005	0.2002	0.2010	0.2005	0.2005
Active material (g) (B side)	anode-2 0.04	anode-2 0.0403	anode2+anode3 0.0402	anode 3 0.0401	anode-3 0.0399	anode-3 0.0406
State	GCD 5 cycles	GCD 35 cycles	GCD 5 cycles	GCD 5 cycles	GCD 5 cycles	only charge
Note	RT	RT	RT	60°C	60°C	60°C

Cu ₂ O PK10 Pb/PbF ₂						
Cell Name	C-1-2	C-1-3	C-1-4	C-1-5	C-1-6	C-1-7
Theoretical Capacity (mAh)	1.5mAh					
Cu ₂ O-1 (g) (A side)	0.0135	0.0136	0.0137	0.0135	0.0134	0.0134
Electrolyte	PK10-3	PK10-4	PK10-4	PK10-4	PK10-4	PK10-4
Mass (g)	0.1998	0.1994	0.1999	0.2003	0.2005	0.1999
Active material (g) (B side)	anode-3 0.04	anode-3 0.0401	anode-3 0.0405	anode-3 0.0403	anode-3 0.0404	anode-3 0.0406
State	GCD 1 cycle	only charge	GCD 1 cycle	CV	CV	CV
Note	60°C	60°C	60°C	60°C failed	60°C	60°C

Table 6.5: Cu₂O full cells

Cell	Cu ₂ O PK10 Pb/PbF ₂				
Name	C-5-3	C-1-1	C-1-2	C-1-3	C-1-4
Charged Specific Capacity (mAh/g)	239.64	333.48	302.86	306.44	368.77
Charged Capacity (mAh)	0.96	1.36	1.23	1.25	1.51
Discharged Specific capacity (mAh/g)	109.1	-	174.6	-	142.6
Charged specific capacity: 310.24 ± 42.47mAh/g					
Charged capacity: 1.26 ± 0.18 mAh					
Discharged specific capacity: 142.10 ± 26.74mAh/g					

Table 6.6: Results of GCD curves of Cu₂O full cells running at 60°

Cell	PK10-CNTS PK10 Pb/PbF ₂			
Name	L-1	L-2	L-3	L-4
PK10-CNTs composite (g) (A side)	0.01	0.01	0.01	0.0102
Electrolyte Mass (g)	PK10-1 0.1997	PK10-3 0.2	PK10-3 0.2003	PK10-3 0.2004
anode-2 (g) (B side)	0.0459	0.046	0.046	0.0451
Note	positive side	Failed	Failed	negative side

Table 6.7: PK10-CNTS|PK10|Pb/PbF₂ full cells for LSV measurement

Cell	FeO PK10 – 3 Pb/PbF ₂	Mn ₂ O ₃ PK10 Pb/PbF ₂
Name	Fe – 5 – 1	Mn – 5 – 1
Theoretical Capacity (mAh)	1mAh	1mAh
Active material	FeO – 1	Mn ₂ O ₃ – 1
Mass (g) (A side)	0.0093	0.0098
Electrolyte	PK10-3	PK10-3
Mass (g)	0.1997	0.2003
Active material	anode-3	anode-3
Mass (g) (B side)	0.0298	0.0301

Table 6.8: FeO and Mn₂O₃ full cells

Cell	Ag PK10 Pb/PbF ₂		
Name	Ag-5-1	Ag-5-2	Ag-5-3
Theoretical Capacity (mAh)	1mAh		
Ag-1 (g) (A side)	0.0101	0.01	0.0101
Electrolyte	PK10-1	PK10-1	PK10-3
Mass (g)	0.2499	0.2495	0.2493
anode-2 (g) (B side)	0.0454	0.0452	0.0449
Note	for GCD	for GCD	for CV

Table 6.9: Ag full cells

	(110) 2 θ (degree)	(200) 2 θ (degree)	(211) 2 θ (degree)
PK10-1	26.398	37.659	46.557
PK10-3	26.351	37.591	46.471
PK10-4	26.374	37.624	46.512

Table 6.10: Position of main peaks in PK10-1, PK10-3, and PK10-4.

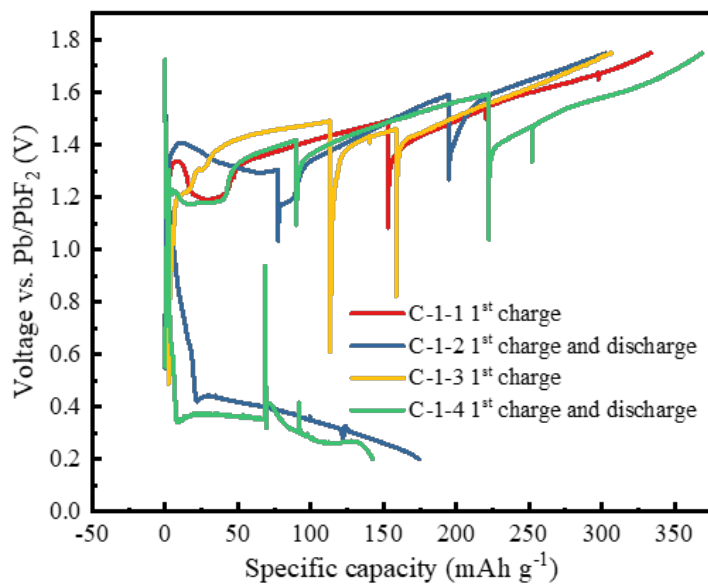


Figure 6.1: GCD curves of cell C-1-1, C-1-2, C-1-3, C-1-4. Note: The unstable data is attributed to the presence of voltage protection, as depicted in section 4.5.

ACKNOWLEDGEMENTS

As my time at Tud pursuing my master's degree comes to an end, I must first express my deepest gratitude to my mother. It is her unwavering support that has afforded me the opportunity to embark on this journey. Throughout, she has shown immense care for both my life and studies. I am also thankful to my grandparents; they hope that I can take care of myself in this distant and beautiful country. Though my family may not fully grasp the intricacies of my graduation project, their willingness to listen to the challenges and triumphs I encountered along the way has been a source of great comfort.

I really want to extend special thanks to my daily supervisor, Pedro. He always tries his best to help me promptly and sincerely. When my experiments are not going well, he consistently offers encouragement, praise and valuable advice. The positive feedback has made me not want to disappoint him. Pedro is a meticulous, organized, and conscientious person. Along the way, he has guided me, and I have learned many excellent qualities from him. I am also indebted to Shoshan for her invaluable assistance in navigating the complexities of graduation formalities and for generously offering her time for discussions. Gratitude is also extended to Amantante, who, amidst a busy schedule, took the time to review my thesis and serve on my defense committee.

I am also grateful to Biffo from the laboratory research group for his patience in teaching me GSAS. Additionally, I want to extend my gratitude to Wang Hao, Chen Chaofan, Zhang Shengnan, and Cheng Zhu for their support during the experiments. Furthermore, I appreciate Lex for our harmonious coordination in utilizing the high-temperature oven, despite its limited channels.

I am grateful to the friends I met in the Netherlands; their presence transformed dreary, rainy, and windy days into moments of warmth and joy. I am especially thankful to my dear Qin Xusen; he helped me through difficult times and provided me with tremendous support both in life and spirit. When obstacles arose in my project, he provided me with solace and encouragement. Encountering him has been a stroke of luck, enriching my life in countless ways.

BIBLIOGRAPHY

- [1] Judao Technology. *The "Past and Present" of Batteries*. https://www.judaoedu.com/news_show.aspx?id=13058. Accessed: February 17, 2024. Judao Chemistry, 2022.
- [2] Antonin Grenier. "Development of solid-state Fluoride-ion Batteries: cell design, electrolyte characterization and electrochemical mechanisms". PhD thesis. Université Pierre et Marie Curie-Paris VI, 2016.
- [3] Albert W Xiao, Giulia Galatolo, and Mauro Pasta. "The case for fluoride-ion batteries". In: *Joule* 5.11 (2021), pp. 2823–2844.
- [4] Yuqing Chen et al. "A review of lithium-ion battery safety concerns: The issues, strategies, and testing standards". In: *Journal of Energy Chemistry* 59 (2021), pp. 83–99.
- [5] Jiali Liu et al. "Constructing a BiF₃/Bi₇F₁₁O₅ multiple-phase composite as advanced cathode for room-temperature all-solid-state fluoride-ion batteries". In: *Journal of Electroanalytical Chemistry* 928 (2023), p. 117073.
- [6] Sumol V Gopinadh et al. "Fluoride-ion batteries: State-of-the-art and future perspectives". In: *Sustainable Materials and Technologies* (2022), e00436.
- [7] Lei Liu et al. "Nd³⁺ doped BaSnF₄ solid electrolyte for advanced room-temperature solid-state fluoride ion batteries". In: *Ceramics International* 46.12 (2020), pp. 20521–20528.
- [8] Mohammad Ali Nowroozi et al. "Fluoride ion batteries—past, present, and future". In: *Journal of Materials Chemistry A* 9.10 (2021), pp. 5980–6012.
- [9] W Baukal. "Über reaktionsmöglichkeiten in elektroden von festkörperbatterien". In: *Electrochimica Acta* 19.11 (1974), pp. 687–694.
- [10] John H Kennedy and Ronald C Miles. "Ionic Conductivity of Doped Beta-Lead Fluoride". In: *Journal of The Electrochemical Society* 123.1 (1976), p. 47.
- [11] John H Kennedy and James C Hunter. "Thin-film galvanic cell Pb/PbF₂/PbF₂, CuF₂/Cu". In: *Journal of The Electrochemical Society* 123.1 (1976), p. 10.
- [12] J Schoonman. "A solid-state galvanic cell with fluoride-conducting electrolytes". In: *Journal of The Electrochemical Society* 123.12 (1976), p. 1772.
- [13] Waldemar Borger, Udo Hullmeine, and Ernst Voss. *Galvanic cell with solid fluoride ion-conductive electrolyte*. US Patent 3,973,990. 1976.
- [14] Y Danto et al. "A Pb|PbF₂|BiF₃|Bi thin solid film reversible galvanic cell". In: *Thin Solid Films* 55.3 (1978), pp. 347–354.
- [15] J Schoonman et al. "Fluoride-Conducting Solid Electrolytes in Galvanic Cells". In: *Journal of The Electrochemical Society* 126.5 (1979), p. 709.

- [16] J Schoonman and A Wolfert. “Alloy-anodes in fluoride solid-state batteries”. In: *J. Electrochem. Soc* 128.7 (1981), pp. 1522–1523.
- [17] J Schoonman and A Wolfert. “Solid-state galvanic cells with fast fluoride conducting electrolytes”. In: *Solid State Ionics* 3 (1981), pp. 373–379.
- [18] M Anji Reddy and Max Fichtner. “Batteries based on fluoride shuttle”. In: *Journal of Materials Chemistry* 21.43 (2011), pp. 17059–17062.
- [19] Datong Zhang et al. “Reversible and Fast (De) fluorination of High-Capacity Cu_2O Cathode: One Step Toward Practically Applicable All-Solid-State Fluoride-Ion Battery”. In: *Advanced Energy Materials* 11.45 (2021), p. 2102285.
- [20] Duc Tho Thieu et al. “ CuF_2 as reversible cathode for fluoride ion batteries”. In: *Advanced Functional Materials* 27.31 (2017), p. 1701051.
- [21] Hiroyuki Nakano et al. “Fluoride-ion shuttle battery with high volumetric energy density”. In: *Chemistry of Materials* 33.1 (2020), pp. 459–466.
- [22] Takahiro Yoshinari et al. “Kinetic analysis and alloy designs for metal/metal fluorides toward high rate capability for all-solid-state fluoride-ion batteries”. In: *Journal of Materials Chemistry A* 9.11 (2021), pp. 7018–7024.
- [23] Datong Zhang et al. “Cu–Pb nanocomposite cathode material toward room-temperature cycling for all-solid-state fluoride-ion batteries”. In: *ACS Applied Energy Materials* 4.4 (2021), pp. 3352–3357.
- [24] Takeshi Tojigamori et al. “Reversible Charge/Discharge Reaction of a Ternary Metal Fluoride, Pb_2CuF_6 : A Highly Conductive Cathode Material for Fluoride-Ion Batteries”. In: *ACS Applied Energy Materials* 5.1 (2022), pp. 1002–1009.
- [25] Antonin Grenier et al. “Electrochemical reactions in fluoride-ion batteries: mechanistic insights from pair distribution function analysis”. In: *Journal of Materials Chemistry A* 5.30 (2017), pp. 15700–15705.
- [26] Toshiro Yamanaka et al. “Reactivity and mechanisms in fluoride shuttle battery reactions: difference between orthorhombic and cubic BiF_3 single microparticles”. In: *ACS Applied Energy Materials* 2.12 (2019), pp. 8801–8808.
- [27] Hiroaki Konishi et al. “Improved electrochemical performances in a bismuth fluoride electrode prepared using a high energy ball mill with carbon for fluoride shuttle batteries”. In: *Journal of Electroanalytical Chemistry* 839 (2019), pp. 173–176.
- [28] Hiroaki Konishi et al. “Electrochemical Performance of BiF_3 - BaF_2 Solid Solution with Three Different Phases on a Fluoride Shuttle Battery System”. In: *Chemistry-Select* 5.16 (2020), pp. 4943–4946.
- [29] Atsushi Inoishi et al. “ FeF_3 as Reversible Cathode for All-Solid-State Fluoride Batteries”. In: *Advanced Energy and Sustainability Research* (2022), p. 2200131.
- [30] Datong Zhang et al. “Understanding the reaction mechanism and performances of 3d transition metal cathodes for all-solid-state fluoride ion batteries”. In: *Journal of Materials Chemistry A* 9.1 (2021), pp. 406–412.

- [31] Mohammad Ali Nowroozi et al. “LaSrMnO₄: reversible electrochemical intercalation of fluoride ions in the context of fluoride ion batteries”. In: *Chemistry of Materials* 29.8 (2017), pp. 3441–3453.
- [32] Mohammad Ali Nowroozi and Oliver Clemens. “Insights on the behavior of conversion-based anode materials for fluoride ion batteries by testing against an intercalation-based reference cathode”. In: *ACS Applied Energy Materials* 1.11 (2018), pp. 6626–6637.
- [33] Le Zhang, Munnangi Anji Reddy, and Maximilian Fichtner. “Electrochemical performance of all solid-state fluoride-ion batteries based on thin-film electrolyte using alternative conductive additives and anodes”. In: *Journal of Solid State Electrochemistry* 22 (2018), pp. 997–1006.
- [34] Victoria K Davis et al. “Room-temperature cycling of metal fluoride electrodes: Liquid electrolytes for high-energy fluoride ion cells”. In: *Science* 362.6419 (2018), pp. 1144–1148.
- [35] Mohammad Ali Nowroozi, Benjamin de Laune, and Oliver Clemens. “Reversible electrochemical intercalation and deintercalation of fluoride ions into host lattices with Schafarzikite-type structure”. In: *ChemistryOpen* 7.8 (2018), pp. 617–623.
- [36] Wasif Zaheer et al. “Reversible room-temperature fluoride-ion insertion in a tunnel-structured transition metal oxide host”. In: *ACS Energy Letters* 5.8 (2020), pp. 2520–2526.
- [37] Oliver Clemens et al. “Electrochemical fluorination of perovskite type BaFeO_{2.5}”. In: *Dalton Transactions* 43.42 (2014), pp. 15771–15778.
- [38] Mohammad Ali Nowroozi. “On the Development of Intercalation-Based Cathode Materials for All-Solid-State Fluoride Ion Batteries”. In: (2020).
- [39] Xiao-Yong Yang, Wei Luo, and Rajeev Ahuja. “Fluoride ion batteries: Designing flexible M₂CH₂ (M= Ti or V) MXenes as high-capacity cathode materials”. In: *Nano Energy* 74 (2020), p. 104911.
- [40] Kerstin Wissel et al. “Developing intercalation based anode materials for fluoride-ion batteries: topochemical reduction of Sr₂TiO₃F₂ via a hydride based defluorination process”. In: *Journal of Materials Chemistry A* 6.44 (2018), pp. 22013–22026.
- [41] Chang Liu et al. “Electrides: a review”. In: *Journal of Materials Chemistry C* 8.31 (2020), pp. 10551–10567.
- [42] Daniel L Druffel et al. “Synthesis and electronic structure of a 3D crystalline stack of MXene-like sheets”. In: *Chemistry of Materials* 31.23 (2019), pp. 9788–9796.
- [43] Da Deng. “Transition Metal Oxyfluorides for Next-Generation Rechargeable Batteries”. In: *ChemNanoMat* 3.3 (2017), pp. 146–159.
- [44] Jordi Cabana et al. “Beyond intercalation-based Li-ion batteries: the state of the art and challenges of electrode materials reacting through conversion reactions”. In: *Advanced materials* 22.35 (2010), E170–E192.
- [45] Tsuyoshi Takami et al. “A new Bi_{0.7}Fe_{1.3}O_{1.5}F_{1.7} phase: Crystal structure, magnetic properties, and cathode performance in fluoride-ion batteries”. In: *APL Materials* 8.5 (2020), p. 051103.

- [46] Jiali Liu et al. “Constructing a $\text{BiF}_3/\text{Bi}_7\text{F}_{11}\text{O}_5$ multiple-phase composite as advanced cathode for room-temperature all-solid-state fluoride-ion batteries”. In: *Journal of Electroanalytical Chemistry* 928 (2023), p. 117073.
- [47] Yanchang Wang et al. “Oxyfluoride Cathode for All-Solid-State Fluoride-Ion Batteries with Small Volume Change Using Three-Dimensional Diffusion Paths”. In: *Chemistry of Materials* 34.23 (2022), pp. 10631–10638.
- [48] Kota Motohashi et al. “Revealing Impacts of Anion Defect Species on Fluoride-Ion Conduction of Ruddlesden-Popper Oxyfluoride $\text{Ba}_2\text{ScO}_3\text{F}$ ”. In: *Electrochemistry* 90.12 (2022), pp. 127005–127005.
- [49] Keisuke Hibino et al. “Experimental Visualization of the Interstitialcy Diffusion of Anions in the LaOF-Based Oxyfluoride $\text{La}_{0.9}\text{Sr}_{0.1}\text{O}_{0.45}\text{F}_2$ ”. In: *ACS Applied Energy Materials* 4.9 (2021), pp. 8891–8900.
- [50] Kerstin Wissel et al. “Electrochemical reduction and oxidation of Ruddlesden-Popper-type $\text{La}_2\text{NiO}_3\text{F}_2$ within fluoride-ion batteries”. In: *Chemistry of Materials* 33.2 (2021), pp. 499–512.
- [51] Nicholas H Bashian et al. “Electrochemical oxidative fluorination of an oxide perovskite”. In: *Chemistry of Materials* 33.14 (2021), pp. 5757–5768.
- [52] Jinzhu Wang et al. “A Fluoride-ion-conducting solid electrolyte with both high conductivity and excellent electrochemical stability”. In: *Small* 18.5 (2022), p. 2104508.
- [53] M Anji Reddy and Max Fichtner. “Batteries based on fluoride shuttle”. In: *Journal of Materials Chemistry* 21.43 (2011), pp. 17059–17062.
- [54] Harshita Bhatia et al. “Conductivity Optimization of Tysonite-type $\text{La}_{1-x}\text{Ba}_x\text{F}_{3-x}$ Solid Electrolytes for Advanced Fluoride Ion Battery”. In: *ACS applied materials & interfaces* 9.28 (2017), pp. 23707–23715.
- [55] Irshad Mohammad et al. “Synthesis of Fast Fluoride-Ion-Conductive Fluorite-Type $\text{Ba}_{1-x}\text{Sb}_x\text{F}_{2+x}$ ($0.1 \leq x \leq 0.4$): A Potential Solid Electrolyte for Fluoride-Ion Batteries”. In: *ACS applied materials & interfaces* 10.20 (2018), pp. 17249–17256.
- [56] Kazuhiro Mori et al. “Experimental visualization of interstitialcy diffusion pathways in fast-fluoride-ion-conducting solid electrolyte $\text{Ba}_{0.6}\text{La}_{0.4}\text{F}_{2.4}$ ”. In: *ACS Applied Energy Materials* 3.3 (2020), pp. 2873–2880.
- [57] Belto Dieudonné et al. “The key role of the composition and structural features in fluoride ion conductivity in tysonite $\text{Ce}_{1-x}\text{Sr}_x\text{F}_{3-x}$ solid solutions”. In: *Dalton Transactions* 46.11 (2017), pp. 3761–3769.
- [58] Belto Dieudonné et al. “Exploring the $\text{Sm}_{1-x}\text{Ca}_x\text{F}_{3-x}$ Tysonite Solid Solution as a Solid-State Electrolyte: Relationships between Structural Features and F-Ionic Conductivity”. In: *The Journal of Physical Chemistry C* 119.45 (2015), pp. 25170–25179.
- [59] Irshad Mohammad et al. “Room-temperature, rechargeable solid-state fluoride-ion batteries”. In: *ACS Applied Energy Materials* 1.9 (2018), pp. 4766–4775.
- [60] Fumika Fujisaki et al. “Mechanical synthesis and structural properties of the fast fluoride-ion conductor PbSnF_4 ”. In: *Journal of Solid State Chemistry* 253 (2017), pp. 287–293.

- [61] Florian Preishuber-Pflügl et al. “Defect-enhanced F⁻ ion conductivity in layer-structured nanocrystalline BaSnF₄ prepared by high-energy ball milling combined with soft annealing”. In: *physica status solidi (c)* 12.1-2 (2015), pp. 10–14.
- [62] Lei Liu et al. “SnF₂-based fluoride ion electrolytes MSnF₄ (M= Ba, Pb) for the application of room-temperature solid-state fluoride ion batteries”. In: *Journal of Alloys and Compounds* 819 (2020), p. 152983.
- [63] Lei Liu et al. “Nd³⁺ doped BaSnF₄ solid electrolyte for advanced room-temperature solid-state fluoride ion batteries”. In: *Ceramics International* 46.12 (2020), pp. 20521–20528.
- [64] Darren HS Tan et al. “From nanoscale interface characterization to sustainable energy storage using all-solid-state batteries”. In: *Nature nanotechnology* 15.3 (2020), pp. 170–180.
- [65] Shuaifeng Lou et al. “Interface issues and challenges in all-solid-state batteries: lithium, sodium, and beyond”. In: *Advanced Materials* 33.6 (2021), p. 2000721.
- [66] LN Patro. “Role of mechanical milling on the synthesis and ionic transport properties of fast fluoride ion conducting materials”. In: *Journal of Solid State Electrochemistry* 24 (2020), pp. 2219–2232.
- [67] Christine Friederike Burmeister and Arno Kwade. “Process engineering with planetary ball mills”. In: *Chemical Society Reviews* 42.18 (2013), pp. 7660–7667.
- [68] V Baheti, R Abbasi, and J Militky. “Ball milling of jute fibre wastes to prepare nanocellulose”. In: *World Journal of Engineering* 9.1 (2012), pp. 45–50.
- [69] Masatoshi Uno et al. “Synthesis and evaluation of Pb_{1-x}Sn_xF₂ by mechanical milling”. In: *Solid State Ionics* 176.31-34 (2005), pp. 2493–2498.
- [70] Mohammad Ali Nowroozi et al. “Fluoride ion batteries—past, present, and future”. In: *Journal of Materials Chemistry A* 9.10 (2021), pp. 5980–6012.
- [71] J Epp. “X-ray diffraction (XRD) techniques for materials characterization”. In: *Materials characterization using nondestructive evaluation (NDE) methods*. Elsevier, 2016, pp. 81–124.
- [72] David Lorca Galindo et al. “Characterisation of NEXT-DEMO using xenon K-alpha X-rays”. In: *Journal Of Instrumentation*, 2014, vol. 9, p. P10007-1-P10007-20 (2014).
- [73] Editors of Encyclopaedia Britannica. *Bragg law*. Encyclopedia Britannica. Sept. 2023. URL: <https://www.britannica.com/science/Bragg-law>.
- [74] Fortunato Migliardini and Pasquale Corbo. “Optimization of fuel cell performance in vehicles by electrochemical impedance spectroscopy”. In: *2012 Electrical Systems for Aircraft, Railway and Ship Propulsion*. IEEE, 2012, pp. 1–6.
- [75] C Hu and Y Hua. “Principles of linear sweep voltammetry and interpretations of voltammograms”. In: *Univ Chem* 36 (2021), pp. 4–7.
- [76] Denis Andrienko. “Cyclic voltammetry”. In: *John Wiley & Sons publication, New York* (2008), pp. 3–12.

-
- [77] Inga Beyers, Astrid Bensmann, and Richard Hanke-Rauschenbach. “Ragone plots revisited: A review of methodology and application across energy storage technologies”. In: *Journal of Energy Storage* 73 (2023), p. 109097.
- [78] Jinzhu Wang and Cheng Ma. “Superior room-temperature cycling stability of fluoride-ion batteries enabled by solid electrolytes synthesized by the solid-state reaction”. In: *Science China Materials* 65.11 (2022), pp. 3025–3032.